

# Templated Epitaxial Growth and Doping of Organic Thin Films

Dissertation

zur Erlangung des akademischen Grades  
doctor rerum naturalium (Dr. rer. nat.)

vorgelegt dem Rat der Physikalisch-Astronomischen Fakultät  
der Friedrich-Schiller-Universität Jena



von Dipl.-Phys. Marco Grünewald

geboren am 16.04.1987 in Jena

## **Gutachter**

1. Prof. Dr. Torsten Fritz (Friedrich-Schiller-Universität Jena)
2. Prof. Dr. Moritz Sokolowski (Universität Bonn)
3. o.Univ.-Prof. Dr. Peter Zeppenfeld (Johannes Kepler Universität Linz)

Tag der Disputation: 17.03.2017

## Abstract

This study focuses on the determination of the structure-property relations of epitaxially grown organic thin films. In the first part, the impact of an ultrathin 3,4,9,10-perylene-tetracarboxylic-dianhydride (PTCDA) interlayer on the structural and optical properties of tin(II)-phthalocyanine (SnPc) films on Ag(111) is investigated. It is shown that the PTCDA layer serves as a template enabling for the highly ordered growth of SnPc up to the multilayer regime. The function of the PTCDA layer in this context is revealed by means of a comprehensive characterization of the SnPc structures formed, which are related to the respective film-thickness-dependent features in the optical absorption. In the second part of this study, potassium-doped monolayer domains on Ag(111) are structurally, electronically, and optically characterized. It is revealed that potassium strongly interacts with PTCDA resulting in a reordering of the commensurate PTCDA herringbone structure into other highly ordered phases comprising  $K_2$ PTCDA and  $K_4$ PTCDA charge transfer complexes. The drastic changes in the structures are accompanied by new features in the electronic and optical spectra indicating that PTCDA is doubly negatively charged in both complex geometries and the metal-organic hybridization becomes weaker with increasing potassium concentration.

## Kurzfassung

Diese Arbeit beschäftigt sich mit der Bestimmung von Struktur-Eigenschafts-Beziehungen von epitaktisch gewachsenen organischen Dünnschichten. Im ersten Teil der Arbeit wird der Einfluss einer ultradünnen 3,4,9,10-Perylentetracarbonsäuredianhydrid (PTCDA) Zwischenschicht auf die strukturellen und optischen Eigenschaften von Zinn(II)-Phthalocyanin (SnPc) Schichten auf Ag(111) untersucht. Es wird gezeigt, dass die PTCDA Schicht als Template dient und so das hochgeordnete Wachstum von SnPc bis in den Multilagenbereich ermöglicht. Die Funktion der PTCDA Lage in diesem Zusammenhang wird mit Hilfe einer umfassenden Analyse der gebildeten SnPc Strukturen geklärt, welche in Beziehung zu den schichtdickenabhängigen Features in der jeweiligen optischen Absorption gebracht werden. Im zweiten Teil dieser Arbeit werden kaliumdotierte Monolagendomanänen von PTCDA auf Ag(111) strukturell, elektronisch und optisch charakterisiert. Es zeigt sich, dass Kalium stark mit PTCDA wechselwirkt, da eine Umordnung der kommensurablen PTCDA Fischgrätenstruktur in andere hochgeordnete Phasen erfolgt, welche  $K_2$ PTCDA und  $K_4$ PTCDA Ladungstransfer-Komplexe beinhalten. Die drastischen Änderungen der Strukturen gehen mit einer Änderung der elektronischen und optischen Spektren einher, welche darauf hindeuten, dass PTCDA in beiden Komplexgeometrien doppelt negativ geladen vorliegt und die metallorganische Hybridisierung mit steigender Kaliumkonzentration schwächer wird.

# Contents

<b>Contents</b>	<b>1</b>
<b>1 Motivation</b>	<b>3</b>
<b>2 Organic Molecules</b>	<b>7</b>
2.1 Orbitals and Bonds . . . . .	7
2.2 Used Molecular Substances . . . . .	8
<b>3 Methods and Devices</b>	<b>11</b>
3.1 Organic Molecular Beam Epitaxy . . . . .	11
3.2 Optical and Electronic Characterization . . . . .	12
3.2.1 Differential Reflectance Spectroscopy (DRS) . . . . .	12
3.2.2 UV-Vis Absorption Spectroscopy . . . . .	19
3.2.3 Photoelectron Spectroscopy (PES) . . . . .	20
3.3 Structural Characterization . . . . .	23
3.3.1 Low-Energy Electron Diffraction (LEED) . . . . .	23
3.3.2 Scanning Tunneling [Hydrogen] Microscopy (ST[H]M) . . . . .	24
3.3.3 Normal Incidence X-Ray Standing Wave (NIXSW) . . . . .	26
<b>4 SnPc Films on a PTCDA Monolayer Template</b>	<b>29</b>
4.1 Introduction . . . . .	29
4.2 Structural Characterization . . . . .	30
4.2.1 SnPc Submonolayers and Monolayers . . . . .	30
4.2.2 SnPc Bilayers and Multilayers . . . . .	40
4.3 Optical Properties . . . . .	46
4.3.1 SnPc Monolayer . . . . .	47
4.3.2 SnPc Bilayer . . . . .	49

4.3.3	Stacked Bilayers . . . . .	50
4.4	Summary and Conclusion . . . . .	52
<b>5</b>	<b>Potassium Doping of PTCDA Monolayer Domains on Ag(111)</b>	<b>55</b>
5.1	Introduction . . . . .	56
5.2	Optical Properties . . . . .	57
5.3	Electronic Properties . . . . .	61
5.3.1	Valence Band Spectra and Work Functions . . . . .	61
5.3.2	Core Level Spectra . . . . .	63
5.4	Structural Characterization . . . . .	69
5.4.1	Lateral Structures . . . . .	69
5.4.2	Adsorption Heights . . . . .	74
5.5	Summary and Conclusion . . . . .	82
<b>6</b>	<b>General Conclusions and Future Perspectives</b>	<b>85</b>
	<b>Appendix</b>	<b>89</b>
	<b>References</b>	<b>97</b>
	<b>List of Figures</b>	<b>118</b>
	<b>List of Tables</b>	<b>120</b>
	<b>Publications</b>	<b>123</b>
	<b>Danksagung</b>	<b>129</b>
	<b>Erklärung</b>	<b>131</b>

# 1 Motivation

Organic thin films have attracted particular interest in recent years owing to their beneficial electronic and optical properties which are partially complementary to silicon-based electronics. This technology takes advantage of the great flexibility and manifold of organic molecules provided by the chemical toolbox for synthesis. [1] In order to access a broad understanding of these new capabilities, systematical studies are indispensable. The main focus in common research lies on one of the most promising classes of molecules for application-relevant films, namely those featuring extended  $\pi$ -conjugated electron systems. [2] Thin films consisting of these molecules have been intensively studied and even first applications like field effect transistors (OFET), light-emitting diodes (OLED), and photovoltaic devices (OPVD) benefit from this technology. [3–5]

Organic components in devices often consist of several stacked thin layers (i.e., planar heterojunctions) each providing a specific functionality (e.g., exciton generation, charge carrier injection, transport, or blocking). [4, 6] Different requirements for functional operation, which even might compete with each other, need to be considered. [2] For example, in a photovoltaic device, on the one hand, more light is absorbed and thus more excitons are created the thicker the respective films are, on the other hand, exciton diffusion lengths are small and hence exciton separation is rather inefficient, while often also charge carrier conductivities are limited, making thinner films desirable. [7]

One of the most important parameters describing the electronic properties of films is the charge carrier conductivity  $\sigma = |q|n\mu$ , where  $q$  is the charge,  $n$  is the density, and  $\mu$  is the mobility of the charge carriers (electrons or holes). The issue of the small charge carrier conductivity can be tackled by optimizing the two parameters  $n$  and  $\mu$ , which can be indeed tuned to a large extent. For instance, it is known that the mobility  $\mu$  can be increased by orders of magnitude by minimizing traps and/or defects. [8, 9] Designing the respective layers as highly ordered films thus significantly

enhances charge carrier mobilities in organic layers. Such films are expected to play an important role in future applications like organic lasers and logical devices. [10, 11] However, challenging preparation conditions still hamper a broad application of such films so far. The charge carrier density  $n$  can be adjusted by controlling the energy level alignment, e.g., by doping. [12–15] Doping means the controlled incorporation of electron acceptors or donors which can be either molecular or atomic species. The doping ratio in organic films is typically in the order of approx.  $10^{-3}$  to one and thus fundamentally different from the inorganic counterpart where extremely low dopant concentrations are applied. [13] Thus, doping of organic material can have a strong influence on the structures formed. Consequently, the charge carrier density and mobility cannot be optimized independently, sometimes they even counteract each other. Understanding and controlling molecular rearrangement effects in organic films upon doping is thus indispensable for improvements of such layers.

Of special interest for the design of organic electronic devices are interfaces, naturally occurring when a layer is contacted or several layers are stacked. This applies to metal-organic but also to organic-organic interfaces. Interfaces can be responsible for effects not expected from the intrinsic properties of the layers, e.g., due to charge transfers across the interfaces, dipole formation, molecular exchange, and so forth. [16] The region where interface effects occur, often extends by a few monolayers only. It is thus crucial to design this region, even on the molecular scale, in order to meet the requirements for functional interaction of all layers within a device. A profound understanding of the physics behind interface formation is thus highly motivated. Devices are, however, usually far too complex for such investigations. Any kind of structural imperfections will immediately obscure the interface effects of interest. It is therefore necessary to study model systems with well-defined interfaces and layers consisting of pure constituents. Such model systems can be fabricated by organic molecular beam epitaxy (OMBE). [17–26]

This thesis aims to provide insight into the physics of interface formation by means of model systems. The used molecular substances are briefly introduced in Chp. 2. Basic information about the employed methods and experimental setups are given in Chp. 3. In Chp. 4, particular attention is paid on the formation of an organic-organic heterointerface and the influence this can have on the structures formed in the top layer. It is demonstrated that such an interface can be used for achieving highly ordered growth of organic material up to multilayers. In Chp. 5,



the interface between a metal and a potassium-doped organic film is investigated. It will be shown that depending on the doping ratio, different charge-transfer complex geometries are formed. The electronic interplay between molecules, dopants, and the metal surface shall be of particular interest. Finally, general conclusions drawn from the results in this work and an outlook are given in Chp. 6.



# 2 Organic Molecules

## 2.1 Orbitals and Bonds

Organic molecules are chemical compounds of carbon ( ${}_6C$ , electron configuration  $[He] 2s^2 2p^2$ ) often containing hydrogen, halogens, oxygen, nitrogen and also metal atoms. The variety of possible compounds is due to the distinct tendency of carbon to form hybrid orbitals. Such orbitals can be energetically favored upon bond formation, e.g., if two  $2p$  orbitals hybridize with one  $2s$  orbital, three energetically degenerate  $2sp_2$  orbitals are formed and one  $p_z$  orbital remains. When two or more of such  $2sp_2$  orbitals overlap, directed bonds ( $\sigma$ ) are created, and the corresponding states energetically split in bonding ( $\sigma$ ) and anti-bonding ( $\sigma^*$ ) states. The remaining  $p_z$  orbitals form delocalized bonds ( $\pi$ ), whose states again split in bonding ( $\pi$ ) and anti-bonding ( $\pi^*$ ) states (cf. Fig. 2.1). In the molecular ground state, the orbitals are successively filled (occupied) with electrons (at maximum two electrons with opposite spin in each orbital) beginning at the energetically lowest lying orbital according to *Hund's* rules. The energetic separation between the highest occupied

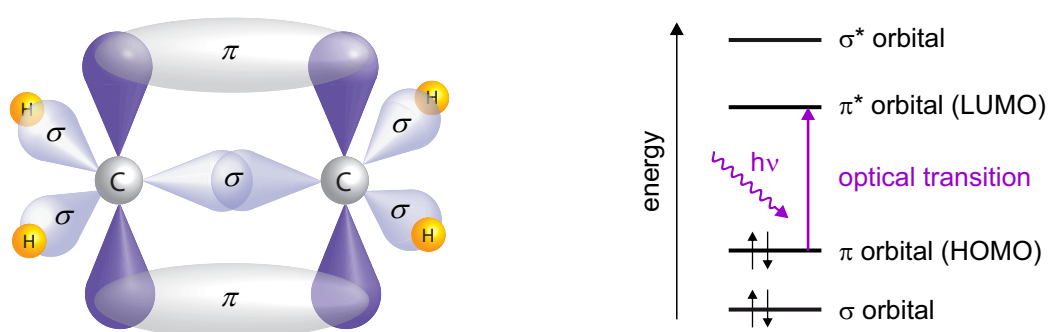


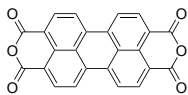
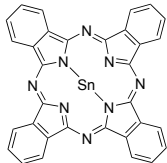
**Figure 2.1:** (a) Scheme of molecular orbitals of ethene and (b) the corresponding energy diagram. The  $sp^2$  hybrid orbitals of carbon form directed  $\sigma$  bonds whereas the former  $p_z$  orbitals (violet) form delocalized  $\pi$  bonds. Adapted from Refs. [27, 28]

molecular orbital (HOMO) and the lowest unoccupied molecular orbital (LUMO) is denoted as energy gap ( $E_g$ ). For lower and higher lying orbitals the notations HOMO-1, HOMO-2, ... and LUMO+1, LUMO+2, ... are commonly used. Planar aromatic molecules often feature large frameworks of conjugated bonds, i.e., resonance structures of alternating single and multiple bonds, which can be described by the hybrid orbitals introduced here. The stronger the degree of delocalization of the  $\pi$ -electron system, the more the electronic gap shrinks, which can even make the visible (Vis) and near-infrared spectral region (NIR) available for light absorption (and emission). Such molecules are thus denoted as dyes.

## 2.2 Used Molecular Substances

The organic dye molecules 3,4,9,10-perylene-tetracarboxylic-dianhydride (PTCDA) and tin(II)-phthalocyanine are employed in this work. Their skeletal formulas are shown in Tab. 2.1. These molecules have been chosen primarily because of their prototypical character in many respects. Especially in the field of organic molecular beam epitaxy, comprehensive literature data is available. [29–31] The molecules are known to form highly ordered monolayers on various substrates in a flat-lying adsorption geometry. The layers are naturally different in their structures depending on the specific adsorbate-substrate combination and preparation conditions. For the studies in Chp. 4, the ability of these molecules to form epitaxial organic-organic heterostructures is of particular importance. [32–36]

**Table 2.1:** Molecular substances used in this work.

acronym	full name	skeletal formula
PTCDA	3,4,9,10-perylene-tetracarboxylic-dianhydride	
SnPc	tin(II)-phthalocyanine	

PTCDA was purchased from Sigma-Aldrich, SnPc was provided by Dr. A. Schöll and Dr. C. Sauer. The molecules were purified by several cycles of temperature-gradient vacuum sublimation. After introducing the molecules to the ultrahigh-vacuum chambers, they were thoroughly degassed prior usage.



# 3 Methods and Devices

## 3.1 Organic Molecular Beam Epitaxy

Organic Molecular Beam Epitaxy (OMBE) is a technique to grow epitaxial layers of very high chemical purity and structural precision. Organic molecules are evaporated under ultrahigh-vacuum conditions on a substrate with the ability of *in situ* growth monitoring and control. Epitaxy thereby refers to the growth of crystalline layers that have a well-defined and reproducible orientation with respect to the underlying substrate. The epitaxy matrix  $\mathcal{C}$  mathematically relates the real-space adsorbate and substrate lattices with the lattice vectors  $\mathbf{a}_1, \mathbf{a}_2$  and  $\mathbf{s}_1, \mathbf{s}_2$ , respectively:

$$\begin{pmatrix} \mathbf{a}_1 \\ \mathbf{a}_2 \end{pmatrix} = \mathcal{C} \cdot \begin{pmatrix} \mathbf{s}_1 \\ \mathbf{s}_2 \end{pmatrix} = \begin{pmatrix} c_{11} & c_{12} \\ c_{21} & c_{22} \end{pmatrix} \cdot \begin{pmatrix} \mathbf{s}_1 \\ \mathbf{s}_2 \end{pmatrix} . \quad (3.1)$$

The adsorbate layer can be of the same or different chemical composition, hereafter denoted as homo- and heteroepitaxy, respectively.

Epitaxial growth is driven by the minimization of total energy by self-organization. Beside the energy gained by the mere adsorption, an additional energy gain can be attributed to epitaxial alignment. Both together are denoted as adsorption energy, which depends generally on molecule-molecule as well as molecule-substrate interaction. From this it can be already inferred that the specific orientation of the adsorbate may be the result of a delicate balance of parameters having an effect on the overall energy gain, e.g., substrate lattice constants, symmetry, and so forth. [25]

In the framework of rigid lattices, the origin of the energy gain upon a specific registry is well-understood in terms of adsorbate and substrate reciprocal lattice point coincidences. [25] Based on such coincidences, the following epitaxial hierarchy is applied [21, 23, 37]:

- *Commensurism* - all adsorbate lattice points lie on substrate lattice points. The epitaxy matrix consists of integer values only.
- *Coincidence I or point-on-line (POL) coincidence* - all adsorbate lattice points lie on one primitive family of lattice lines of the substrate.
- *Coincidence II or commensurate super cell* - a commensurate super cell can be constructed. The epitaxy matrix contains rational values only.
- *Line-on-line coincidence* - all adsorbate lattice points lie on non-primitive lattice lines of the substrate.
- *Incommensurism* - The overlayer is incommensurate if none of the above epitaxy modes is present.

For all structures investigated in this work, the epitaxy modes listed describe the experiments sufficiently well. However, adsorbate-substrate combinations exist where the approach of rigid lattice epitaxy fails. In certain cases, the adsorbate atoms or molecules are slightly displaced from an ideal lattice, which need to be accounted for by other concepts, e.g., static distortion waves. [38]

The epitaxial films investigated in this work were grown on single crystals, e.g., Ag(111), prepared by repeated Ar<sup>+</sup>-sputtering and annealing cycles according to Ref. [39]. Each substrate preparation was checked by means of low-energy electron diffraction (LEED) prior to film deposition. The molecules were deposited under ultra-high vacuum conditions (base pressure 10<sup>-10</sup> mbar) from effusion cells with temperature stabilized ( $\pm 1$  K) crucibles. The deposition rates were approx. 0.1 ML per minute.

## 3.2 Optical and Electronic Characterization

### 3.2.1 Differential Reflectance Spectroscopy (DRS)

Differential Reflectance Spectroscopy (DRS) is a variant of optical absorption spectroscopy. This technique was originally utilized for *in situ* studies of surface reactions occurring upon adsorption of diverse atoms and small molecules on metal and semiconductor surfaces. [40–45] In recent years, this method has been also successfully



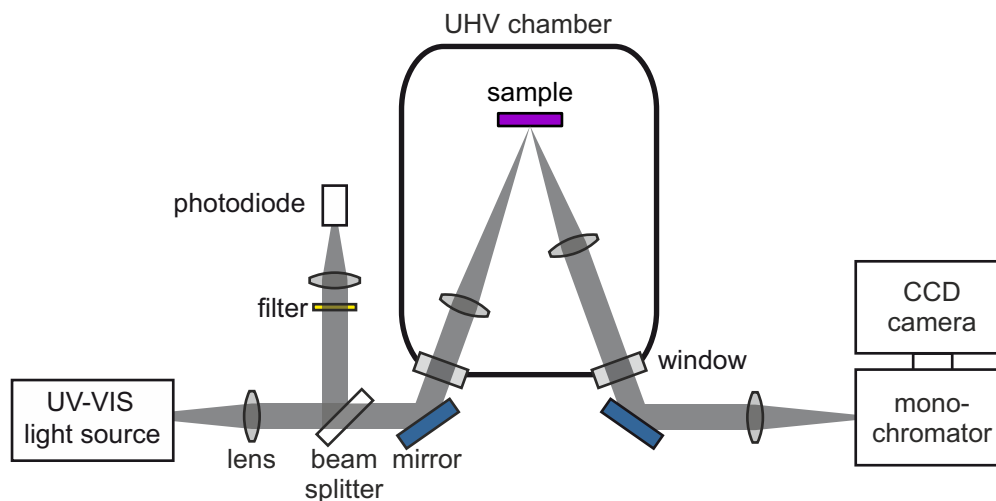


**Figure 3.1:** Realization of our DRS setup, schematically. Detailed information of the components can be found in Refs. [46, 47]. Modified from Ref. [46]

employed for the adsorption of large organic molecules and polymers. The variety of possible applications of DRS has been extensively reviewed previously. [46, 47] The realization of our DRS setup is schematically shown in Fig. 3.1.

DRS probes optical properties of (ultra)thin films. The measured optical transitions are directly related to the electronic structure of the molecules, however, the transition energies thereby differ noticeably from the energetic separation of the electronic levels (cf. Fig. 2.1 (b)). Attractive *Coulomb* interaction between excited electrons and the corresponding holes result in (neutral) quasi-particles, often denoted as excitons. The optical gap, i.e., the HOMO-LUMO fundamental transition is thus  $E_{\text{opt}} = h\nu = E_g - E_B$ , where  $E_B$  is the binding energy of the excitons. Due to weak dielectric screening in organic materials,  $E_B$  can be relatively high ( $\sim 1\text{ eV}$  [48]) compared to inorganic material.

A variety of effects are known to influence the optical transition energies of the molecules. For instance, excitonic coupling may significantly alter the optical fingerprint upon molecular (physical) aggregation. Also intra-molecular vibrations and rotations can be excited giving rise to a fine structure in optical spectra. These effects are known to depend sensitively on the specific molecular arrangement. Different phases and polymorphs of organic material can thus be easily distinguished. [49] In the limit of ultrathin films, interface effects may manifest in the optical spectra,

e.g., (integer) charge transfer and interface hybridization, both yield distinct features, which would not occur in the absence of these effects. [50] DRS can further help to distinguish between the two extreme cases of bonding to surfaces, i.e., physisorption and chemisorption, of large aromatic molecules and even intermediate cases are detectable. [51, 52]

The differential reflectance spectrum (DRS) relates the reflectivity  $R(E, d)$  of a substrate covered with a film of thickness  $d$  to the reflectivity  $R(E, 0)$  of the pristine substrate:

$$\text{DRS}(E, d) := \frac{R(E, d) - R(E, 0)}{R(E, 0)} . \quad (3.2)$$

All spectral quantities are considered as a function of photon energy  $E$ . Defining a quantity as in Eq. 3.2 has the advantage that no absolute reflectivities need to be measured, which can be rather challenging, if not impossible in certain cases. [41]

Reflectivities  $R = |\hat{r}|^2$  are related to the reflection coefficient  $\hat{r}$ , which is given as the ratio of electric-field amplitudes of the reflected and incident waves. For a single interface, the reflection and transmission coefficients are given by the *Fresnel* formulas. Generally, they depend on the optical functions of the materials at the interface, on the angle of incidence ( $\Theta$ ), and polarization (p and s) of the light. For calculating the reflection coefficient of a real system, e.g., a film on top of a substrate, it is necessary to sum up all reflected parts of the incident wave. Multiple internal reflections possibly need to be considered, e.g., an incident wave is partially reflected at the first interface of a film; the transmitted part propagates through the material, and is once more reflected and transmitted at the backside interface and so forth. The superposition of internally reflected and transmitted waves may cause interference effects.

DRS signals often cannot be intuitively interpreted in terms of the optical absorption behavior of the deposited film due to complicated dependencies in the optical functions of the adsorbate and the substrate. In fact, the DRS can be positive, negative, and even zero, depending on the specific combination of optical functions and the spectral region considered. The dependencies of the DRS signal shall be demonstrated by means of the calculated DRS signals for the same hypothetical film on different substrates (no adsorbate-substrate interaction considered) shown in Fig. 3.2. Accordingly, all spectra appear different, i.e., the peak height ratios and the peak positions, and also the overall signal heights differ by up to one order

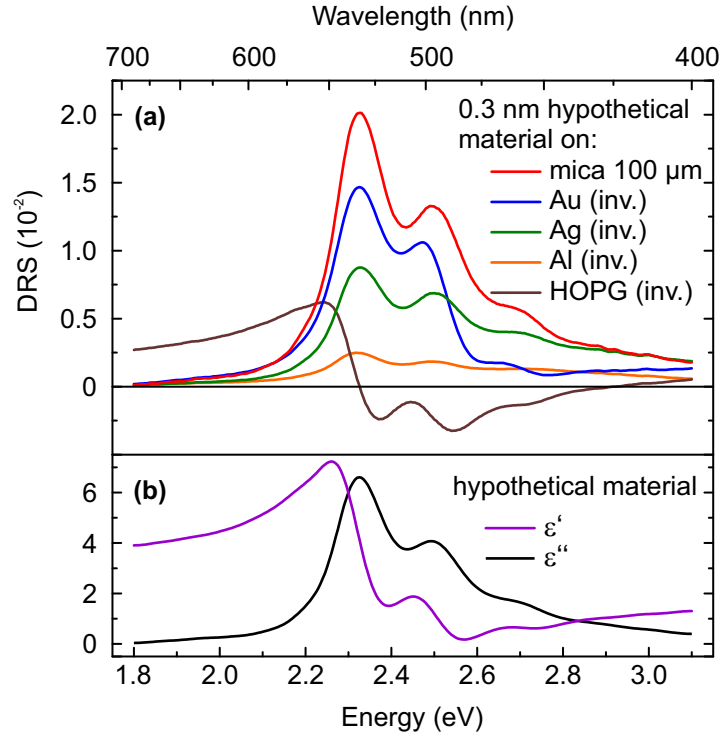


**Figure 3.2:** (a) Calculated DRS signals for the same hypothetical film on different substrates. The optical functions  $\epsilon'(E)$  and  $\epsilon''(E)$  of the film are shown in (b). The DRS signals were inverted (i.e., multiplied by  $-1$ ) for the opaque substrates.

of magnitude. Consequently, the sensitivity of this method depends on the specific adsorbate-substrate combination. For a quantitative analysis of the optical absorption behavior of a film, the corresponding optical functions need to be extracted, e.g., the complex dielectric function  $\hat{\epsilon} = \epsilon' - i\epsilon''$  with  $\epsilon'$  and  $\epsilon''$  as the real the imaginary parts, respectively, and  $i$  refers to the imaginary unit. The complex dielectric function is related to the complex refractive index  $\hat{n} = n - ik$  by  $\hat{\epsilon} = \hat{n}^2$  for non-magnetic materials at optical frequencies. The analytic expression of the DRS is typically rather complicated such that it is in general impossible to determine optical functions analytically. In the following, two approaches for the determination of optical functions shall be briefly reviewed.

The first approach rely on a simplification of the analytical description of the DRS as derived in Refs. [41, 54]. This has been done for the simple case of a three phase system *vacuum/thin film/substrate*. The substrate is considered as semi-infinite, which means that its light absorption is sufficiently high such that reflections at the

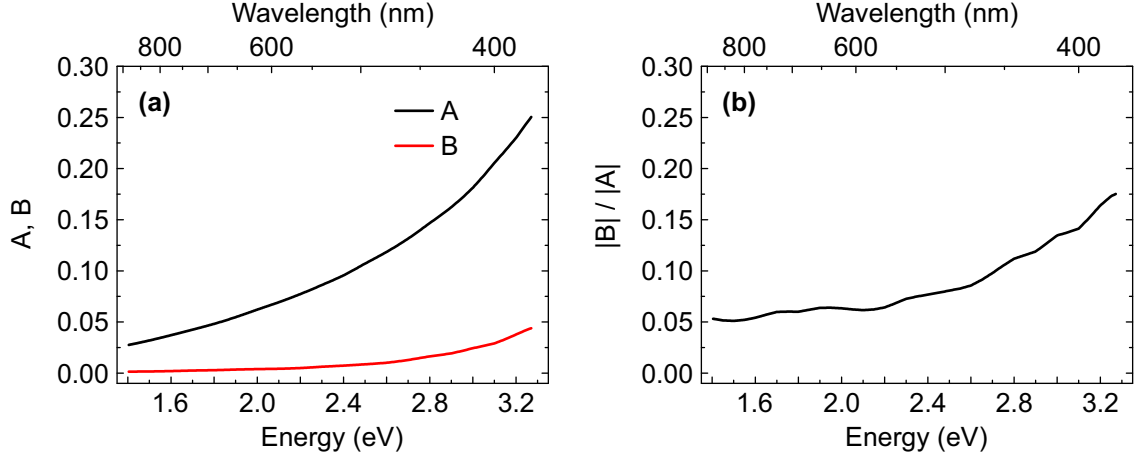


**Figure 3.3:** (a) Spectral coefficients  $A(E)$  and  $B(E)$  and (b)  $|B|/|A|$  for Ag based on the  $n$  and  $k$  values from Ref. [53].

substrate backside can be neglected. In the limit of ultrathin films (film thickness  $d$  is much smaller than the wavelength  $\lambda = hc/E$ ,  $h$  is the Planck constant,  $c$  is the speed of light in vacuum, and  $E$  is the photon energy) and under normal incidence of light, the DRS can be approximated by:

$$\text{DRS} \approx -8\pi \frac{d}{\lambda} [A \cdot \epsilon''_{\text{film}} + B \cdot (\epsilon'_{\text{film}} - 1)] \quad , \quad (3.3)$$

with the two spectral coefficients  $A(E)$  and  $B(E)$ , which only depend on the substrate optical functions:

$$A = \frac{(1 - \epsilon'_{\text{sub}})}{\epsilon''_{\text{sub}} + (1 - \epsilon'_{\text{sub}})^2} \quad , \quad (3.4)$$

$$B = \frac{\epsilon''_{\text{sub}}}{\epsilon''_{\text{sub}} + (1 - \epsilon'_{\text{sub}})^2} \quad , \quad (3.5)$$

with  $\hat{\epsilon}_{\text{sub}}$  and  $\hat{\epsilon}_{\text{film}}$  being the dielectric functions of the film and the substrate, respectively. One immediately see from Eq. 3.3 that the DRS may depend on both, the real and imaginary part of  $\epsilon_{\text{film}}$  depending on the ratio between the two coefficients  $|A|$  and  $|B|$ . If the condition  $|B| \ll |A|$  is fulfilled for the substrate optical constants in a certain spectral region, the DRS there can be further simplified to:

$$\text{DRS} \approx -8\pi \frac{d}{\lambda} A \cdot \epsilon''_{\text{film}} \quad , \quad \text{for } |B| \ll |A| \quad . \quad (3.6)$$

In practice, the condition  $|B| \ll |A|$  is typically valid for substrates that are optically transparent and is not necessarily valid for opaque substrates. However, small spectral regions may exist where this condition is sufficiently fulfilled, e.g.,  $|B|/|A|$  for silver is in the order of magnitude of 1/10 in the spectral range shown in Fig. 3.3.

This approximation is particularly useful since it allows for an analytical determination of  $\epsilon''_{\text{film}}$  from DRS data in certain cases. The prerequisites for applying the approximations cannot always be fulfilled, thus, numerical methods need to be considered. A numerical algorithm for the determination of optical functions from DRS has been introduced in Refs. [47, 55]. The basic idea is to numerically minimize the following objective function by means of the *Levenberg-Marquardt* algorithm [56]:

$$\delta := \sum_{i=1}^N [\text{DRS}_{\text{exp}}(E_i) - \text{DRS}_{\text{theo}}(n(E_i), k(E_i))]^2 \rightarrow \min \quad (3.7)$$

where  $\text{DRS}_{\text{exp}}$  is the experimental data and  $\text{DRS}_{\text{theo}}$  the calculated quantity being fitted by varying the refractive index  $n$  and extinction coefficient  $k$  of the adsorbate film.  $\text{DRS}_{\text{theo}}$  can be derived conveniently by using the generalized matrix formalism as introduced in Ref. [57]. This is well-suited for calculating complex layer systems, e.g., stacks of coherent and incoherent layers. It is important to reduce the number of parameters to be optimized since the two spectral quantities, namely  $n$  and  $k$ , cannot be derived simultaneously in an unconstrained fit from only one spectral function ( $\text{DRS}_{\text{exp}}$ ). Various attempts can be found in the literature to cope with this issue. Dispersion models, e.g., a *Lorentzian* oscillator model, are often used with the advantage of a strong reduction of free parameters. [58] However, the need of a model restricts the applicability of the algorithm significantly. Thus, a dispersion-model-free approach is used in this work. This relies on the fact that  $n$  and  $k$  are not independent from each other; in a linearly responding system, they are connected by a so-called *Kramers-Kronig* transformation (KKT), which is based on the principle of causality. The  $n(E_i)$  spectrum in Eq. 3.7 is thus replaced by the KKT, which depends solely on the  $k$  spectrum and the photon energy. [47] Besides technical difficulties of the numerical evaluation of the KKT [59], integration over an unlimited energy interval would be necessary which is, of course, not accessible by any experiment. This problem, however, can be solved under the condition that the measured energy interval covers the considered absorption bands of the film entirely. [55] This

cannot be perfectly fulfilled in practice, but transitions lying outside of the measuring interval should be as far as possible from the boundaries of the measured energy interval. In the case of organic material, this can often be ensured since absorption bands are usually sufficiently narrow. The KKT is thus calculated by using the data in the measured energy interval whereas the contribution of transitions lying outside are accounted for by a non-spectral offset parameter  $n_{\text{offset}}$ , which is also fitted to the data. For this purpose, it is usually necessary to provide one additional constraint, e.g., the value of  $k$  at a certain energy. The reliability of the numerical evaluation of the KKT can be increased by suitable extrapolation of the  $k$  spectrum. [47, 55] The numerical algorithm thereby converges to a *Kramers-Kronig* compatible set of optical functions, which constitute the best description of the measured DRS on the basis of the used thin film model.

The optical functions determined from DRS data are sensitive to drift effects stemming from the experimental setup. It has become evident that from the manifold of possible origins (e.g., electrical, mechanical, and thermal influences), lamp intensity fluctuations are mainly responsible for drift effects in the DRS data obtained with our setup. Such drift can easily be misinterpreted in terms of light absorption and may even prevent the algorithm from converging toward a physically meaningful solution. In this work, the data have thus been corrected for drift, either numerically or by a second, independent measurement. The numerical method requires an estimation of the lamp fluctuations on the basis of the DRS signal itself. For this purpose, the spectral regions where the molecular films are likely to show almost no absorption are used for drift correction. For the second method, each reflectance spectrum is normalized by the separately measured intensity of the light source. It has been shown that this approach can significantly improve the accuracy of DRS measurements. [60] The DRS setup used here has therefore been improved in the course of this work. In contrast to Ref. [60], the reference beam detection is carried out by a photodiode, which allows for a non-spectral correction only. This approach is feasible only if the lamp intensity fluctuations are very small and thus the shape of the spectrum remains essentially unaltered over time. In practice, each reflectance spectrum is normalized by dividing by the mean value of the photodiode current  $\bar{I}_{\text{photo}}(\tau) = 1/T \int_{t=\tau}^{\tau+T} I_{\text{photo}}(t) dt$  with the period of accumulation  $T$ . The DRS can then be obtained in analogy to Eq. 3.2, with the difference that the normalized reflectivities  $\hat{R} = R/\bar{I}_{\text{photo}}(\tau)$  are used. An example of the achievable improvement

is shown in the appendix in Fig. A.1. This procedure allows to measure very weak DRS signals in the low  $10^{-4}$  range and even long-term stable monitoring, e.g., of recrystallization processes, becomes feasible.

Detailed information about the used DRS setup can be found in Refs. [46, 47] By using an unpolarized light beam at nearly normal incidence (incident angle is approx.  $20^\circ$ , the in-plane components of the dielectric tensor of the adsorbate film are essentially probed. A polarizer in the incident beam and an analyzer in the reflected beam could principally be used, however, the films investigated in this work are known to show nearly isotropic behavior for in-plane components due to a multiple rotational and mirror domains. An actively cooled 100 W halogen lamp (Osram Xenophot) was operated with a stabilized power supply (Voltcraft HPS-11530). The reflected light was spectrally analyzed by means of a monochromator (Acton Research SpectraPro SP2356) with a charge-coupled device (CCD) attached (Princeton Instruments Spec-10 100BR, liquid-nitrogen-cooled). The reference beam detection was carried out by a photodiode (Osram BPW 21), which is designed to have maximum sensitivity at 550 nm, an current-to-voltage converter based on AD822, and a data acquisition interface National Instruments PCI-6014. The photodiode was operated in zero-bias mode in order to ensure highest linearity between the light intensity and the measured photocurrent.

### 3.2.2 UV-Vis Absorption Spectroscopy

Optical spectroscopy in the UV-Vis spectral region is a widely used technique for the determination of light absorption properties of liquid and solid samples. These are placed into a light beam from which a certain amount of its initial intensity is absorbed by the sample. With the light intensities of the initial and transmitted beams,  $I_0$  and  $I_T$ , respectively, the transmittance  $T$  is calculated as  $I_T/I_0$ . The absorbance  $A$ , also referred to as optical density, is given by  $A = -\log(T)$ . If the light absorption is sufficiently weak, the absorbance can be expressed as  $A = \alpha l$  according to the *Beer-Lambert-Bouguer* law, where  $\alpha = 4\pi k/(\lambda \ln 10)$  is the absorption coefficient at a specific wavelength  $\lambda$  of the light in free space and  $l$  is the path length of the sample. The absorbance in this case is proportional to the extinction coefficient  $k$  of the sample material.

Absorbance spectra of molecules in solvents were acquired at room temperature by means of an *ex situ* UV-Vis spectrophotometer Cary 5000 from Varian. The spectrophotometer was operated in the dual beam mode using a scan rate of 600 nm/min, a data interval of 1 nm resulting in an average time of 0.1 s per data point, and a spectral bandwidth of 2 nm.

### 3.2.3 Photoelectron Spectroscopy (PES)

Photoelectron spectroscopy (PES) is a widely used technique for the characterization of the electronic and chemical properties of surfaces and thin adsorbates. This makes use of the (outer) photoelectric effect, i.e., electrons are emitted from gases or solid surfaces upon absorption of photons with energy  $E_{\text{ph}} = h\nu$ . The electrons are usually analyzed in terms of their kinetic energy  $E_{\text{kin}}$  and/or momentum. The energy balance is given in a single-particle picture by the *Einstein* equation [61] :

$$E_{\text{kin}} = h\nu - E_B - \Phi \quad , \quad (3.8)$$

where  $h$  is the *Planck* constant,  $E_B$  the binding energy of the electron, and  $\Phi$  the work function of the sample. The emitted primary electrons are responsible for distinct features in photoelectron (PE) spectra (PE intensity versus  $E_B$ ) from which the occupied density of states (DOS) can be inferred as shown in Fig. 3.4.

Binding energies measured by PES are given as the difference of the total energy between the ground (initial) state and excited (final) state where the latter is lacking one electron, i.e., a photohole is created. All electrons in the final state thereby relax in order to screen the photohole. Screening thus influences the measured electron binding energies, which is referred to as final-state effects. In a zero-order approximation, it is assumed that the orbitals do not rearrange upon ionization (cf. Koopman's theorem [62]) meaning that  $E_B$  equals the ground state energy of the electron (in the framework of *Hartree-Fock* theory). This assumption is especially applicable for valence band PES where a photohole is rather effectively screened by delocalized electrons, resulting in small relaxation energies. For photoholes in the core level region, however, the screening is much less effective. [63] Especially for this case, additional calculations accounting for even these final-state effects are often needed for a reliable analysis of measured electron binding energies.



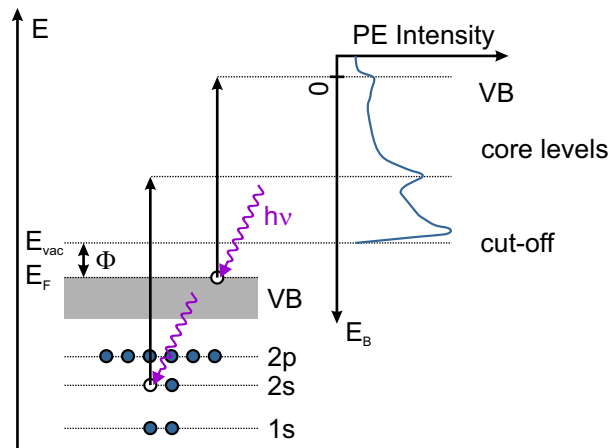


**Figure 3.4:** Principle of photoemission measurements using the example of a metal, i.e., the valence band is extending to the Fermi energy  $E_F$ . Binding energies  $E_B$  are typically measured with respect to the Fermi energy (corresponding to  $E_B = 0$ ). PE spectra additionally show a characteristic secondary-electron background due to inelastic scattering of the primary electrons. At the so-called secondary-electron cut-off, the PE intensity abruptly decreases. This point thus gives an upper limit of the measurable binding energies at  $E_B = h\nu - \Phi$  where  $E_{kin}$  equals zero.

Depending on the photon energy, different variants of PES can be distinguished. For ultra-violet photoelectron spectroscopy (UPS), photon sources providing energies ranging from approximately 10 to 100 eV are used, e.g., helium discharge lamps (He-I $\alpha$  [ $h\nu = 21.22$  eV] and He-II $\alpha$  [ $h\nu = 40.81$  eV]), which enable emission of electrons from the valence band region. Valence band features yield information about electronic properties, e.g., bonding character of orbitals, charge transfers, and charge rearrangements. The work function of the sample can be determined from the secondary-electron cut-off if the photon energy  $h\nu$  is known (cf. Fig. 3.4).

In x-ray photoelectron spectroscopy (XPS), photons with higher energies are used, e.g., x-ray anodes (Al K $\alpha$  [ $h\nu = 1486.6$  eV] and Mg K $\alpha$  [ $h\nu = 1253.6$  eV]) with or without subsequent monochromatization, and also appropriate synchrotron radiation is becoming increasingly popular. Consequently, higher binding energies are accessible, i.e., core levels can be analyzed with a high surface sensitivity, which mainly results from the low escape depth of the photoelectrons. Binding energies of core level electrons are not only element-specific but also sensitive to the chemical state (chemical shift) owing to final-state effects. In addition to the main peaks (m) in such PE spectra, several satellites (s) may appear. From a variety of possible ori-

gins of satellites, the two most important are: (i) a valence electron is additionally excited during the photoemission process and (ii) a formerly unfilled state becomes filled and therefore pulled down in energy in order to (almost) entirely screen the photohole. The scenarios (i) and (ii) are referred to as shake-up and shake-down final-state effects named after the satellites occurring at higher and lower binding energies compared to the main peak, respectively. PE core level lines of organic materials are commonly analyzed by fitting *Voigt* profiles. The *Voigt* profile represents the convolution of a *Lorentzian* and a *Gaussian*, where the former and the latter account for broadening due to the limited lifetime of the photohole and broadening due to the measurement process (limited detector resolution, thermal effects), respectively. An analytical expression of the *Voigt* profile is not available, in practice approximations are often applied, e.g., by a *Gaussian-Lorentzian* product function, in order to reduce the numerical complexity. The ratio between *Gaussian* and *Lorentzian* contributions is kept fixed to 30/70 for the analyses in this work. Strongly broadened satellites were accounted for by pure *Gaussian* peaks. The area of the fitted peaks, also referred to as photoelectron yield  $Y$ , is the integrated PE intensity obtained from the considered chemical component after background subtraction.

For the measurements of core level and valence band spectra, a FOCUS 500 monochromatized x-ray (Al  $K_\alpha$  emission) and a monochromatized UV light source UVLS (He-I $\alpha$  emission) combined with a toroidal-mirror monochromator TMM 304 have been used. The photoelectrons were analyzed using a PHOIBOS 150 2D-DLD hemispherical energy analyzer. All parts were supplied by SPECS. Valence band measurements were done under normal emission. The acceptance angle of the detector is  $\pm 7^\circ$ . The *Fermi* edge region has been fitted by a convolution of the *Fermi-Dirac* function with a *Gaussian* representing the instrumental resolution which was thereby estimated to be  $\approx 50$  meV. For the determination of work functions, secondary electron cut-offs were measured with the sample biased at  $\approx -9$  V. The core level spectra have been processed by means of CasaXPS 2.3.16 PR 1.6.

## 3.3 Structural Characterization

### 3.3.1 Low-Energy Electron Diffraction (LEED)

Low-energy electron diffraction (LEED) allows for precise structural investigations of crystalline surfaces. [64] Electron diffraction can be understood in the framework of wave–particle duality meaning that each quantum particle shows not only classical, but also wave-like properties. The *de Broglie* wavelength  $\lambda = h/\sqrt{2mE}$  accounts for this correlation, where  $h$  is the *Planck* constant, and  $m$  and  $E$  are the particle mass and energy, respectively. In practice, a monochromatic electron beam, provided by an electron gun, is focused on the sample surface whose atoms act as diffraction centers. A prerequisite for the observation of interference effects thereby is that the electron wavelength is in the same order of magnitude as the sample lattice constants, i.e., typically several Ångströms (Å) in the case of an atomic lattice. This means that the primary energy of the incident electrons  $E_{\text{primary}}$  must be in the range of several electron volts (eV) up to 1000 eV. In analogy to the diffraction of light at an optical grating, the atomic (or molecular) lattice thereby serves as a diffraction grating for electron waves resulting in distinct interference maxima of the back-scattered electrons in specific directions. These electrons can be detected by either a fluorescence screen or a channeltron. [65] While the first is used in conventional and microchannel-plate (MCP) LEEDs, the latter is employed in spot profile analysis (SPA) LEEDs. If a fluorescence screen is used, a post-acceleration of the scattered electrons is necessary, which is achieved by applying a high voltage. While most electrons are subject to elastic scattering (the electron energy is maintained), inelastic scattering may also occur under phonon and/or plasmon excitations as well as electron-electron interactions. Inelastically scattered electrons generally contribute as a diffuse background to LEED images and are usually suppressed to a certain extent by a retardation field in conventional and MCP LEED devices.

The recorded diffraction patterns can be understood in the framework of geometric LEED theory which makes use of the reciprocal space. The real space lattice vectors  $\{\mathbf{a}_i\}$  and the reciprocal lattice vectors  $\{\mathbf{a}_i^*\}$  are related by:

$$\mathbf{a}_i \cdot \mathbf{a}_j^* = 2\pi\delta_{ij} \quad . \quad (3.9)$$

For an incident and a scattered electron with the wave vectors  $\mathbf{k}_0$  and  $\mathbf{k}$ , respectively, the conditions for interference maxima are given by the *Laue* equation:

$$\Delta\mathbf{k} = \mathbf{k} - \mathbf{k}_0 = \mathbf{G}_{hkl} = h\mathbf{a}_1^* + k\mathbf{a}_2^* + l\mathbf{a}_3^* \quad , \quad (3.10)$$

where  $(h, k, l)$  is a set of integer values. As a regular LEED pattern stems from elastic scattering, the absolute values of the wave vectors of incident and scattered electrons are equal, i.e.,  $|\mathbf{k}| = |\mathbf{k}_0|$ . Eq. 3.10 can be further simplified by realizing the low escape depth of the electrons which results from strong interactions with the electrons in the solid. Only the first few monolayers and therefore more or less two-dimensional (2D) lattices contribute to the observed diffraction patterns. Consequently, it is sufficient to consider the two surface reciprocal lattice vectors in the *Laue* equation, whereas the third reciprocal lattice vector is degenerate to infinitely dense reciprocal lattice points, so-called rods standing perpendicular on the two other surface reciprocal lattice vectors.

In this work, an MCP LEED device from OCI Vacuum Microengineering Inc. was used. The raw images were corrected for geometric distortions, for the primary electron energy error, and axial distortions if the sample was tilted off-normal. [66, 67] Finally, the LEED patterns were analyzed by means of the LeedLab [68] software.

### 3.3.2 Scanning Tunneling [Hydrogen] Microscopy (ST[H]M)

The scanning tunneling microscope (STM) technique is based on the quantum mechanical tunneling effect. Contrarily to classical physics, this effect enables electrons with an energy  $E$  to overcome a potential barrier higher than  $E$ . The tunneling effect occurs between two separated electrodes which are very close to each other (in the range of nm). By applying a bias voltage, a net tunneling current occurs depending exponentially on the electrode gap. In practice, an atomically sharp metallic tip is used as a probe, which is usually created by either cutting a PtIr wire or by electrochemically etching a tungsten wire. This tip is scanned along a raster pattern  $(x, y)$  in short distance  $(z)$  over an electrically conductive sample surface, which is realized by piezo actuators. Two different operating modes can basically be used for imaging: In *constant current* mode, a feedback loop actively controls the tip-sample distance in order to keep the tunneling current constant. In *constant height* mode,

the feedback loop is switched off and the average tip-sample distance is constant. A three-dimensional image is then created from the  $x$  and  $y$  coordinates of the tip and, depending on the chosen operating mode, from the  $z$  position of the tip or the tunneling current. The interpretation of STM images in terms of the sample topography can be challenging because: (i) a contrast can be observed simultaneously in both, the current and  $z$  image due to the finite response time of the feedback loop whose parameters can be adjusted rather freely, and (ii) the relevant quantity for the measured tunneling current is the local density of states of the sample surface, which is not necessarily constant. The lateral resolution is typically in the range of Ångströms.

Recent developments have been achieved by functionalization of the tip. By intentionally inserting atoms or molecules in the tunneling junction, its characteristics can be altered significantly such that widely differing types of interactions are accessible by STM. [69–71] In this work, scanning tunneling hydrogen microscopy (STHM) was applied as introduced by Temirov *et al.* [69]. This technique goes well beyond conventional STM since hydrogen-functionalized tips clearly show strongly improved resolution when the tips are operated at distances where *Pauli* repulsion forces are dominant. The STM images then feature not only electronic contrast, e.g., molecular orbitals, but also a geometric contrast reminiscent of the corresponding skeletal formula of the molecule can be achieved. [69, 70] This technique may even help to determine stoichiometric ratios of molecules and dopants in ultrathin films. [72]

A commercially available STM (SPECS JT-LT-STM/AFM with KolibriSensors) operated at  $T = 1.1$  K was used. [73] Hydrogen gas was allowed into the chamber up to a pressure of  $10^{-7}$  mbar during STHM measurements by means of a leak valve. The pressure inside the three closed cryoshields (one at 78 K, the others at 4 K and 1.1 K, respectively) may be orders of magnitudes smaller. The hydrogen valve was closed once the contrast in the STM images strongly enhanced and stable operation was achieved as suggested in Ref. [74]. In order to optimize the contrast, achieving the most stable operation, and in order to avoid imaging artifacts, a variety of tunneling parameters as well as different STM tips have been used for the measurements in this work. Only images that are representative of the samples are shown. The STM and STHM images were processed with Gwyddion 2.41, using line and plane corrections as well as different color scalings.

### 3.3.3 Normal Incidence X-Ray Standing Wave (NIXSW)

Normal incidence x-ray standing wave (NIXSW) is a technique that allows for a precise determination of vertical adsorption positions (accuracy  $\sim 0.01 \text{ \AA}$ ) of atoms and molecules on top of a single crystalline substrate taking advantage of elemental and chemical sensitivity of core level photoemission (cf. Subsec. 3.2.3). The discussion of adsorption heights is thereby not only restricted to the respective molecule in its entirety, also different atomic species within molecules can be analyzed separately, making statements about molecular conformations, deformations, and bonding channels possible. [75–82] For the latter, the argumentation thereby relies on the comparison of the vertical adsorption heights with the sum of the van-der-Waals (vdW) radii of the involved atoms. Two main scenarios are often discussed: (i) The adsorption heights are significantly smaller than the sum of vdW radii meaning that the bonding strength can be classified as strong and charge transfers are likely to occur. (ii) If the adsorption heights are comparable or even higher than the sum of vdW radii, the bonding can be classified as weak because vdW interactions clearly dominate.

In the following, a brief introduction of the concept of the standing wave technique shall be given. A more detailed description can be found in reviews [83, 84]. This technique makes use of an x-ray standing field (XSW) which is formed by a coherent superposition of two x-ray waves both having the same wavelength and a fixed phase relation as illustrated in Fig. 3.5. The first one is an incident x-ray wave usually provided by synchrotron radiation, i.e., the wavelength is tunable to a certain extent. The second wave is generated by a *Bragg* reflection of the incident wave at a single crystalline substrate. The periodicity of the XSW is thereby given by the distance of the scatterer planes, for which the condition for *Bragg* reflection  $\mathbf{k} - \mathbf{k}_0 = \mathbf{G}_{hkl}$  is fulfilled. The wave vectors  $\mathbf{k}$  and  $\mathbf{k}_0$  correspond to the *Bragg* reflected and incident waves, respectively, and  $\mathbf{G}_{hkl}$  is a reciprocal lattice vector, cf. Eq. 3.10. The XSW is modulated in the direction of  $\mathbf{G}_{hkl}$ , i.e., perpendicular to the *Bragg* planes, and non-modulated perpendicular to  $\mathbf{G}_{hkl}$ . By sweeping the photon energy through the *Bragg* condition while all other parameters are kept constant, the relative phase between the two complex amplitudes of the waves and thus the positions of nodes and antinodes can be moved in a controlled manner. The intensity of photoelectrons emitted by adsorbate atoms depend on the their relative position to the standing

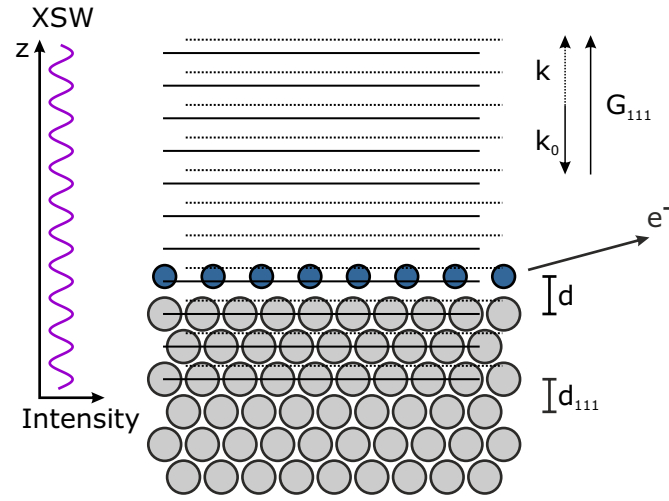


**Figure 3.5:** Principle of the NIXSW technique. An x-ray standing wave (XSW) is created by the interference of an incident and a Bragg-reflected wave characterized by the wave vectors  $\mathbf{k}_0$  and  $\mathbf{k}$ , respectively. Bragg reflection is obtained at a single crystal (here with (111) as the Miller indices of the Bragg plane). The standing field is characterized by a periodic intensity modulation depending on the Bragg plane distance  $d_{111}$ . The photoelectron yield thus depends on the adsorption height  $d$  of the photoelectron emitters (blue). Adapted from Ref. [85]

field, e.g., high photoelectron yield is achieved when an antinode is directly on the plane of atomic centers.

In practice, a series of core level PE spectra is measured by sweeping the photon energy through the Bragg condition. Each obtained spectrum is either simply integrated or decomposed by peak fits into contributions stemming from different chemical species. The PE yields  $Y$  as function of the energy  $E$  of the incident x-rays, also referred to as partial yield curves, are of particular interest. These are proportional, within the dipole approximation, to the intensity of the standing field  $I_{\text{XSW}}$ , which can be modeled as follows [83, 84]:

$$Y(E) \sim I_{\text{XSW}} = 1 + R(E) + 2\sqrt{R(E)}F_C \cos(\nu(E) - 2\pi P_C) \quad , \quad (3.11)$$

where  $E$  is the photon energy,  $R(E)$  is the x-ray reflectivity,  $\nu$  is the relative phase between the amplitudes of the incident and Bragg reflected waves,  $F^H$  and  $P^H$  are the coherent fraction and position, respectively. The separately measured reflectivity  $R(E)$ , also referred to as rocking curve, is fitted to a model of dynamic scattering

theory in order to determine the exact position of the standing wave field with respect to the *Bragg* planes.  $P^H$  and  $F^H$  are usually fitted to the experimentally obtained yield curves. The coherent position  $0 < P^H < 1$  gives the mean relative position of the photoelectron emitters with respect to the *Bragg* plane used. The coherent fraction  $0 < F^H < 1$  thereby belongs to the degree of coherence, i.e., it can be regarded as an ordering parameter. For instance,  $F^H = 0$  can be indicative of vertical disorder, whereas  $F^H = 1$  implies that all photoelectron emitters are on the same coherent position. The adsorption heights can be calculated according to:

$$d = d_{hkl} \cdot (n + P^H) \quad , \quad (3.12)$$

where  $d_{hkl}$  is the *Bragg* plane distance and  $n$  is an integer value. From Eq. 3.11 it can be seen that the partial yield curve is periodic in  $P^H$ . For the determination of adsorption heights, the parameter  $n$  needs to be chosen such that physically plausible results are obtained.

The NIXSW experiments shown in this work have been performed at the end station of the beamline IO9 at Diamond Light Source in Oxfordshire, England. The end station is equipped with a hemispherical electron analyzer (VG Scienta EW4000) which is attached perpendicular to the incident photon beam, a screen with a CCD camera for measuring the x-ray reflectivity. The films were carefully checked for radiation damage prior and after each XSW scan. Significant degradation can be excluded at least on the time scale of the experiments done in this work. The core level spectra have been processed by means of CasaXPS 2.3.16 PR 1.6 and the fits of the partial yield curves were performed using Torricelli 2.9.269 [86].



# 4 SnPc Films on a PTCDA Monolayer Template

*This chapter discusses structural and optical properties of SnPc mono- and multilayers adsorbed on one monolayer of PTCDA/Ag(111). LEED and STM measurements were performed in the course of the master's thesis of Julia Peuker. Additionally, molecular switching experiments were done by her and Susanne Fuchs who evaluated the data in her bachelor's thesis. It was my privilege to supervise the experimental work and data analysis, which were carried out in close collaboration with these two students. Parts of the results have been published in Refs. [52, 87].*

## 4.1 Introduction

Achieving high structural ordering of organic material is of major importance for improving physical properties of thin films, e.g., the charge carrier mobility. A recently developed concept, the so-called molecular templated growth, can be used for this purpose. [88–90] The idea behind is that an additional ultrathin molecular layer is inserted, which can be regarded as a template if the layer(s) adsorbed on top inherits structural properties from this, e.g., molecular orientations, crystal sizes, and morphologies can be controlled to a certain extent. [88–90] This approach offers great potential for tailoring thin film properties, however, finding a template layer material that brings the desired effects is a long process in most cases. This is mainly because of the still poorly understood adsorption behavior at organic-organic interfaces, such as those formed between the template and the top layers.

In this chapter, an insight into the complex adsorption behavior at organic-organic interfaces is provided by the example of tin(II)-phthalocyanine (SnPc) layers adsorbed on a 3,4,9,10-perylene-tetracarboxylic-dianhydride (PTCDA) monolayer (ML) on Ag(111). The influence of the organic-organic interface on the structure

formation of SnPc is elucidated, e.g., the structural ordering of SnPc multilayers can be strongly improved by the templating effect induced by the PTCDA ML. Each experiment shown in this chapter started with a PTCDA ML on Ag(111) prepared by annealing of multilayers at approximately 600 K [32, 34, 35]. SnPc was subsequently deposited on top with the substrate at room temperature (RT). The structures were studied by low-energy electron diffraction (LEED) and scanning tunneling microscopy (STM). The electronic interaction at the SnPc/PTCDA interface as well as the excitonic coupling between SnPc molecules were characterized by differential reflectance spectroscopy (DRS).

## 4.2 Structural Characterization

### 4.2.1 SnPc Submonolayers and Monolayers

In order to investigate the impact of a PTCDA monolayer (ML) on the growth of SnPc multilayers adsorbed on top, the structure formation at the SnPc/PTCDA interface shall be initially addressed. For this purpose, SnPc adlayers were prepared at room temperature (RT) with coverages ranging from dilute submonolayers (subML) up to one ML. The unit cell parameters were subsequently measured with LEED for different sample temperatures between RT and approximately 20 K. The molecular arrangement in the unit cell of each structure was determined by means of STM while the samples were kept at around 1 K. The structural analysis reveal that the SnPc adlayer either forms disordered or distinctly different highly ordered phases depending on the coverage and the sample temperature. The tentative phase diagram is depicted in Fig. 4.1 in order to give a brief overview first, followed by a more detailed discussion of structural data.

#### Disordered phases

Two LEED images are shown in Fig. 4.2, which correspond to SnPc coverages of approximately 0.46 ML and 0.70 ML acquired at 20 K and RT, respectively. The sharp spots can be ascribed to the commensurate herringbone structure of 1 ML PTCDA/Ag(111) [29, 30]; the PTCDA layer thus structurally remains unaltered upon SnPc adsorption. The disordered structure of SnPc is responsible for the diffuse intensity around the specular reflex.

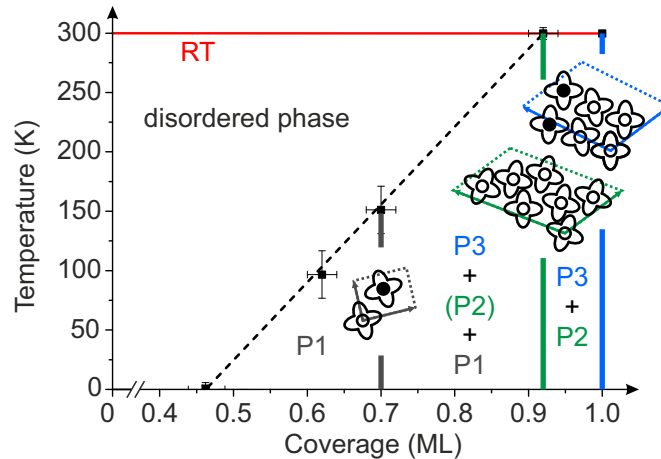


**Figure 4.1:** Tentative phase diagram of SnPc on top of 1 ML PTCDA/Ag(111) as a function of coverage and temperature. The dotted line is a guide to the eye and shall indicate a transition from disordered to highly ordered phases, which are labeled P1, P2, and P3. Each indicated data point reflects a structural transition monitored in temperature-dependent LEED experiments, except of that at  $\sim 1$  K which has been obtained from STM. In the region where highly ordered structures appear, usually more than one phase can be observed simultaneously by means of LEED. The predominant structure at certain points are depicted by sketches of the corresponding unit cells. Molecules in Sn-up and Sn-down configuration are indicated by a bright and dark center, respectively.

The LEED patterns of SnPc can be explained by the formation two-dimensional (2D) gas-phases, where repulsive behavior of intermolecular interactions leads to a maximization of the distances between neighboring molecules. In order to explain the diffuse intensity pattern, a broad distribution of intermolecular distances, as occurring in a fully dispersed system, shall be initially considered. In that case, all frequencies would occur with equal probability in reciprocal space, and thus the LEED intensity would be smooth and unstructured. In reality, however, *Pauli* repulsion forces give rise to a minimal molecule-molecule distance, which corresponds to the disk diameter in the LEED images, e.g., the minimal distance is  $18.5 \text{ \AA}$  for a 0.46 ML SnPc film.

With increasing coverage, the disk increases in diameter and intensity is transferred from the inner to the outer part of the disk, resulting in a more ring-like intensity distribution as observed for 0.70 ML coverage at RT in Fig. 4.2 (a). This observation can be explained by a shrinking of the mean intermolecular separation and a narrowing of the distribution of distances, as previously also reported for other molecules. [91] The thereby associated mean intermolecular distance of  $14.5 \text{ \AA}$

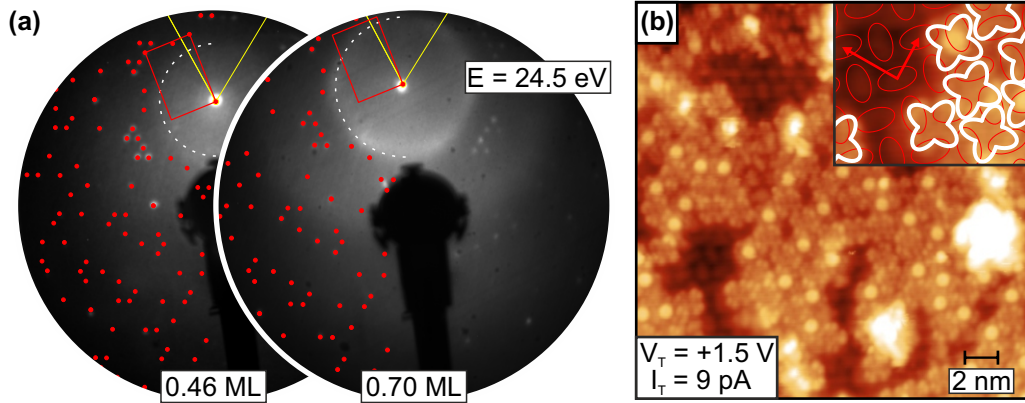


**Figure 4.2:** (a) LEED images for 0.46 and 0.70 ML of SnPc on 1 ML PTCDA/Ag(111) acquired at approximately 20 K and RT, respectively. Simulations of the reciprocal lattice of PTCDA (red dots), the disk- or ring-like intensity distribution (white dotted circle) and primitive reciprocal unit cell of Ag(111) (yellow lines) are superimposed on one half of the images. (b) STM image of 0.46 ML SnPc on 1 ML PTCDA/Ag(111). The SnPc molecules feature submolecular resolution as previously reported for electronically decoupled phthalocyanines. [94] A sketch of the PTCDA herringbone arrangement (red contour lines and basis vectors) is superimposed on the zoomed STM image in the right upper corner. White contour lines visualize the positions of individual SnPc molecules on top.

is already close to that reported for flat-lying phthalocyanines in highly ordered layers. [31, 51, 92, 93] In fact, an angular intensity modulation of the ring in LEED images emerges for coverages slightly higher than 0.70 ML, meaning that the molecules tend to condense into a highly ordered structure with a well-defined orientation with respect to the PTCDA lattice. The STM image shown in Fig. 4.2 (b) resembles a snapshot of that phase transition by imaging a SnPc adlayer with 0.46 ML coverage at a temperature of 1.1 K (cf. phase diagram in Fig. 4.1). At this point of the phase diagram, neither a 2D gas-phase nor a highly ordered structure of SnPc is observed, but loosely packed SnPc islands without long-range order are formed. This image will be discussed in more detail later in Sec. 4.2.1.

Two-dimensional gas-phases have been reported in the literature for different adsorbate-substrate combinations. [31, 91–93, 95–100] For the origin of gas-like behavior, electrostatic interactions are often put forward, either between permanent dipole moments of the molecules [101] or between adsorption induced dipoles arising from charge transfers with the substrate and the push-back effect [31, 91, 102, 103]. In addition, driving forces due to entropy maximization contribute to repulsive intermolecular interaction as well. [96, 104] The free SnPc molecule indeed has a dipole

moment of 0.9 D as calculated by means of density functional theory (DFT) [34], however, this might not play an important role for the formation of the gas-phase observed here. This can be concluded from a very similar system, where SnPc is simply replaced by the planar copper(II)-phthalocyanine (CuPc). This molecule does not feature a permanent dipole moment, nevertheless, the adsorption behavior in the subML region over a wide temperature range is very similar to that observed here for SnPc, a 2D gas-phase is initially formed.[35, 105] It is more likely that adsorption induced dipole moments contribute to repulsive intermolecular interaction, even though the interaction at the SnPc/PTCDA interface has predominantly non-covalent character. [34] Further, it has been shown that partial charges residing on the outer hydrogen atoms of aromatic molecules can lead to *Coulomb* repulsion, while the attractive *van der Waals* forces may be significantly screened in the proximity of a metal surface [106].

### Commensurate phases

Distinct highly ordered phases arise upon cooling depending on the SnPc coverage, i.e., the phases *P1*, *P2*, and *P3* can be obtained. In order to characterize their unit cell parameters, the corresponding LEED images have been analyzed in detail. This has been done by numerically fitting reciprocal lattices to diffraction spots stemming from SnPc by using LEEDLab [68]. This procedure allows for a rather objective and accurate determination of the epitaxy type. For instance, commensurability has not simply been concluded on the basis of seemingly coinciding diffraction spots. If two spots are situated rather close together, they will not be individually resolvable due to finite spot sizes. Thus, the algorithm would treat both spots as a single one, which most likely leads to wrong conclusions. Thus, only those spots of SnPc have been used for the lattice fit that are well separated from other spots such as those of the underlying PTCDA. Getting information about the unit cell orientation just by LEED can be rather difficult when it comes to organic-organic heteroepitaxy. Since a LEED pattern usually represents a macroscopic average of the sample, symmetry equivalent structures are often simultaneously observed, e.g., rotational and mirror domains of PTCDA. Nevertheless, it is thereby highly unlikely that a SnPc domain possesses more than one orientation on top of a PTCDA domain for symmetry reasons (1 ML PTCDA/Ag(111) exhibits an oblique lattice with a unit cell angle

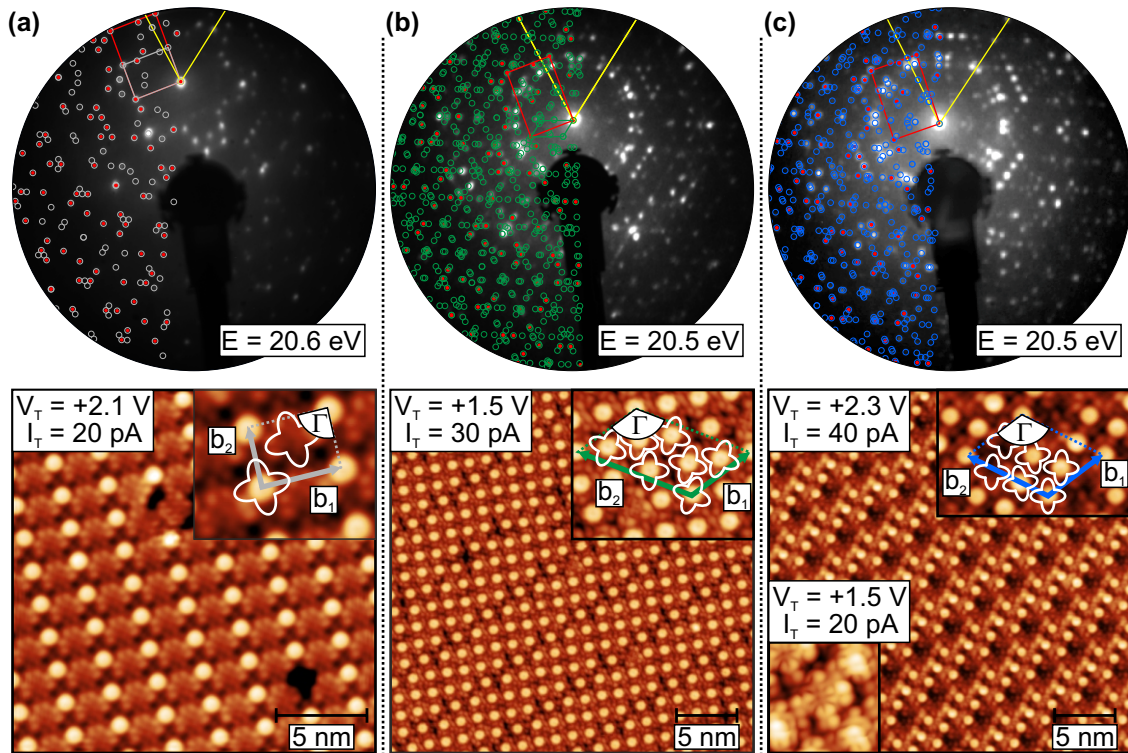


**Figure 4.3:** LEED and STM images of (a) 0.62 ML (phase P1), (b) 0.92 ML (phase P2) and (c) 1.00 ML (phase P3) of SnPc on 1 ML PTCDA/Ag(111). Simulated LEED patterns of SnPc according to the epitaxy matrices in Tab. 4.1, the underlying PTCDA (red dots) under the consideration of symmetry equivalents as well as primitive reciprocal unit cells of Ag(111) (yellow lines) are superimposed on the upper images. The sample surfaces have been tilted to observe the origin of the reciprocal space [(00)-spot]. In the magnified insets in the upper right corner of each STM image, the unit cell vectors and corresponding bases are depicted. Submolecular resolution clearly features nodal planes in the orbital structure as exemplary shown for a Sn-down molecule in the lower left part of the STM image in (c). Adapted from Ref. [52].

of  $89^\circ$ ). In practice, such LEED images can be indeed simulated by different SnPc epitaxy matrices, however, only one of them is most likely physically meaningful. It was that epitaxy relation considered to be relevant that fits to one of the epitaxy modes listed in Sec. 3.1.

The structural analysis shall start with phase P1, which forms large domains over a wide coverage range. For coverages less than 0.7 ML at low temperatures, P1 is exclusively formed on the surfaces. For higher coverages, however, P1 was found to coexist with other highly ordered phases (cf. Fig. 4.1). The LEED image of a

0.62 ML SnPc adlayer acquired for a sample temperature of approximately 20 K is shown in Fig. 4.3 (a). All spots can be assigned to phase  $P1$  with a lattice that is in a commensurate registry with the underlying PTCDA lattice. The epitaxy matrix follows  $\mathcal{C}_{P1} = \begin{pmatrix} 2 & 0 \\ 0 & 1 \end{pmatrix}$ , also referred to as a  $2 \times 1$  superstructure in terms of the so-called *Wood* notation [107].

The unit cell composition shall be determined from the STM image shown in Fig. 4.3 (a). The specific configuration of each molecule is clearly discernible by the contrast stemming in large part from the HOMO-1, which is known to be localized predominantly at the Sn atom. [108–113] Accordingly, the center of Sn-up and Sn-down molecules appear bright and dark, respectively. It can thus be seen that the basis consists of 2 SnPc molecules with opposite Sn configuration. The determination of adsorption sites, however, is difficult since no uncovered PTCDA regions could be imaged simultaneously. Nevertheless, the STM image of the disordered structure in Fig. 4.2 (a) can give at least a hint, since pairs of molecules are reminiscent of the molecular arrangement within the unit cell of phase  $P1$ . Adsorption sites have been determined on the basis of a superimposed PTCDA herringbone arrangement as exemplified in the zoom in the upper right corner of Fig. 4.1 (b). The corresponding lattice has been oriented and scaled on the basis of uncovered PTCDA regions. The adsorption sites and configurations of SnPc thereby correlate such that Sn-down and Sn-up molecules adsorb preferentially between (hollow site) and on top of PTCDA molecules, respectively. Remarkably, pairs of neighboring SnPc molecules often consist of alternating Sn-up and Sn-down configurations, which enables a local compensation of the permanent dipole moments of the molecules. The adsorption sites adopted within an extended domain, however, might differ. Thus, the adsorption sites of the molecules in phase  $P1$  remain somewhat uncertain.

For higher coverages, transitions to phase  $P2$  and  $P3$  can be observed. The LEED images shown in Fig. 4.3 reveal that these phases distinctively differ from  $P1$ , although they are also commensurate. The structures of the phases  $P1$ ,  $P2$ , and  $P3$  are thereby fundamentally different from those obtained for SnPc molecules adsorbed on metal single crystals. [31, 51, 92, 93]. The STM images in Fig. 4.3 (b) and (c) reveal that 7 and 6 molecules are in the unit cells of phase  $P2$  and  $P3$ , respectively, which renders the large unit cells concluded from LEED plausible. The lack of any *Moiré* pattern is a further hint towards (though not a direct proof of) commensurability. Moreover, in both cases very special Sn-up and Sn-down

**Table 4.1:** Structural parameters of the three commensurate phases of SnPc on 1 ML PTCDA/Ag(111).  $\mathbf{b}_1$ ,  $\mathbf{b}_2$ : SnPc lattice vectors;  $\Gamma$ : unit cell angle between  $\mathbf{b}_1$  and  $\mathbf{b}_2$ ;  $\theta$ : SnPc domain angle between  $\mathbf{b}_1$  and the PTCDA lattice vector  $\mathbf{a}_1$ . The SnPc epitaxy matrices are given with respect to the PTCDA interlayer. For each matrix element an uncertainty of  $\pm 0.01$  was determined, representing twice the standard deviation of the numerical lattice fit. The total scaling of each matrix is  $(1 \pm \delta)$  with a scaling error of  $\delta \approx 0.01$ . The matrix  $\mathcal{C}_{PTCDA} = \begin{pmatrix} 3 & 5 \\ -6 & 1 \end{pmatrix}$  was used to simulate the PTCDA/Ag(111) spots. Primitive silver lattice vectors enclose an angle of  $120^\circ$ .  $N$  is the number of SnPc molecules per unit cell and  $\rho$  refers to the number of molecules per  $\text{nm}^2$ . Numbers in parentheses indicate the uncertainty of the last significant digit.

phase	$ \mathbf{b}_1 $ (Å)	$ \mathbf{b}_2 $ (Å)	$\Gamma$ (°)	$\theta$ (°)	epitaxy matrix $\mathcal{C}$	$N$	$\rho$ (1/nm <sup>2</sup> )
<i>P1</i>	25.2(4)	18.9(3)	90.9(1)	73.3(1)	$\begin{pmatrix} 2.00 & 0.00 \\ 0.00 & 1.00 \end{pmatrix}$	2	0.42
<i>P2</i>	31.9(4)	53.6(6)	122.5(1)	36.7(1)	$\begin{pmatrix} 2.01 & 1.00 \\ -4.01 & 1.01 \end{pmatrix}$	7	0.49
<i>P3</i>	31.8(5)	42.1(6)	116.6(1)	36.6(1)	$\begin{pmatrix} 2.00 & 1.00 \\ -3.01 & 1.00 \end{pmatrix}$	6	0.50

motifs occur, which are entirely different from any molecular arrangement of SnPc in known bulk crystal structures [114]. For instance, in phase *P2* all molecules are in Sn-up configuration, whereas 4 Sn-up and 2 Sn-down molecules are in the unit cell of phase *P3*. Remarkably, the molecular areal density, given as the area of the unit cell divided by the number in the respective basis, tends to increase with the coverage. The unit cell parameters of all those commensurate phases are compiled in Tab. 4.1.

To the our knowledge, only three commensurate organic-organic heterointerfaces of large aromatic molecules have been previously found, namely 1 ML CuPc/1 ML PTCDA [35], 1 ML F<sub>16</sub>CuPc/1 ML CuPc [81], both on Ag(111) substrates, and a subML of vanadyl phthalocyanine (VOPc) on top of an iron phthalocyanine (FePc) ML on Au(111) [115]. All of these previously reported examples exhibit unit cell dimensions much larger than those of the  $2 \times 1$  superstructure of SnPc (phase *P1*). At first glance, the occurrence of different commensurate phases seems to be counterintuitive especially in the light of the rather different symmetries of the molecules, e.g., two-fold and nearly planar (PTCDA) versus four-fold and shuttlecock-shaped (SnPc). However, specific epitaxial structures adopted by organic molecules are a consequence of a subtle balance between molecule-molecule and molecule-substrate interactions (cf. Sec. 3.1). Especially in the case of organic-organic interfaces the



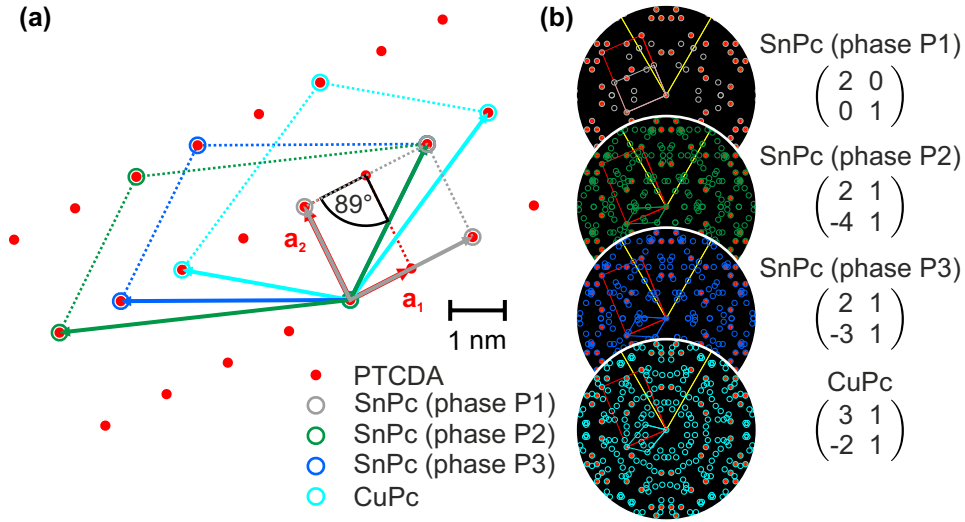


**Figure 4.4:** (a) Real space lattices of the three commensurate phases of SnPc as well as CuPc (Ref. [35]) on top of 1 ML PTCDA/Ag(111). The epitaxy matrices of each structure and simulated LEED patterns under the consideration of PTCDA symmetry equivalents (red dots) are given in (b). Adapted from Ref. [52].

adsorption potential can be highly corrugated, i.e., the energy gain upon a certain epitaxial registry can be strongly adsorption site specific. Therefore, the molecules and whole domains may quickly respond even to slightly changed environmental conditions, e.g., coverage and temperature. The structural transitions between the commensurate phases  $P1$ ,  $P2$ , and  $P3$  are prime examples where not only lattice constants and orientations change, even different molecular configurations (Sn-up and Sn-down) occur. This behavior is not the usual case at organic-organic interfaces. Often other types of epitaxial relations, namely point-on-line (POL) and line-on-line (LOL), are preferentially formed.[23, 116–119]

It can be anticipated that the non-planarity of SnPc plays an important role for the wealth of commensurate phases. This shall be made plausible by a comparison to the same heterointerface, but with the planar CuPc instead of SnPc. In fact, the phase diagrams of both phthalocyanines differ significantly: for low coverages of CuPc, a gas-like phase is initially formed from which the molecules condense into a highly ordered commensurate structure upon increasing coverage and/or cooling to low temperatures. [35] Interestingly, this is the only highly ordered phase reported even up to monolayer coverage. The epitaxy matrix of CuPc follows  $\mathcal{C}_{\text{CuPc}/\text{PTCDA}} = \begin{pmatrix} 3 & 1 \\ -2 & 1 \end{pmatrix}$  [35], while the SnPc adlayer follows  $\mathcal{C}_{\text{SnPc}/\text{PTCDA}} = \begin{pmatrix} 2 & 1 \\ -3 & 1 \end{pmatrix}$  (phase  $P3$ ). Both

lattices have rather comparable appearances as depicted in Fig. 4.4 (a) and even the unit cell areas are identical. It seems as if they could be related to each other by applying a mirror operation at an axis parallel to the long unit cell vector of PTCDA. However, they are definitively not symmetry equivalent since the PTCDA unit cell vectors are not perpendicular to each other but enclose an angle of  $89^\circ$ . Probably even more convincing is the fact that already the LEED patterns differ significantly (cf. Fig. 4.4 (b)). In fact, the noticeable difference between both structures is most likely a consequence of slightly different molecular geometries of SnPc and CuPc. The lower symmetry of SnPc thereby provides another degree of freedom (Sn-up and Sn-down) for energy minimization upon epitaxial growth.

### Molecular switching

Structural transitions in these films make it necessary that molecules change their configurations between Sn-up and Sn-down, which is referred to as molecular switching. [109, 120–124] In the following, an attempt shall be made to estimate the activation energy needed to switch a molecule from one to a another configuration. It is known that single SnPc molecules can selectively be switched under the influence of an STM tip with a certain switching voltage  $V_S$  applied. A key role thereby plays the tip-molecule interaction via HOMO-1 and LUMO+1 of SnPc. [109, 121] Especially the first orbital is known to be strongly localized at the Sn atom and hence to protrude from the molecular plane. [121] Depending on the polarity of the tip voltage, either electrons or holes are injected into the molecule. From the switching voltage  $V_S$ , the bonding situation of the Sn atom to the substrate can be inferred to a certain extent.

The possibility of configurational switching has been demonstrated for SnPc in different bonding environments: For strong bonding scenarios, as it is the case for SnPc directly on Ag(111), switching was feasible from Sn-up to Sn-down by applying  $V_S \leq -1.9$  V. [109] Switching in the other direction, however, was not feasible which has been ascribed to an increased orbital overlap of HOMO-1 with substrate states in the case of Sn-down molecules. [109, 121] Attempts were made to electronically decouple SnPc molecules from the metal substrate prior to switching [109], i.e., bringing the molecules in a weakly bonding environment. It is known that a ML of the same material is appropriate to electronically decouple the second-layer

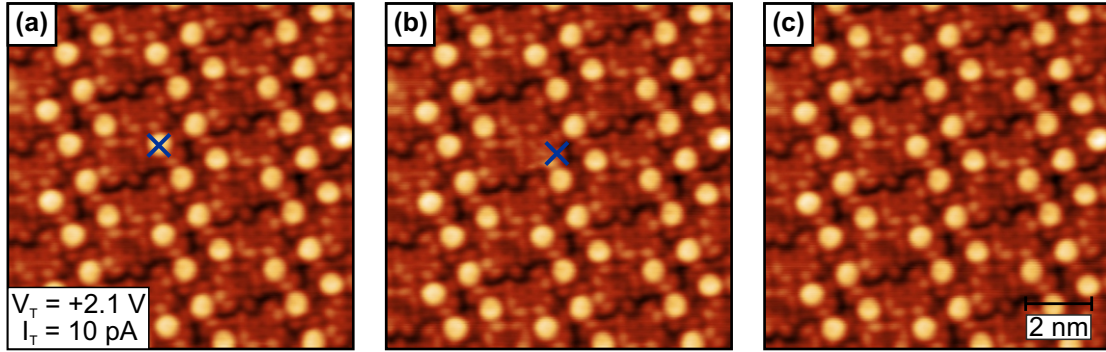


**Figure 4.5:** STM-tip-induced switching of a selected SnPc molecule embedded in an extended highly ordered domain (phase P3). (a) The configuration of a Sn-up molecule shown in (a) has been inverted by applying a negative bias voltage  $V_T \lesssim -1.9\text{V}$ . (b) After switching, the same molecule remains in a Sn-down configuration during scanning with  $V_T = +2.1\text{V}$ . (c) Switching back to Sn-up is feasible by applying a positive tip voltage  $V_T \geq 2.8\text{V}$ . The tip positions while switching the molecules are indicated by blue crosses in the STM images.

molecules. [34, 51, 125] These molecules indeed enable reversible switching, meaning that changing the configuration from Sn-down to Sn-up is permitted, by applying  $V_S \geq +2.8\text{V}$ . Similar results were found for SnPc on InAs(111) [123] and chloroaluminum phthalocyanine (ClAlPc) on graphite [124], with the difference that there the molecule-substrate interaction is already weak enough to enable reversible switching even for first-layer molecules. Two mechanisms are basically discussed in the literature: (i) tunneling of the Sn atom through the molecular plane [109, 123, 124] and (ii) a flip-over of the whole molecule [120]. A comprehensive theoretical study of the inversion of shuttlecock-shaped phthalocyanines in this context is provided in Ref. [122].

Switching of individual SnPc molecules on top of PTCDA/Ag(111) has been investigated for phase P3 because of: (i) Commensurability is advantageous since the number of molecules with different adsorption sites is strongly reduced due to periodic conditions. Consequently, a proper overview can be gained by investigating the molecules within the unit cell, i.e., six nonequivalent molecules need to be considered in that case. (ii) It is the most densely packed phase occurring in the phase diagram up to monolayer coverage. This makes it more unlikely that switching is simply caused by spontaneously changed adsorption sites, molecular rotations or

flip-over processes as brought forward in Refs. [109, 120] It was desired to switch only one molecule embedded in an extended domain. The corresponding molecule has been addressed by positioning the STM tip above. During sweeps of the tip voltage, the tip-sample distance has been kept constant by disabling the feedback-loop (thermal drift effects are minor owing to low and very stable temperatures). In Fig. 4.5, a representative series of STM images is shown, where the configuration of the individual molecule has been changed. Importantly, this was reversibly feasible for each of the six molecules in the unit cell. Sn-down to Sn-up and vice versa thereby require tip voltages of  $V_S \lesssim -1.9\text{ V}$  and  $V_S \gtrsim +2.8\text{ V}$ , respectively. No significant differences in the switching voltages of the six molecules in the unit cell were found. It is noteworthy that only the respective addressed molecule switched while the molecular environment was minor if even negligibly affected. In fact, the voltages are very similar to those observed for switching SnPc from down to up on top of 1 ML SnPc/Ag(111). [108] Switching in the same direction, but at significantly lower voltages was feasible for SnPc on InAs(111)A. [123] The underlying mechanism has been ascribed to an injection of electrons into unoccupied states of SnPc, e.g., LUMO+1. [108] It is likely that thereby intramolecular vibrations are resonantly excited activating the tunneling process of the Sn atom to find a more favored position. [109, 123] It is further thought that the tip-induced electric field assists the switching by coupling to the permanent dipole moment of SnPc. [123]

From the observation that switching from down to up is possible here, it can be concluded that the orbital overlap of HOMO-1 and silver and/or PTCDA states is far from being strong.

### 4.2.2 SnPc Bilayers and Multilayers

The heterointerface of 1 ML SnPc on top of 1 ML PTCDA/Ag(111) was structurally characterized. Briefly, it was been found that the SnPc ML forms a commensurate structure with a relatively large unit cell consisting of 6 SnPc molecules where 4 are in Sn-up and 2 in a Sn-down configuration. In the following, the influence of the PTCDA layer on the structures of thicker films of SnPc shall be elucidated.

The structural analysis starts with a 1.5 ML SnPc adlayer on 1 ML PTCDA/Ag(111). Such films mainly consist of densely packed domains and, very sporadically,

single molecules loosely distributed in the second SnPc ML. Thus, the first SnPc ML intentionally remains partially uncovered.

The STM image in Fig. 4.6 (a) shows a very dilute region of the second ML of SnPc, where single molecules (highlighted by white dashed circles) are adsorbed in a geometry with the shuttles being stacked in a head-to-tail alignment. It seems that the structure of the first ML of SnPc is not affected. This arrangement is reminiscent of quasi-isolated physical dimers in solutions under certain conditions [126, 127] supposedly accounting for a maximum of  $\pi$ - $\pi$  orbital overlap. A comparable behavior has been recently observed also for submonolayers of shuttlecock-shaped vanadyl phthalocyanine (VOPc) on top of a ML of planar iron phthalocyanine (FePc) monolayer on Au(111). [115]

The densely packed domains of the second SnPc ML laterally extend over several hundred nanometers, thereby forming a highly ordered structure with a low defect concentration. It seems that the domains size is only limited by defects of the first ML SnPc predominately located at silver steps (cf. Fig. A.2), apparently acting as a diffusion barrier for second-layer molecules (cf. Fig. 4.6 (b)). Strikingly, lattice defects of the first ML of SnPc can be often observed nearby a domain boundary of the second ML (cf. Fig. 4.6 (c)). Since these defects are certainly not caused by substrate steps, two alternative scenarios remain to be discussed: (i) A domain boundary of the underlying PTCDA and (ii) bilayer (BL) formation structurally rearranging the first ML of SnPc. A domain boundary of PTCDA can be either formed between domains of different orientations (mirror and rotational symmetry equivalents) or between equally oriented domains. The domain boundary in the latter case is also referred to as dislocation. While different domain orientations can easily be excluded by the help of fast *Fourier* transformations (FFT) of the lower left and upper right parts of the STM image in Fig. 4.6 (c), providing evidence for dislocations is more complicated. Since even large-area scans ( $100 \times 100 \text{ nm}^2$ ) of the SnPc ML on 1 ML PTCDA/Ag(111) did not show any comparable pattern of molecular defects that would be indicative of PTCDA dislocations, it is therefore concluded that scenario (ii) is far more likely. This is also corroborated by the fact that the characteristic motif of the (uncovered) first ML of SnPc is not adapted by the second ML of SnPc as shown in Fig. 4.6 (c).

The structure of the SnPc BL has therefore been analyzed in more detail. The LEED image of a 1.5 ML SnPc adlayer in Fig. 4.6 (d) shows spots stemming from

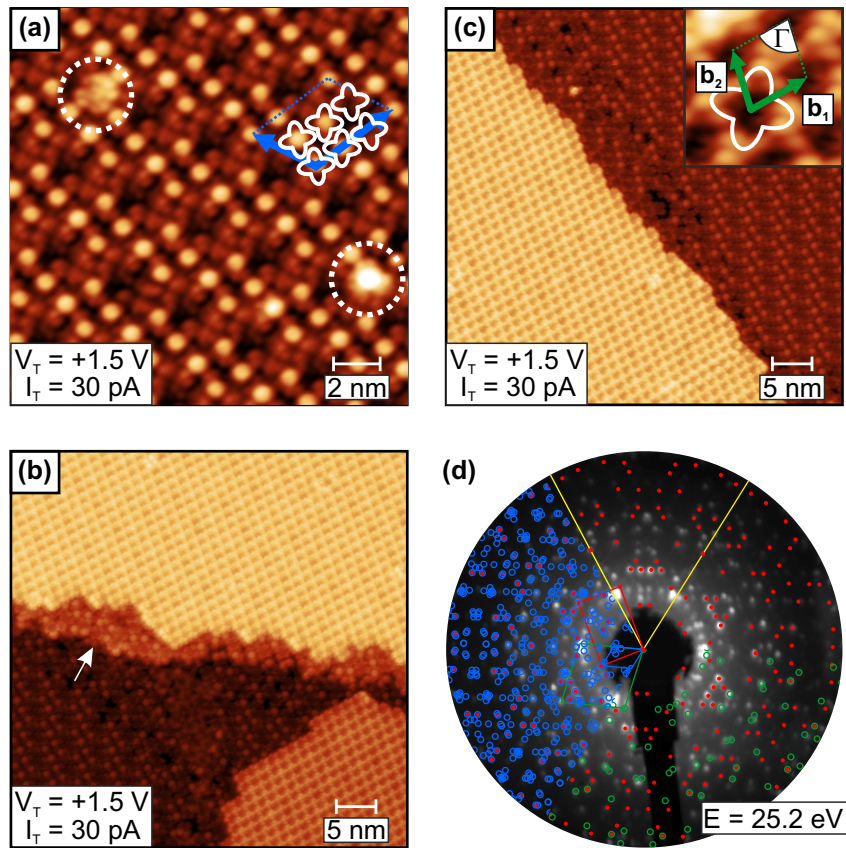


**Figure 4.6:** STM and LEED images of a 1.5 ML SnPc adlayer on 1 ML PTCDA/Ag(111). The second ML of SnPc consists of (a) loosely distributed single molecules in dilute regions (highlighted by white dotted circles) and (b) densely packed highly ordered domains. The white arrow in (b) points at a substrate step edge. The unit cell vectors of the BL and the basis consisting of one molecule is shown in the magnified inset in the upper right corner of (c). A LEED simulation of the SnPc BL (open green circles), the SnPc ML (open blue circles), the 1 ML PTCDA/Ag(111) layer (red dots), and primitive reciprocal unit cell of Ag(111) are superimposed on selected segments of the image in (d).

the SnPc bilayer. The difficulty of the structural analysis, however, is the same as already encountered in Subsec. 4.2.1, i.e., the determination of the epitaxy relation based solely on LEED measurements is ambiguous in general. This issue can be tackled by a combined evaluation of LEED and *Fourier*-transformed STM images. These images can basically be analyzed in full analogy; the only difference between both is that LEED probes a macroscopic average of the sample, the latter approach takes advantage of local resolution of STM. This means that a single domain can be investigated, which substantially facilitates the determination of the epitaxy relation

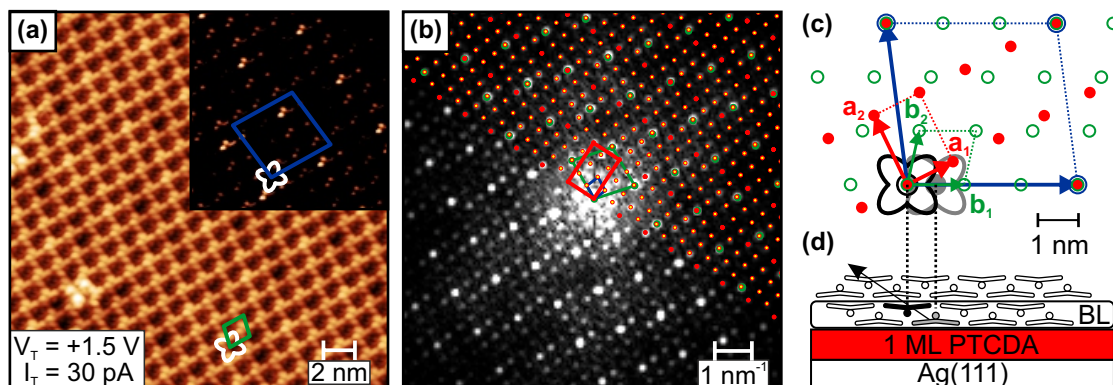


**Figure 4.7:** (a) Zoom of the STM image of the SnPc BL shown in the lower left corner of Fig. 4.6 (c). The upper right part has been strongly contrast enhanced. (b) The corresponding 2D Fourier transformation with a lattice simulation superimposed on one half of the image. The convolution (yellow spots) of the primitive SnPc (green spots) and PTCDA (red spots) lattices has been fitted to the experimental data by varying the lattice parameters. A real-space plot of the SnPc BL is shown in the schematic (c) top- and (d) side-view. The suggested basis of the primitive unit cell of the SnPc BL consists of a Sn-up (grey) and a Sn-down (black) molecule in the first and second ML of SnPc, respectively. The stacking of SnPc layers is illustrated in the side-view. The first BL is indicated by the rounded box. The arrow points in the stacking direction of the quasi-one-dimensional aggregates.

as demonstrated in the following. An STM image containing only one SnPc domain and the corresponding FFT are shown in Fig. 4.7. Strikingly, the FFT contains not only spots stemming from the primitive SnPc lattice of the second ML (green spots), also frequencies (yellow spots) are observed that can be ascribed to the Moiré pattern clearly visible in the strongly contrast-enhanced STM image in the upper right part of Fig. 4.7 (a). In reciprocal space, the spot pattern can thus be mathematically described by a convolution of the SnPc and the PTCDA lattices. [128] This approach already describes all spots of the FFT rather well. No contributions of the SnPc monolayer structure  $P3$  can be found, which unequivocally proves that the first SnPc layer is structurally rearranged upon adsorption of second-layer molecules in sufficiently large quantities.

The lattice parameters determined from FFTs can be affected by drift, which is often unavoidable in STM measurements. However, if the adsorbate as well as the substrate lattices are observed at the same time in an FFT, as it is the case here, the

epitaxy relation can be determined with very high accuracy because both lattices are subject to the same drift-induced distortion. [128] The epitaxy matrix of the second ML of SnPc  $\mathcal{C}_{\text{SnPc}}^{\text{primitive}} = \begin{pmatrix} 1 & -1/3 \\ 2/3 & 5/9 \end{pmatrix}$  contains only rational values indicating a commensurate super cell (SC), often also referred to as higher-order commensurism (cf. Sec. 3.1). The SC can also be identified in the strongly contrast enhanced upper right part of the STM image shown in Fig. 4.7 (a). The epitaxy matrix of the SC follows  $\mathcal{C}_{\text{SnPc}}^{\text{SC}} = \begin{pmatrix} 3 & -1 \\ 1 & 2 \end{pmatrix}$  due to coincidences between the  $(\bar{1}3)$  and  $(30)$  lattice vectors of SnPc and the  $(12)$  and  $(3\bar{1})$  lattice vectors of PTCDA. This is further illustrated in the real-space plot in Fig. 4.7 (c). All epitaxy matrices are given with respect to the PTCDA ML. Since the PTCDA lattice parameters are well known, the adsorbate lattice parameters can be deduced as well. The lattice parameters obtained are compiled in Tab. 4.2.

Structural reorganizations as occurring upon bilayer formation can strongly alter the orbital overlap of adjacent molecules and hence optical and electronic properties are affected as well. It is thus highly desired to identify the molecular arrangement within the SnPc bilayer. The data so far indicate a structural rearrangement of the lower SnPc layer from six molecules in the unit cell towards a structure that is most likely comparable or even the same as in the upper layer. This can be readily justified from the lattices of the upper SnPc layer and that of the PTCDA ML being in a commensurate registry. If the upper and lower SnPc layers were in different registries with respect to PTCDA, it would be clearly visible in the *Fourier*-transformed STM images. An attempt shall be made to describe the SnPc bilayer structure by a two-dimensional lattice and a bimolecular basis with exactly one molecule in each layer. While the upper layer obviously contains only molecules in Sn-down configuration, information about the Sn configurations within the first ML of SnPc is not readily accessible by means of STM.

The molecular arrangement of the bilayer shall thus be inferred from the well-known triclinic bulk structure of SnPc. [114] Strikingly, the unit cell identified for the upper SnPc layer is rather similar to the two-dimensional unit cell of the  $(10\bar{1})$  lattice plane of the SnPc triclinic structure. The corresponding basis there consists in fact of two molecules which are stacked pairwise in a slipped cofacial geometry and the shuttlecocks of adjacent molecules of each pair point towards each other. The molecules are not flat-lying with respect to the  $(10\bar{1})$  lattice plane, but they are tilted by  $\sim 20^\circ$  giving rise to a length difference of  $1.6 \text{ \AA}$  between the two unit



**Table 4.2:** Structural parameters of SnPc on 1 ML PTCDA/Ag(111).  $\mathbf{b}_1$ ,  $\mathbf{b}_2$ : SnPc lattice vectors;  $\Gamma$ : unit cell angle between  $\mathbf{b}_1$  and  $\mathbf{b}_2$ ;  $\theta$ : SnPc domain angle between  $\mathbf{b}_1$  and the PTCDA lattice vector  $\mathbf{a}_1$ . The structural parameters of the BL and the 4 ML SnPc film were obtained from the FFT in Fig. 4.7 and from LEED measurements, respectively. The epitaxy matrix of the SnPc BL is given with respect to the PTCDA lattice, which itself is described by  $C_{PTCDA} = \begin{pmatrix} 3 & 5 \\ -6 & 1 \end{pmatrix}$  relative to the Ag(111) surface. The uncertainties of each matrix element refer to the standard deviation of the fitting routine. The primitive silver lattice vectors enclose an angle of  $120^\circ$ . Numbers in parentheses indicate the uncertainty of the last significant digit(s).

structure	$ \mathbf{b}_1 $ (Å)	$ \mathbf{b}_2 $ (Å)	$\Gamma$ (°)	$\theta$ (°)	epitaxy matrix $\mathcal{C}$
BL	13.99(4)	13.59(4)	77.5(2)	-26.8(2)	$\begin{pmatrix} 1.001(2) & -0.333(1) \\ 0.668(3) & 0.556(2) \end{pmatrix}$
4 ML	13.9(4)	13.4(4)	77.6(2)	-	-
(10 $\bar{1}$ )-plane of triclinic bulk [114]	14.205(10)	12.630(3)	75.40(8)	-	-

cell vectors. In contrast, the unit cell vectors of the bilayer structure,  $\mathbf{b}_1$  and  $\mathbf{b}_2$ , differ by only  $0.4 \text{ \AA}$ . It can thus be expected that the molecules are tilted to a lesser extent and they may even adsorb flat-lying, i.e., the phthalocyanine ring is oriented parallel to the surface. The suggested basis has been superimposed to the real-space plot in Fig. 4.7 (c). It can be seen that the arrangement of stacked molecules in bilayer domains significantly differ from that encountered for single second-layer molecules seen in Fig. 4.6 (a). In extended BL domains, a slipped cofacial geometry is preferred against a cofacial (face-to-face) arrangement, which emphasizes the known tendency of the central metal atoms of phthalocyanines to interact with the mesobridged nitrogen atoms of adjacent molecules. [129]

Further molecules adsorbed on top of the first BL do not grow in a layer-by-layer mode (cf. Sec. 3.1) anymore, but they tend to grow BL-wise. The configuration is thereby Sn-up and Sn-down in odd- and even-numbered layers, respectively. A similar behavior has been found for multilayers of SnPc on Ag(111) [108] and for PbPc on graphite [130]. In Fig. 4.8 (a), an STM image of the fourth ML of SnPc is shown where all molecules in the topmost layer are in Sn-down configuration. A Sn-up molecule, that is a representative of the third ML, is indicated by the white dashed circle in Fig. 4.8 (a). This molecule is slipped by about half of the length

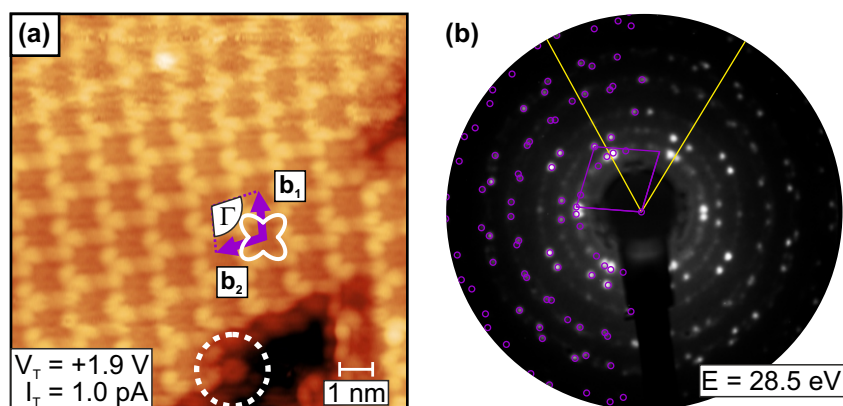


**Figure 4.8:** (a) STM and (b) LEED images of a SnPc adlayer on 1 ML PTCDA/Ag(111) with nominal thickness of 4 ML. The surface unit cell of the fourth ML is superimposed to the STM image with the basis consisting of a Sn-down molecule in the upper layer. A Sn-up molecule that is a representative of the third ML is indicated by the white dashed circle. In (b) a LEED simulation of SnPc multilayers (purple) is superimposed to image. The primitive reciprocal unit cell of Ag(111) (yellow lines) is also indicated.

of the longer unit cell vector compared to the respective molecule in the topmost layer. This arrangement thus mimics the suggestion structure of the first BL (cf. Fig. 4.7 (c)). In fact, the lattice parameters obtained from the LEED measurement in Fig. 4.8 (b) are rather similar to those of the first BL. Only the second unit cell vector seems to be smaller by  $0.2 \text{ \AA}$  which, however, might be insignificant due to the much higher experimental uncertainty.

### 4.3 Optical Properties

The structural characterization in the previous section evidences that SnPc films grow layer-by-layer up until completion of the first BL, whereas three-dimensional crystallites are formed in thicker films. Since DRS measurements probe a macroscopic area of the sample surface, film thickness specifications in units of MLs are inappropriate. Monolayer equivalents (MLE) shall thus be introduced here, where 1 MLE refers to the amount of SnPc molecules that is necessary to entirely cover the surface with a single layer of phase *P3* (see above). For the sake of consistency in the following discussion of DRS data, SnPc film thickness specifications are always given in units of MLE.

### 4.3.1 SnPc Monolayer

The imaginary part of the dielectric function  $\epsilon''$  of SnPc on 1 ML PTCDA/Ag(111) is shown in Fig. 4.9 for film thicknesses ranging from submonolayers up to 1 MLE. These spectra have been numerically extracted from the DRS data by means of the algorithm introduced in Subsec. 3.2.1. A two-layer model has been applied using the effective film thicknesses of a monolayer of PTCDA and SnPc, 3.2 Å [131, 132] and 3.4 Å [114, 133], respectively.

The spectrum of 1 ML SnPc (cf. red curve in Fig. 4.9 (a)) shows a main peak and a shoulder at 1.88 eV and 1.71 eV, respectively. This signature can be assigned to the Q-band of phthalocyanine monomers as likewise observed on an inert mica substrate or in appropriate solutions, e.g., benzene (cf. Fig. 4.9 (d)). The monomer behavior is thereby a consequence of (i) the ability of the PTCDA ML to electronically decouple SnPc from the metal substrate, while the electronic interaction of SnPc with PTCDA is supposed to be minor at most, and (ii) the excitonic coupling is quite small within the layer as well as across the heterointerface. Excitonic coupling in this context refers to *Coulomb* interaction between molecules where excited states are involved. The impact of this coupling mechanism to optical absorption spectra can be qualitatively understood in the semi-classical framework of *Kasha's* theory [134], albeit simplified since the specific appearances of orbital overlaps are neglected. The interactions between molecules are instead discussed on the basis of transition dipole coupling. The corresponding transition dipole moments account for spatial charge rearrangements upon optical excitation of the molecules. Moreover, the dipole moments are often even treated as point-like to further reduce the complexity. In the case of phthalocyanines, two transition dipole moments need to be considered, both are orthogonal to each other and they are lying within the molecular plane. They are energetically degenerate as long as the molecule is isolated. Excitonic coupling in this theory depends on the molecular arrangement, or more precisely, on the distance and orientation of transition dipole moments with respect to each other. From this, it can be realized that excitonic coupling within the first MLE of SnPc is quite small, although the molecules are surrounded by others. The reason lies in the fact that the distance between the centers of gravity of adjacent SnPc molecules, with a value of approximately 1.3 nm, is relatively large.

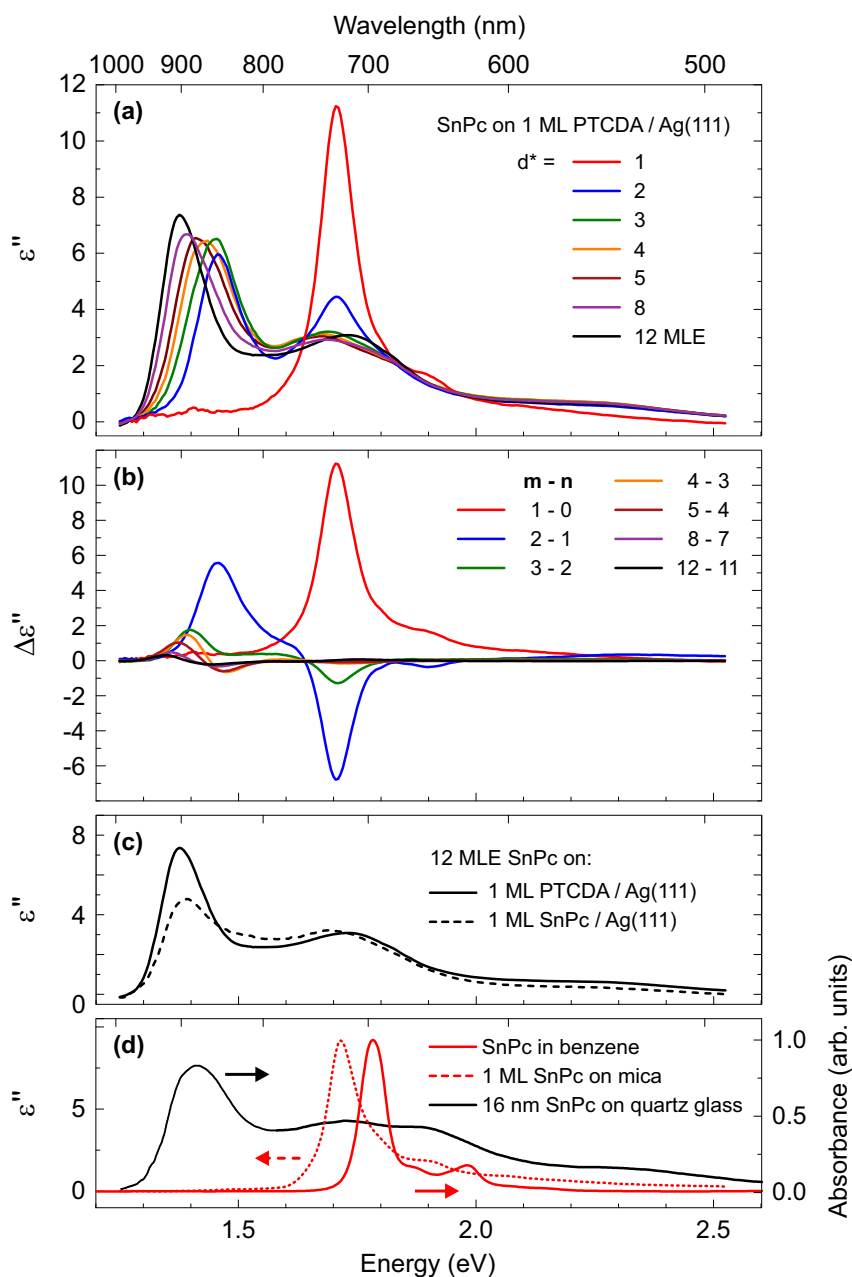


**Figure 4.9:** (a)  $\epsilon''$  spectra of SnPc adlayers on 1 ML PTCDA/Ag(111) numerically extracted from Fig. A.3.  $\Delta\epsilon''$  spectra are shown in (b), labeled according to the scheme  $m - n$  meaning that the differences of the  $\epsilon''$  spectra corresponding to the film thicknesses  $m$  and  $n$  MLE are calculated. (c) For comparison,  $\epsilon''$  of 12 MLE of SnPc on 1 ML PTCDA and 1 ML SnPc, both on Ag(111). (d) Normalized absorbance spectra of SnPc in benzene, 16 nm SnPc on quartz glass [137] and  $\epsilon''$  spectrum of SnPc on inert mica for comparison. The arrows point to the ordinate corresponding to the respective curves.

### 4.3.2 SnPc Bilayer

Upon bilayer formation (1BL equals 2MLE), the  $\epsilon''$  spectra change abruptly. In order to illustrate spectral changes, the differences between  $\epsilon''$  spectra, hereafter denoted as  $\Delta\epsilon''$  spectra, are shown in Fig. 4.9 (b). The spectra are labeled according to the scheme  $m - n$ , meaning that the differences between the  $\epsilon''$  spectra of films with nominal SnPc thicknesses of  $m$  and  $n$  MLEs have been calculated. It can be seen that monomers disappear with increasing film thickness indicated by a negative monomer spectrum in  $\Delta\epsilon''$ . The reason for this sudden spectral transformation is readily explainable considering the distance between the centers of gravity of the molecules. This distance changes drastically as soon as the second SnPc ML starts to grow. A significant overlap of the out-of-plane  $\pi$  orbitals sets in between stacked molecules, which is also referred to as physical aggregation. If the in-plane interaction thereby remains quite weak, the aggregates can be regarded as quasi-one-dimensional. [135, 136] The aggregate size scales with the number of stacked molecules. For instance, two stacked molecules may form a dimer and so forth. The suggested stacking geometry is shown in Fig. 4.7 (d).

This can be qualitatively understood such that every second-layer molecule converts a monomer into a physical dimer upon bilayer formation. The dimers have a characteristic absorption peak at 1.46 eV, the former Q-band of the monomers is thus strongly redshifted. This principally indicates a head-to-tail arrangement of transition dipole moments of the molecules, the aggregates thus having J-type character. This is compatible with the structure suggestion in Fig. 4.7.

It is known that the energetic positions of the two absorption bands depend on the slipping distance. [138] However, understanding the optical spectra can be more complex for the following reasons: (i) The specific appearance of orbitals, especially fine details, are not accounted for in the framework of transition dipole coupling, e.g., the orbital overlap may not change continuously with the slipping distance, but can feature several minima and maxima depending on spatial modulations of orbitals. [139] Especially for non-planar molecules, more geometrical parameters than merely a transition dipole moment can be required, e.g., it can be expected that it is important to account for different Sn-up and Sn-down configurations of adjacent molecules. (ii) The theory only accounts for *Frenkel* excitons, whereas in practice also charge-transfer (CT) excitons may occur. In general, strong orbital

overlap can allow the excitation energy to delocalize, preferentially along directions where the largest electronic dispersion occurs. [140] In fact, a splitting of the HOMO has been found for the SnPc BL on 1 ML PTCDA/Ag(111) [32] and similarly for PbPc on graphite [130]. For the latter, this splitting has been explicitly attributed to relatively strong  $\pi$ - $\pi$  interactions. Consequently, it cannot be excluded that in BLs an admixture of *Frenkel* and CT excitons dictate the optical absorption behavior. [141] (iii) Electron-phonon coupling can strongly change upon aggregation. All these arguments are difficult to account for, especially together in a comprehensive theory. A prime example for such a theory is given for quasi-one-dimensional aggregates of perylene derivatives in Refs. [142–145].

Electronic absorption spectra of SnPc monomers and aggregates have been recently calculated by means of time-dependent density functional theory. [146] The findings relevant for this work shall be briefly given in the following. Those calculations go well beyond *Kasha's* theory since orbital overlaps are considered by means of quantum chemistry methods, i.e., band formation and charge delocalization are included, however, electron-phonon coupling is not. For these calculations, different kinds of dimers were identified to be relevant in aggregates, i.e., convex and concave, depending on the orientation of the shuttlecocks to each other. The structural suggestion in Fig. 4.7 (d) implies convex-type dimers in a SnPc BL. It has been found that for such dimers the HOMO-LUMO gap is strongly reduced due to significant  $\pi$ - $\pi$  orbital overlap. Additionally, the redshifted components mainly stem from HOMO to LUMO and HOMO to LUMO+1 transitions, whereas the peaks in the Q-band region show strong contributions from the Sn atom, i.e., metal-to-ligand charge transfers.

### 4.3.3 Stacked Bilayers

The initial growth of the second BL (3 MLE) causes the low-energy transition band to slightly shift to lower energies by 6 meV and still some monomers are converted into aggregates. Both effects can be clearly seen in the corresponding  $\Delta\epsilon''$  spectrum (cf. Fig. 4.9 (b) (green line)). This means that the absorption properties of the film undergo only minor changes upon adsorption of the second BL. Bearing in mind the strong change from monomers to dimers, orbital overlap must be considerably smaller between the two BLs. This is compatible with PES studies on PbPc/

graphite where the formation of extended bands has been excluded. [130]. Towards completion of the second BL (4 MLE) of SnPc, a more redshifted peak evolves, which indicates the beginning growth of the next BL.

For higher film thicknesses, the low energy absorption band shifts even more towards lower energies down to 1.37 eV for 12 MLE. Since the spectral changes are minor at such film thicknesses (cf. Fig. 4.9 (b) (black line)), the optical properties from there on can be regarded as bulk-like (cf. Fig. 4.9 (d) (black line)). This spectral appearance is already known from other shuttlecock-shaped phthalocyanines in their triclinic crystal structures [147–150] with the difference that the low-energy transition bands of the SnPc films on 1 ML PTCDA/Ag(111) are much less broadened. As reasoned in the literature, a strong redshift and narrowing of the low-energy transition band is a consequence of coherently coupled transition dipole moments of molecules in extended J-type arrangements. [126]. It is thus plausible that effects like finite domain sizes, defects, and disorder limit the number of molecules being coherently coupled, which in turn renders the peak width indicative for the structural quality.

The influence of structural ordering on the optical properties of SnPc multilayers films shall be demonstrated by replacing the PTCDA with a SnPc ML, i.e., a pure SnPc multilayer film on Ag(111). The SnPc ML in contact with Ag(111) also serves as a decoupling layer for further SnPc molecules in terms of electronic interaction. [51] Hence, monomer behavior is also observed for the first decoupled ML. The optical signature of the multilayers, however, is broadened, less intense in the near-infrared (NIR), and the low-energy transition band is less redshifted (cf. Fig. 4.9 (c)) compared to the film where the PTCDA interlayer is used. Yet, the optical absorption behavior is essentially that of a polycrystalline film on quartz glass as shown in Fig. 4.9 (d). The differences in the optical properties of the multilayer films can be attributed to dissimilar structures: while the SnPc film on top of the PTCDA ML yields sharp diffraction spots even for more than 10 MLE of SnPc (cf. Fig. A.4), it is the opposite for the pure SnPc film, i.e., no long-range ordering is observed for such film thicknesses. The latter is in agreement with previous studies, where a mixture of dissimilar phase each having different unit cell compositions and orientations have been observed already for the second ML of SnPc/Ag(111) [108]. An effective broadening of the absorption spectrum of the pure SnPc films is caused by (i) different optical absorption properties of each phase and (ii)

small quasi-one-dimensional aggregates due to a small number of molecules being coherently coupled. In conclusion, an intense and narrow absorption band of SnPc multilayers in the NIR can be achieved by strongly improved structural ordering initiated by a PTCDA template layer.

## 4.4 Summary and Conclusion

The structural and optical properties of SnPc layer adsorbed on 1 ML PTCDA/Ag(111) have been comprehensively investigated. It was found that SnPc forms either disordered phases in the case of dilute layers or three distinct commensurate structures for coverages up to 1 ML. Commensurate registries at organic-organic heterointerfaces have been found very sporadically so far [35, 81, 115], therefore, one can regard this system as a prime example for unusual epitaxial growth in this respect. Upon adsorption of the second SnPc ML, the first ML is entirely structurally rearranged. This is all the more remarkable since a super cell of the SnPc BL is also commensurate to the PTCDA lattice. The SnPc BL mimics the molecular arrangement within the  $(10\bar{1})$  lattice plane of the SnPc triclinic bulk structure, namely stacked SnPc molecules in a slipped cofacial geometry. Further molecules on top also arrange BL-wise in similar structures. None of these phases shows any sign of significant electronic interaction with PTCDA or metal states of Ag(111). Yet, the first SnPc ML features monomer behavior, indicating a rather weak bonding environment. The SnPc BL is characterized by a strongly redshifted low-energy absorption band compared to SnPc monomers. This can be ascribed to dimer formation due to significant  $\pi$ - $\pi$  orbital overlap between the molecules in adjacent layers. Further BLs on top, however, alter the optical absorption spectrum only to a minor extent. In other words, the absorption spectrum of the BL already closely resembles that of a multilayer film. It can be concluded that the latter can be regarded as a stack of BLs: While each BL contributes more or less a dimer signature, weak orbital overlap between adjacent BLs is responsible for an additional redshift and narrowing of the low-energy transition band. The latter two effects thereby have the character of transition dipole coupling of the molecules in a J-type arrangement. It has been demonstrated that this effect is more pronounced the higher the structural order is.



It was found that the PTCDA layer has several functions in the studied system: First, it prevents the SnPc molecules from directly electronically interacting with the metal substrate and, second, it modifies the surface potential landscape. The modified surface potential has lower symmetry than that of the pristine Ag(111) surface. This ensures that the SnPc BL grows in only one structure without any further rotational and mirror domains than those already encountered for PTCDA. In fact, the SnPc BL serves as an ideal buffer layer for the highly ordered growth of multilayers. Even several nanometers thick films are highly ordered with a structure rather similar to that of the buffer layer. If the PTCDA layer is omitted, however, no long-range ordering was observed. PTCDA thus serves as a commensurate template layer for multilayer formation. This demonstrates the potential of organic-organic heterointerfaces to gain influence on multilayer formation.



# 5 Potassium Doping of PTCDA Monolayer Domains on Ag(111)

*Different experimental and theoretical techniques are employed in this chapter in order to characterize K-doped PTCDA monolayer domains on Ag(111). DRS, LEED, and ST[H]M data were acquired and analyzed together with Christian Zwick, who has used parts of the data for his master's thesis. PES measurements done in Jena were performed by Felix Otto. NIXSW measurements were performed at the beamline I09 of Diamond Light Source (England) in close collaboration with Prof. Dr. Christian Kumpf (Forschungszentrum Jülich), who headed the session, and Prof. Dr. Benjamin Stadtmüller (University of Kaiserslautern). During the measurement session, we were assisted by Dr. Sergey Subach, Markus Franke, Dr. Gerben van Straaten (all from Forschungszentrum Jülich), Ina Krieger (University of Bonn), and Norman Haag (University of Kaiserslautern). Density functional theory (DFT) calculations and STM simulations were done by Dr. Anu Baby, Elisabeth Verwüster, Dr. Oliver T. Hofmann (all from Graz University of Technology). They were assisted by Dr. Guido Fratesi (University of Milano-Bicocca and University of Milan), Prof. Dr. Gian Paolo Brivio (University of Milano-Bicocca), and Prof. Dr. Egbert Zojer (Graz University of Technology) for the interpretation of the results. Parts of the calculations and experimental data can be found in a joint publication [72]. The DFT calculations and STM simulations discussed in this chapter are indispensable for the understanding of the experimental data, however, these calculations were not carried out by myself.*

## 5.1 Introduction

Controlled doping is the key for tailoring of electronic and optical properties of layers in organic-based devices. Doping of inorganic semiconductors has been investigated exhaustively. The experiences and know-how gained in these studies, however, cannot be straightforwardly applied to organic material mainly because of the rather different electronic structure. Especially the tendency of band formation is much less pronounced in organic compounds resulting in more strongly localized charge carriers. Doping in this case can be thus understood more as charging of individual molecules rather than band doping. Consequently, not only the electronic structure, but also molecular packing motifs and morphologies may drastically change upon doping.

Alkali metal doping of organic thin films has been extensively studied for the prototypical molecule 3,4,9,10-perylene-tetracarboxylic-dianhydride (PTCDA), where electronic [80, 151–161], optical [161, 162], vibrational [153, 154, 157, 163], and structural properties [72, 80, 153, 155, 160] were characterized. These reports indicate that electrons are injected into the LUMO of PTCDA due to charge transfer complex formation. The determination of the specific doping ratios, however, seems quite challenging. These values are often estimated from stoichiometric ratios between molecules and dopants on the basis of core level PES [154–157, 159] or by using a quartz crystal microbalance [158]. The interpretation of such results requires a precise knowledge about the structures formed because not every alkali metal atom necessarily undergoes charge transfer with PTCDA. Some of them may form clusters, others are indeed incorporated into the film, but occasionally charge transfer may be hampered due to unfavorable adsorption sites. Gaining accurate structural information, however, is often hindered by polycrystallinity, tiny domains, or even the lack of any degree of structural ordering.

In this chapter, it shall be demonstrated that highly ordered layers of K-PTCDA charge transfer complexes can be epitaxially grown on Ag(111) allowing for a comprehensive and consistent study of their structural, electronic, and optical properties. The starting point of each experiment was a submonolayer (subML) of PTCDA on Ag(111) with a coverage of 0.6 to 0.7 ML. Potassium was subsequently deposited from a commercially available dispenser source (SAES Getters) while the substrate was kept at room temperature (RT). The structures formed were studied

using low-energy electron diffraction (LEED), scanning tunneling [hydrogen] microscopy (ST[H]M), and the normal incidence x-ray standing wave (NIXSW) technique. The electronic and optical properties were studied by means of photoelectron spectroscopy (PES) and differential reflectance spectroscopy (DRS), respectively.

## 5.2 Optical Properties

The impact of potassium doping on the optical properties of PTCDA shall be discussed first. For this purpose, DRS data (cf. Fig. A.5) were acquired during potassium deposition onto a 0.7 ML PTCDA/Ag(111) film. For a quantitative analysis of the DRS signal in terms of the light-absorbing behavior of the film, the imaginary part of the dielectric function  $\epsilon''$  shall be determined initially. One prerequisite for applying the numerical algorithm (cf. Subsec. 3.2.1) for the extraction of  $\epsilon''$  from DRS data is that the observed optical transition bands are entirely covered by the measured spectral range. In fact, this cannot be achieved for this system owing by the limitations of the spectral range accessible with our experimental setup. The  $\epsilon''$  spectra were therefore analytically extracted from the DRS data by using the approximation given by Eq. 3.3. This is justified because in the here considered spectral range the optical functions of silver are such that  $|B| \ll |A|$  is satisfactorily fulfilled, cf. Fig. 3.3. Further information about this approach and the prerequisites for its applicability are given in Subsec. 3.2.1.

The  $\epsilon''$  spectrum of the pristine 0.7 ML PTCDA/Ag(111) film shown in Fig. 5.1 (a) (black line) reveals a broad and featureless optical absorption. This behavior is indicative of a strong bonding situation [51], which is often referred to as chemisorption in the literature. The bonding of PTCDA on Ag(111) has been the subject of various literature reports. [29, 51, 78, 154, 164–169] For instance, it has been concluded from photoemission spectroscopy that the electronic structure of a ML of PTCDA in contact with Ag(111) differs significantly compared to that of PTCDA multilayers. This can be mainly attributed to a strong orbital overlap of the flat-lying PTCDA molecules with orbitals of Ag(111). [78, 164, 169] The optical absorption thus stems from transitions between states that are strongly affected by metal-organic hybridization (cf. Newns-Anderson model [170, 171]).

With the beginning of potassium deposition, the situation clearly changes (cf. red lines in Fig. 5.1 (a)). The broad absorption of the hybridized PTCDA par-

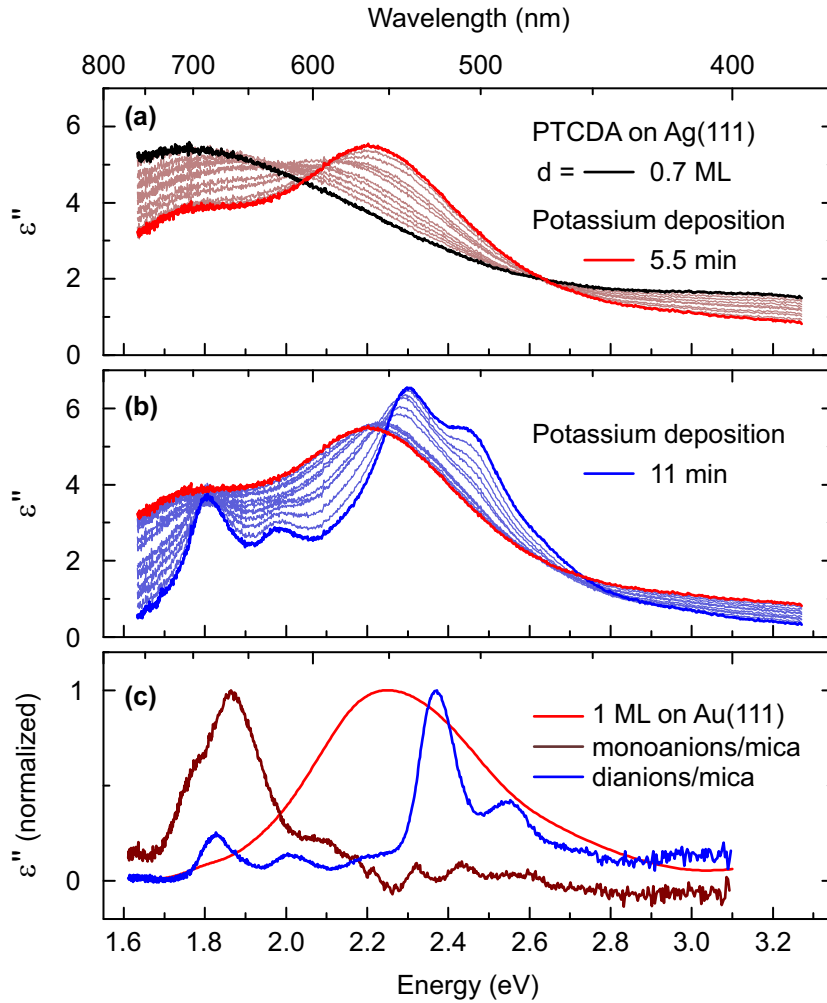


**Figure 5.1:**  $\epsilon''$  spectra of K-doped 0.7 ML PTCDA/Ag(111) extracted from the DRS data in Fig. A.5. Doping stages are indicated by characteristic optical absorption features observed for pristine PTCDA and for continuous potassium deposition of (a) up to 5.5 min, and further (b) up to 11 min. (c)  $\epsilon''$  spectra of 1 ML PTCDA/Au(111) [173] and PTCDA mono- and dianions on mica [162] are shown for comparison. Slight spectral shifts can be ascribed to different polarizabilities of the substrate and/or two-dimensional aggregation effects [174]. Since the DRS raw data are affected by spectral drift for photon energies below 1.63 eV, the  $\epsilon''$  spectra were cut at the low-energy side in order to prevent misinterpretations. Even slight drift can influence the  $\epsilon''$  values considerably if Eq. 3.3 is employed, because  $A(E)$  of Ag becomes very small at low  $E$ , cf. Fig. 3.3.

tially disappears in favor of a distinct feature at 2.29 eV. This emerges up to a potassium deposition time of 5.5 min, which indicates the end of the first doping stage (cf. thick red line in Fig. 5.1 (a)). The optical signature shall be discussed under the aspects of broadening and the energetic peak positions. From the fact that the spectra are less broadened compared to those of the pristine PTCDA film, it can be concluded that the metal-organic hybridization is reduced. However, the molecules are not entirely electronically decoupled as it is frequently the case on inert and passivated substrates, where vibrationally resolved molecular features can be observed. [47, 51, 136, 162, 172, 173] Remarkably, a rather similar fingerprint is provided by 1 ML PTCDA/Au(111) [173], a system commonly described as electronically weakly interacting (physisorption) because no significant charge transfer across the metal-organic interface was found.[168] Although the spectra of the first doping stage and PTCDA/Au(111) are rather comparable in terms of broadening as well as the peak position, the origin of the peak can be indeed different. Scenarios are plausible were the molecules in the first doping stage are either neutral or doubly negatively charged (dianions) (cf. blue line in Fig. 5.1 (c)). The occurrence of singly negatively charged PTCDA (monoanions) can be ruled out since the corresponding features are clearly absent (cf. dark red line in Fig. 5.1 (c)). The charging state of PTCDA can only be elucidated with the help of complementary methods as shown later in this chapter.

Up to a potassium deposition time of 11 min, distinct peaks evolve in the  $\epsilon''$  spectra thereby giving rise to the second doping stage. Strikingly, the spectral features are less broadened than for the first stage, which means that the molecules are even better electronically decoupled from the substrate. The main spectral features are at 2.31 and 2.47 eV, followed by a shoulder on the high-energy side. Smaller features are observed at 1.81 and 2.00 eV. The spectral appearance is characteristic for PTCDA dianions, which follows from a comparison with the reference spectrum in Fig. 5.1 (c). The overall agreement is quite good, only the peak-height ratio of the main features and spectral broadening slightly differ compared to the reference spectrum. These effects can be ascribed to a stronger electronic interaction of PTCDA with substrate states than it is the case on mica and, additionally, to the beginning formation of the next higher doping stage (cf. Fig. 5.2 (a)).

Further doping stages can be observed for continuing potassium deposition. After completion of the second doping stage, dianions features disappear in favor of a peak

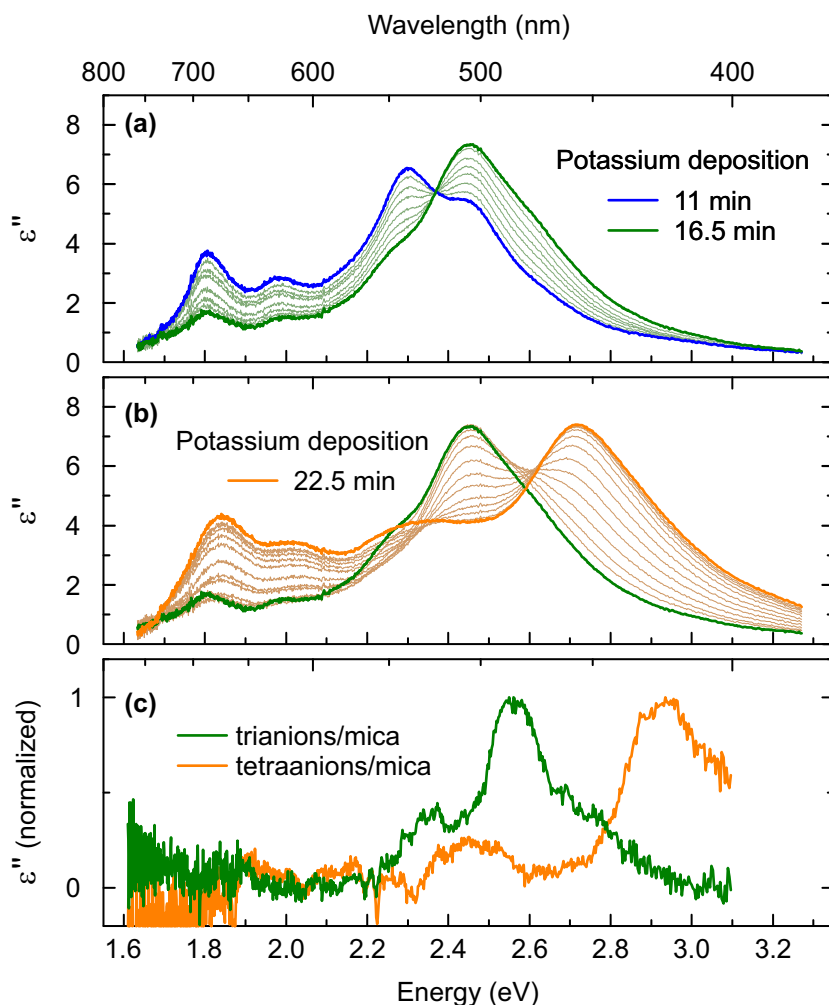


**Figure 5.2:**  $\epsilon''$  spectra of K-doped 0.7 ML PTCDA/Ag(111) for higher potassium concentrations. Doping stages are indicated by characteristic optical absorption features. The PTCDA dianion behavior is observed for 11 min potassium deposition in (a). Higher charging states are observed for (a) 16.5 and (b) 22.5 min, where the spectra are indicative of the formation of tri- and tetraanions. (c)  $\epsilon''$  spectra of PTCDA tri- and tetraanions on mica [162] are shown for comparison. Slight spectral shifts can be ascribed to different polarizabilities of the substrate and/or two-dimensional aggregation effects [174]. Since the DRS raw data are affected by spectral drift for photon energies below 1.63 eV, the  $\epsilon''$  spectra were cut at the low-energy side in order to prevent misinterpretations. Even slight drift can influence the  $\epsilon''$  values considerably if Eq. 3.3 is employed, because  $A(E)$  of Ag becomes very small at low  $E$ , cf. Fig. 3.3.



emerging at 2.47 eV and a shoulder at 2.63 eV for a potassium deposition time of up to 16.5 min (cf. thick green line in Fig. 5.2 (a)). For even higher potassium concentrations, a feature and a shoulder occur at around 2.75 and 2.47 eV, respectively. Additionally, a series of peaks is visible for photon energies around 1.85 eV. The spectra corresponding to 16.5 and 22 min deposition time have distinct similarities to the spectra of triply and quadruply negatively charged PTCDA, respectively, as shown in Fig. 5.2 (c). DRS indicates that these stages are metastable since they degenerate on the time scale of minutes after stopping the potassium deposition (not shown).

So far, it has been shown that electronic interaction across the metal-organic interface as well as the charging states of the molecules are functions of the amount of potassium deposited. Distinct doping stages are clearly discernible, where each has a characteristic fingerprint in the optical absorption. Further structural and electronic investigations within this chapter refer to this definition of doping stages. Since the optical spectra of the first doping stage cannot unequivocally be interpreted in terms of the charging state of PTCDA, additional information shall be gained from photoelectron spectroscopy.

## 5.3 Electronic Properties

### 5.3.1 Valence Band Spectra and Work Functions

Valence band (VB) spectra of K-doped 0.7 ML PTCDA/Ag(111) are shown in Fig. 5.3. Potassium was deposited until accomplishing the first and second doping stages referring to the DRS measurement in Fig. 5.1. The VB spectra of the pristine PTCDA subML are additionally given in the graph.

For the pristine PTCDA subML, a peak at the binding energy of  $E_B = 1.55$  eV and a feature cut by the *Fermi* level show up. These features can be assigned to the HOMO and the former LUMO (F-LUMO) of PTCDA, respectively. The F-LUMO is partially filled due to a charge transfer across the metal-organic interface. [164, 175, 176] It has been shown that such a signature is indicative of a rather strong bonding situation (chemisorption). [104, 125, 164, 168]

In the first doping stage, the HOMO and F-LUMO peaks of PTCDA are both shifted to lower binding energies of 0.69 and 1.96 eV, respectively, giving rise to

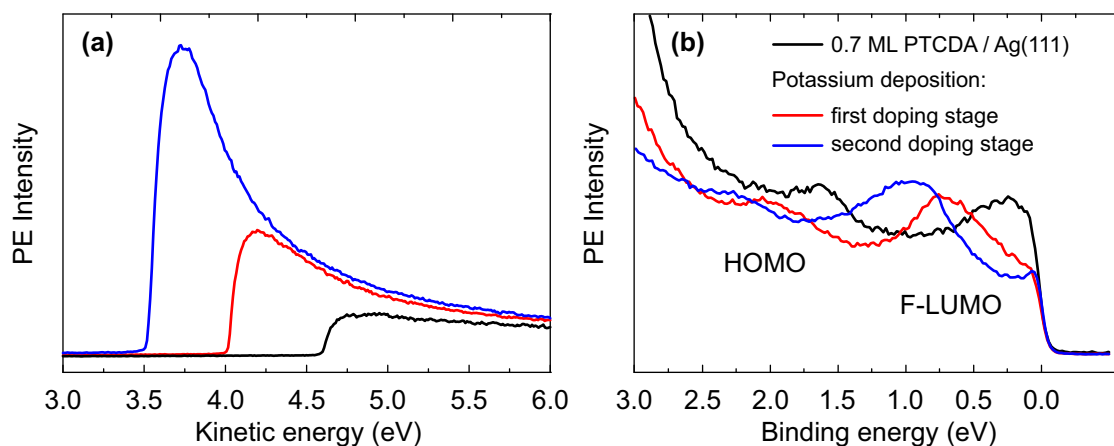


**Figure 5.3:** VB spectra of K-doped 0.7ML PTCDA/Ag(111) for the first (red lines) and second (blue lines) doping stage. All spectra were acquired in normal emission geometry using He-I $\alpha$  ( $h\nu = 21.22$  eV) excitation. The VB spectrum of the pristine PTCDA/Ag(111) film is given for comparison (black lines). The secondary electron cut-off spectra are shown in (a); the region around the Fermi level is shown in (b). The peaks observed in (b) are assigned to HOMO and F-LUMO of PTCDA.

a complete filling of the F-LUMO. The energetic separation between HOMO and F-LUMO is 1.27 eV, i.e., almost unchanged as compared to the pristine PTCDA on Ag(111). [168] Remarkably, the shift of the VB features towards higher binding energies is in accordance with the work function decrease of 0.6 eV.

In the second doping stage, the HOMO and F-LUMO peaks further shift to binding energies of 0.93 and 2.26 eV, respectively. The energetic difference between the HOMO and F-LUMO position is slightly larger than in the first doping stage. The VB features are shifted to higher binding energies, however, no additional orbitals become filled. The work function decrease of 0.5 eV relative to the first doping stage is larger than the shift of the HOMO and F-LUMO peaks, which can be plausibly explained by the noticeable amount of excess potassium as revealed by means of core level PES in the next subsection.

A fully occupied LUMO of PTCDA in the first and the second doping stages indicates PTCDA dianion formation in both cases. This is interesting since the amount of potassium deposited for the second doping stage is significantly higher than for the first doping stage. It is thus worthwhile to analyze the chemical composition of these two doping stages by means of core level photoelectron spectroscopy.

### 5.3.2 Core Level Spectra

#### Peak-fit Analysis

Core level spectra were recorded from all chemical species that are present in the films of pristine 0.7 ML PTCDA/Ag(111) as well as of the first and second doping stages. The peak fitting models, which enable for a quantitative analysis of these spectra, shall be discussed in the following.

The C 1s PE spectrum of the pristine PTCDA film is shown in Fig. 5.4 (a). By using high-resolution core level PE spectra of PTCDA multilayer films (with more than 10 ML) on Ag(111) [177], the presence of four chemically different carbon species were identified, which are closely related to the molecular structure of PTCDA: the carbon atoms of the functional groups that bond to carbon and oxygen atoms (C1, also referred to as  $C_{\text{funct}}$ ), the connecting carbon atoms between the functional groups and the carbon atoms of the perylene core (C2), the carbon atoms that are bonded to three other carbon atoms (C3), and the carbon atoms with one bond to a hydrogen atom and two bonds to carbon atoms (C4). For stoichiometric reasons, the PE yields  $Y$  of these components follow the ratios:

$$Y(\text{C1}) : Y(\text{C2}) : Y(\text{C3}) : Y(\text{C4}) = 4 : 4 : 8 : 8 \quad . \quad (5.1)$$

The binding energies of the main peaks  $\text{C2}^{\text{m}}$ ,  $\text{C3}^{\text{m}}$ , and  $\text{C4}^{\text{m}}$  do not differ much thereby forming the asymmetric shape of the main emission line of the perylene core ( $\text{C}_{\text{peryl}} = \text{C2}^{\text{m}} + \text{C3}^{\text{m}} + \text{C4}^{\text{m}}$ ) in Fig. 5.4 (a). In contrast, the main peak of the functional carbon atoms  $\text{C1}^{\text{m}}$  appears at a significantly higher binding energy and is therefore well separated from the perylene core main emission line. This can be explained by the presence of the highly electronegative oxygen atoms, which withdraw electrons from the perylene core via the functional carbon atoms thereby giving rise to a relatively large chemical shift to  $\text{C1}^{\text{m}}$ , whereas the  $\text{C}_{\text{peryl}}$  underlying peaks are less affected. The chemical shift of  $\text{C1}^{\text{m}}$ , however, is noticeably smaller than that observed in PTCDA multilayers. [177] This can be readily explained by the strong electronic interaction of the oxygen atoms of PTCDA with the Ag(111) surface as well as the different intermolecular interaction in the subML, both together are responsible for a different chemical environment for the functional carbon atoms. Besides the main peaks, also satellites were taken into account, namely  $\text{C1}^{\text{s}}$ ,  $\text{C5}^{\text{s}}$ ,

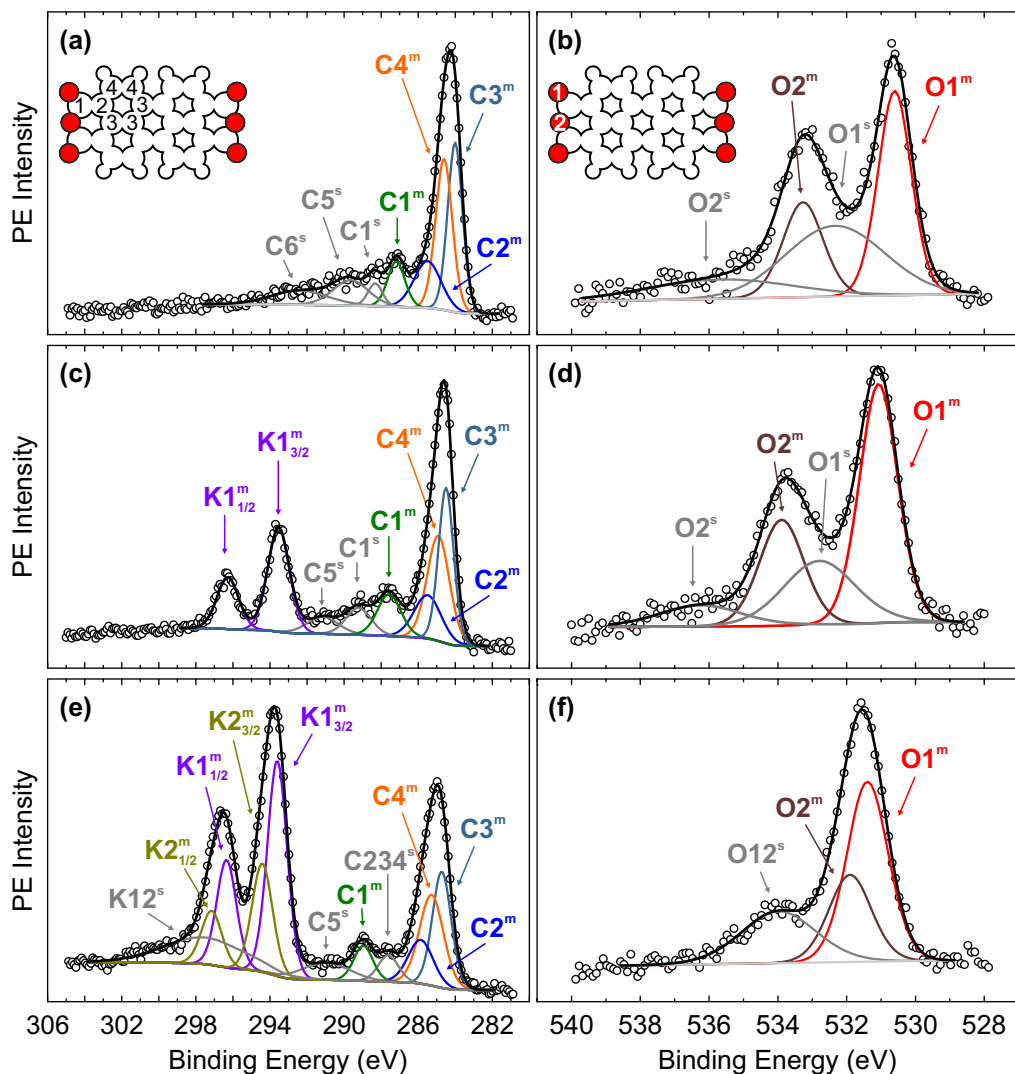


**Figure 5.4:** Core level spectra of the pristine PTCDA layer [(a) C 1s; (b) O 1s], the first doping stage [(c) C 1s and K 2p; (d) O 1s], and the second doping stage [(e) C 1s and K 2p; (f) O 1s]. All spectra were acquired at  $70^\circ$  emission using an excitation energy of 1486.6 eV ( $Al K_\alpha$ ). C 1s and K 2p spectra were measured using a pass energy of 20 eV, O 1s spectra with 100 eV. Measured data points are given as circles. The PE backgrounds of C 1s and K 2p were described by the Shirley function, whereas a linear background was used for O 1s. The peaks of each individual component distinguished by the fitting model are shown as solid lines. The thick black lines represent the best fits to the data.

**Table 5.1:** Peak parameters of the fitted components in Fig. 5.4. Binding energy:  $E_B$ ; FWHM: peak width; and relative areas.

peak	undoped PTCDA			first doping stage			second doping stage			origin
	$E_B$ (eV)	area (%)	FWHM (eV)	$E_B$ (eV)	area (%)	FWHM (eV)	$E_B$ (eV)	area (%)	FWHM (eV)	
C2 <sup>m</sup>	285.49	13.8	1.71	285.49	14.5	1.72	285.87	14.6	1.20	C <sub>peryl</sub>
C3 <sup>m</sup>	284.00	27.6	0.95	284.50	29.1	0.96	284.73	29.3	1.53	
C4 <sup>m</sup>	284.60	27.6	1.06	284.91	29.1	1.42	285.28	29.3	1.59	
C234 <sup>s</sup>							287.61	7.2	1.29	
C1 <sup>m</sup>	287.18	8.6	1.10	287.56	12.3	1.49	288.96	9.0	1.22	C <sub>funct</sub>
C1 <sup>s</sup>	288.32	3.6	0.93	289.21	8.4	1.60				
C5 <sup>s</sup>	289.64	9.9	2.26	291.16	6.6	1.99	290.98	10.7	1.29	C satellites
C6 <sup>s</sup>	292.41	8.7	3.58							
O1 <sup>m</sup>	530.61	33.7	1.14	531.06	42.4	1.28	531.39	49.5	1.41	O <sub>carbox</sub>
O1 <sup>s</sup>	532.34	33.8	3.38	532.39	21.1	2.44				
O2 <sup>m</sup>	533.27	18.8	1.37	533.85	26.6	1.55	531.90	24.8	1.46	O <sub>anhyd</sub>
O2 <sup>s</sup>	535.70	13.7	5.02	536.06	9.9	3.11				
O12 <sup>s</sup>							533.98	25.7	2.55	O satellite
K1 <sub>3/2</sub> <sup>m</sup>				293.53	66.7	1.37	293.61	35.6	1.25	K <sub>PTCDA</sub>
K1 <sub>1/2</sub> <sup>m</sup>				296.27	33.3	1.37	296.35	17.8	1.25	
K2 <sub>3/2</sub> <sup>m</sup>							294.42	18.7	1.31	K <sub>excess</sub>
K2 <sub>1/2</sub> <sup>m</sup>							297.16	9.4	1.31	
K12 <sup>s</sup>							297.49	18.5	5.33	K satellite

and C6<sup>s</sup>. While the first originates from C1<sup>m</sup>, the latter two most likely have contributions from C<sub>peryl</sub> and C1<sup>m</sup>. The satellite C234<sup>s</sup> accompanying the main peaks C2<sup>m</sup>, C3<sup>m</sup>, and C4<sup>m</sup> is known to occur, however, this cannot be evidenced here, because it coincides with C1<sup>m</sup> and appears usually with relatively low PE intensity. [80, 177] The peak areas of C2<sup>m</sup>, C3<sup>m</sup>, and C4<sup>m</sup> were constrained in the fitting model according to Eq. 5.1. Remarkably, the PE yields of each chemical component (main peak + satellite) distinguished by the fitting model reflect the stoichiometry of PTCDA quite well. The O 1s spectrum is shown in Fig. 5.4 (b). This consists of two chemically inequivalent oxygen species, O1 and O2, originating from the carboxylic and anhydride oxygen atoms, respectively. The corresponding main peaks O1<sup>m</sup> and O2<sup>m</sup> are each accompanied by a shake-up satellite, i.e., a four-peak model is applied. The stoichiometric ratio of 1:2 between the carboxylic and anhydride oxygen atoms is correctly reflected if not only the main peaks, but also their satellites are considered in the balance of the PE yields, which is  $[Y(O2^m) + Y(O2^s)]:[Y(O1^m) + Y(O1^s)] = 0.48$ . The *FWHMs* and positions of the peaks were not constrained for fitting the O 1s spectrum.

The C 1s fitting model of the pristine PTCDA film has been transferred to the respective PE spectrum of the first doping stage shown in Fig. 5.4 (c). In addition to the C 1s signature, K 2p emission lines of the deposited potassium additionally show up in the high-binding energy region. The main differences in the C 1s signal compared to the undoped film are the satellite features C1<sup>s</sup> appearing with higher intensity, C5<sup>s</sup> is weaker, and C6<sup>s</sup> is not readily visible because of the intense potassium features. Further, all peaks slightly shift towards higher binding energies (e.g., C4<sup>m</sup> shifts by 0.49 eV). The potassium signature comprises two spin-orbit split peaks (K1<sub>3/2</sub><sup>m</sup> and K1<sub>1/2</sub><sup>m</sup>), which are energetically separated by 2.74 eV. [178] The ratio of their areas has been constrained to 1:2 for the fit of the spectrum, which follows from the degeneracy of the respective initial states. As both peaks originate from the same species, the degree of broadening is expected to be identical. The O 1s signature in Fig. 5.4 (d) is also rather comparable to that of the undoped film (cf. Fig. 5.4 (b)). Basically, O1<sup>m</sup> and O2<sup>m</sup> slightly shift towards higher binding energies by 0.45 and 0.58 eV, respectively. These values nicely agree with the C 1s chemical shift in the first doping stage with respect to the undoped PTCDA film. Further, the O 1s satellites are less pronounced, i.e., more PE intensity is transferred into the respective main peaks O1<sup>m</sup> and O2<sup>m</sup> compared to the pristine PTCDA film.

For the second doping stage, it can be seen that the main carbon peaks  $C2^m$ ,  $C3^m$ , and  $C4^m$  slightly shift towards higher binding energies (e.g.,  $C4^m$  shifts by 0.37 eV) with respect to the first doping stage. The most noticeable difference, however, is observed for  $C1^m$ , which shifts by 1.40 eV to a value which is similar to that observed for PTCDA multilayer films on Ag(111) [177]. The peak labeled with  $C234^s$  mainly stems from satellites of  $C2^m$ ,  $C3^m$ , and  $C4^m$ . Significant differences between the first and second doping stages can also be observed for the K  $2p$  signature. Not only the signal intensity increases, but asymmetric emission lines appear at 293.6 and 296.4 eV. These are indicative of two K  $2p$  doublets [179], shifted in binding energy by 0.77 eV. The energetic separation of the two spin-orbit split peaks of each doublet was constrained for the fit to 2.74 eV. These findings indicate two inequivalent potassium species, namely potassium incorporated into the PTCDA film ( $K1_{3/2}^m$  and  $K1_{1/2}^m$ ) and excess potassium ( $K2_{1/2}^m$  and  $K2_{3/2}^m$ ). The higher binding energy of the excess potassium indicates stronger oxidization, which suggests that this species directly adsorbed on the Ag(111) surface. This is further corroborated by the almost identical K  $2p$  doublet revealed for potassium deposited onto a clean Ag(111) substrate (cf. Fig. A.7). Also the O  $1s$  signature is strongly affected by the higher potassium concentration as shown in Fig. 5.4 (f).  $O2^m$  appears shifted by approximately  $-1.8$  eV compared to the first doping stage, whereas the carboxylic oxygen peak  $O1^m$  is affected to a minor extent only. It can be stated that the chemical environment of the anhydride oxygen atoms must be entirely different between the first and second doping stages. In fact, this can be realized by the structure model that will be developed in Sec. 5.4.1, which reveals that one and two potassium atoms are nearby each anhydride oxygen atom in the first and second doping stages (cf. Fig. 5.5). The shoulder at 534.1 eV in Fig. 5.4 (d) is accounted for by a single satellite peak  $O12^s$  possibly having contributions from both main peaks  $O1^m$  and  $O2^m$ . The very small intensity of the satellite means a strongly reduced inelastic scattering of O  $1s$  photoelectrons in the film. This might be explained by a lower bonding strength of the oxygen atoms to Ag(111), i.e., a reduced metal-organic hybridization of PTCDA in the second doping stage as already indicated by the DRS results in Sec. 5.2.

The azimuthal angle dependence of the PE intensities of the C  $1s$ , K  $2p$ , and O  $1s$  signatures were measured for the first and second doping stages. From this information, the morphology can be inferred to a certain extent: [180] Since no

significant differences between  $70^\circ$  (cf. Fig. 5.4) and  $0^\circ$  (cf. Fig. A.8) are observed, it is likely that potassium ( $K1_{3/2}^m$  and  $K1_{1/2}^m$ ) is situated in between rather than underneath the molecules.

### Estimation of Stoichiometry

The stoichiometric ratio  $x$  between potassium and PTCDA can be estimated from the ratio of PE yields of potassium and carbon emission lines. PE yields do not only depend on atomic concentrations, but also on photoionization cross sections, the mean electron escape depth, the analyzer transmission, and photoelectron attenuation lengths of the layer. [180] All these parameters depend on the kinetic energy of the photoelectrons. However, these complex dependencies are canceled in the ratio of PE yields here since the photoelectrons emitted from C 1s and K 2p core levels have rather similar kinetic energies. The ratio of atomic concentrations between potassium  $c(K\ 2p)$  and carbon  $c(C\ 1s)$  can thus be approximated by:

$$\frac{c(K\ 2p)}{c(C\ 1s)} = \frac{Y(K\ 2p)}{Y(C\ 1s)} \cdot \frac{\sigma(C\ 1s)}{\sigma(K\ 2p)}, \quad (5.2)$$

with the PE yield  $Y$  and the photoionization cross section  $\sigma$  of the respective species. PE yields are given by the peak areas, which are an outcome of the peak-fit analysis in Fig. 5.4 (c) and (e). Accordingly,  $Y(C\ 1s)$  and  $Y(K\ 2p)$  refer to the total areas of all C 1s peaks and the area of the doublet that stems from potassium bonded to PTCDA ( $K1_{3/2}^m$  and  $K1_{1/2}^m$ ), respectively. The amount of excess potassium can be estimated by instead using the other doublet ( $K2_{3/2}^m$  and  $K2_{1/2}^m$ ). The photoionization cross sections, which are listed in Tab. 5.2, were calculated using the formula given in Ref. [181]. The stoichiometric ratio  $x$  can easily be derived from Eq. 5.2

**Table 5.2:** Calculated ratio of the photoionization cross sections of carbon C1s and potassium K2p according to Ref. [181] for the two photon energies used for the measurements in Fig. 5.4 and Fig. 5.7.

photon energy (eV)	$\sigma(C\ 1s):\sigma(K\ 2p)$ [neutral K]	$\sigma(C\ 1s):\sigma(K\ 2p)$ [K <sup>+</sup> ]
1486	0.249	0.252
2632	0.281	0.279



multiplied by the overall number of carbon atoms of a PTCDA molecule, i.e., 24. Since the photoionization cross sections for neutral potassium (K) and singly ionized potassium ( $K^+$ ) are almost identical (within 1%) for the here considered photon energies, information about the respective charging state of potassium is not necessarily required for the estimation of stoichiometries.

The stoichiometries were estimated to 2.5 and 4.6 potassium atoms bound to PTCDA for the first and second doping stage, respectively. There is little excess potassium in the first doping stage, however, in the second doping stage excess potassium occurs significantly with 3.1 potassium atoms per PTCDA molecule. If the two different potassium species had not been distinguished in the PE spectra by means of peak fitting, the overall signal intensity of K  $2p$  could easily have been misinterpreted in terms of the stoichiometry of charge transfer complexes formed. The results indicate  $K_2$ PTCDA in the first doping stage, however, in the second doping stage, it is not clear whether  $K_4$ PTCDA or  $K_5$ PTCDA complexes are formed. Detailed structural characterization of the charge transfer complexes shall therefore be performed in the following.

## 5.4 Structural Characterization

### 5.4.1 Lateral Structures

#### First Doping Stage: $K_2$ PTCDA

The starting point of the structural investigation was a 0.7 ML PTCDA/Ag(111) film showing the well-known commensurate herringbone structure [22, 29, 167, 176] with two molecules in the unit cell (cf. Fig. 5.5 (a)). Potassium was deposited until accomplishing the first doping stage referring to the DRS measurement in Fig. 5.1. The structure of the pristine PTCDA/Ag(111) is thereby converted into another highly ordered phase as indicated by the LEED images in Fig. 5.5 (a) and (b). The structural parameters of the first doping stage were accurately determined through lattice fits to the LEED image in Fig. 5.5 (b) using the LEEDLab software [66]. All spots can be well described by considering a unit cell with the vectors  $\mathbf{a}_1$  and  $\mathbf{a}_2$  being 8.92 and 16.05 Å in length, respectively, and a unit cell angle  $\Gamma$  of 108.60°. The corresponding epitaxy matrix reveals a point-on-line (POL) coincidence (cf.

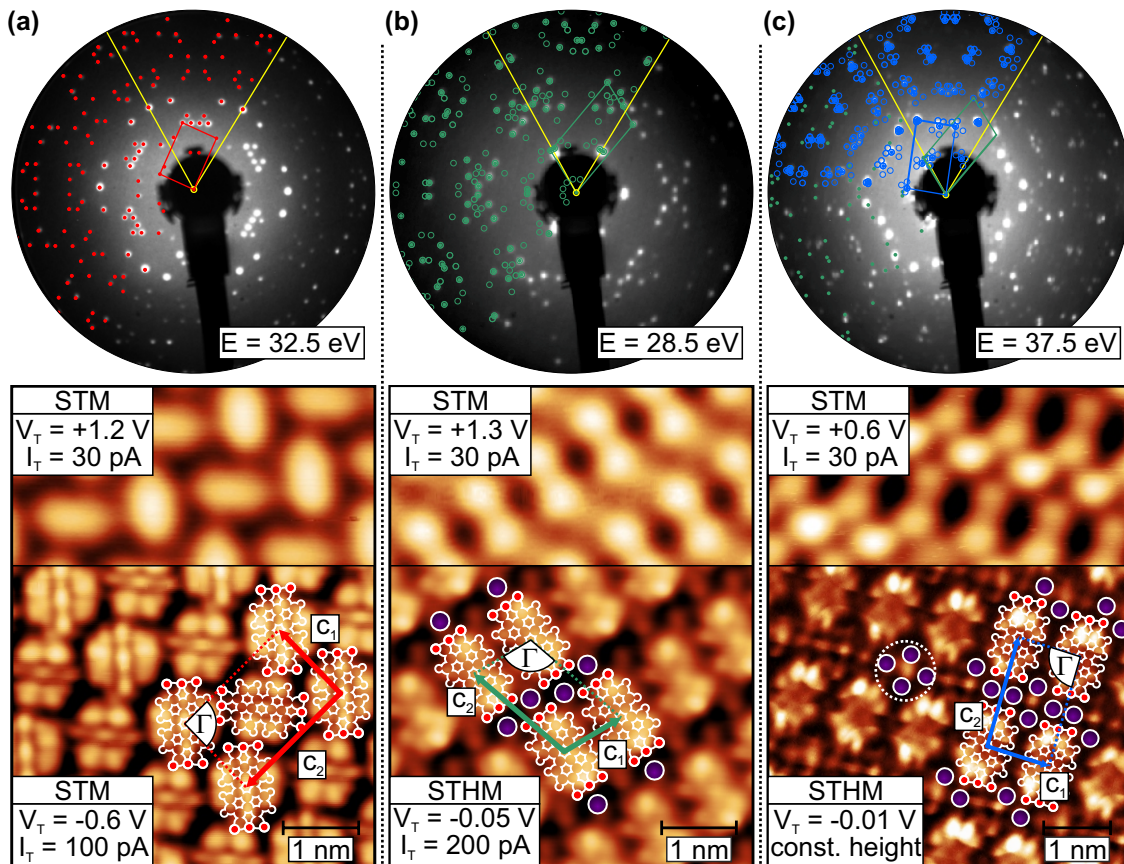


**Figure 5.5:** LEED and STM data of 0.7 ML PTCDA/Ag(111). Starting from the pristine PTCDA layer in (a), potassium doping results in distinct  $K_x$ PTCDA complexes with  $x$  being 2 and 4 in (b) and (c), respectively. The LEED patterns (primary electron energy  $E$  is indicated in each panel) are fully describable by the epitaxial matrices given in Tab. 5.3 and symmetry equivalents. The corresponding LEED simulations (filled dots) and reciprocal unit cells are superimposed to segments of the images. No spots remain unidentified by taking multiple scattering effects (open circles) into account. Additionally, primitive reciprocal unit cells of Ag(111) are indicated by the yellow lines. STM and STHM images were stitched together to illustrate the different contrasts achievable by different tunneling conditions (tunneling bias  $V_T$  and current  $I_T$ ). The suggested structure models (molecular silhouette of PTCDA in white and potassium atoms in purple) are superimposed to the ST[H]M images.

Sec. 3.1) with respect to the substrate lattice. This is corroborated by the one-dimensional *Moiré* pattern visible in the large scale STM image in Fig. A.6 (a). The domains are rather large and exhibit a low defect density.

When trying to analyze the unit cell composition, only somewhat blurred features can be found in STM images (cf. Fig. 5.5 (b)), which is not an unusual behavior for molecules in contact with a metal surface. [182–184] These STM images are therefore inappropriate for determining potassium adsorption sites. However, knowledge about these is indispensable for a comprehensive understanding of the DRS and the PES data. To tackle this issue, the STHM technique has been adapted (cf. Subsec. 3.3.2), which goes well beyond conventional STM since the lateral resolution can be strongly enhanced yielding a contrast which is reminiscent of the skeletal formula of the molecules. [69, 70] This is achieved by condensing elementary hydrogen within the tunneling junction. The tunneling characteristics are thereby altered when the tip is operated at distances where *Pauli* repulsive forces dominate. In turn, by setting more moderate tunneling parameters, one can switch back to a contrast of conventional STM. This has been done for two separate measurements shown in Fig. 5.5 (b). While the upper part clearly shows the contrast of conventional STM, the lower part allows for resolving individual molecules as well as potassium atoms owing to the strongly increased resolution provided by STHM. It can be seen that the unit cell consists of one molecule and two potassium atoms which are situated at opposite ends of PTCDA. This structure corroborates the known tendency of alkali metal atoms to bond to the functional groups of PTCDA. [160, 163] Remarkably, the here observed structural appearance as well as bonding distances are both rather similar to those calculated for free-standing  $K_2$ PTCDA complexes. [163] Strikingly, the potassium is incorporated into the film, i.e., a mixed monolayer phase together with the PTCDA molecules. The situation is clearly different from a similar doping experiment where Ag(110) instead of Ag(111) was used as substrate. [185] The films there were also prepared by potassium deposition onto a predeposited PTCDA film, however, highly ordered structures were only obtained by post-growth annealing. The potassium was then observed to be incorporated into the less densely packed upper substrate layer giving rise to a missing-row surface reconstruction. Since the films investigated here were neither annealed nor do they show any indication of a Ag(111) surface reconstruction, it is rather unlikely that further potassium is situated underneath the PTCDA molecules.

The found unit cell parameters and composition of the  $K_2$ PTCDA phase were used as a starting point for structural optimizations by means of density functional theory (DFT) calculations. [72] The optimized geometry closely resembles the ex-

**Table 5.3:** Structural parameters of  $K_x\text{PTCDA}$  complexes on  $\text{Ag}(111)$  for  $x = 0, 2, 4$ .  $\mathbf{a}_1$ ,  $\mathbf{a}_2$ : lattice vectors;  $\Gamma$ : unit cell angle between  $\mathbf{a}_1$  and  $\mathbf{a}_2$ ;  $\theta$ : domain angle between  $\mathbf{a}_1$  and a primitive substrate lattice vector, and  $A_{\text{PTCDA}}$ : area of the unit cell divided by the number of molecules in the unit cell. Uncertainties given in parentheses represent the standard deviation of the numerical lattice fits. The  $\text{Ag}(111)$  primitive lattice vectors enclose an angle of  $120^\circ$ .

x	$ \mathbf{a}_1 $ (Å)	$ \mathbf{a}_2 $ (Å)	$\Gamma$ (°)	$\theta$ (°)	epitaxy matrix $\mathcal{C}$	$A_{\text{PTCDA}}$ (nm <sup>2</sup> )
0	12.59(1)	18.95(2)	90.99(5)	36.60(4)	$\begin{pmatrix} 5.00(1) & 3.00(1) \\ -1.00(1) & -6.00(1) \end{pmatrix}$	119.3(2)
2	8.92(1)	16.05(2)	108.60(9)	2.63(8)	$\begin{pmatrix} 3.16(1) & 0.16(1) \\ 0.98(1) & 5.98(1) \end{pmatrix}$	135.7(4)
4	9.57(1)	16.77(2)	91.66(1)	51.68(6)	$\begin{pmatrix} 3.55(1) & 3.00(1) \\ -2.65(1) & -4.00(1) \end{pmatrix}$	160.4(4)

perimentally found situation, which confirms that the assignment of features in the STHM image is correct. The DFT calculations additionally provide insight into the energetic balance of layer formation. It was found that the binding energy per molecule for the  $\text{K}_2\text{PTCDA}$  phase (11.61 eV) is significantly larger than for the former PTCDA herringbone structure (4.01 eV per molecule) and also for single K atoms (2.49 eV) on the silver surface. It was concluded that the formation of  $\text{K}_2\text{PTCDA}$  is energetically favored with an energy gain of 2.62 eV per molecule upon potassium doping. This indicates a rather strong bonding situation between PTCDA and potassium. This is most likely responsible for the here observed structural transition from the pristine PTCDA layer to the  $\text{K}_2\text{PTCDA}$  phase, which occurs fully self-organized and spontaneously affects whole domains even without annealing.

### Second Doping Stage: $\text{K}_4\text{PTCDA}$

By further potassium deposition until accomplishing the second doping stage referring to the DRS measurement in Fig. 5.1, a phase transition to another highly ordered structure evidenced by LEED, which occurs on the time scale of several minutes via an intermediate disordered phase. The analysis of the LEED image in Fig. 5.5 (c) reveals that, in comparison to the  $\text{K}_2\text{PTCDA}$  phase, the unit cell vectors  $\mathbf{a}_1$  and  $\mathbf{a}_2$  further increase in length to 9.57 and 16.77 Å, respectively, and the unit cell angle decreases to  $91.66^\circ$ . The epitaxy matrix indicates a POL coincidence (cf. Sec. 3.1) with respect to the substrate lattice. The structural parameters are

compiled in Tab. 5.3. Remarkably, the structural ordering does not reach the same quality as in the first doping stage, which is indicated by a lower contrast of the LEED spots as well as a noticeable number of clusters (cf. Fig. A.6 (b)). In the STM image shown in Fig. 5.5 (c), the molecules are again characterized by intense features nearby their functional groups as similarly observed for the  $K_2$ PTCDA phase. Additionally, bright features can be observed in between the molecules. All features in the STM image again appear somewhat blurred making definitive statements about the stoichiometry impossible; the advantages of STHM shall thus be used to tackle this issue. An STHM image of the second doping stage is shown in the lower part of Fig. 5.5 (c). This image does not only feature PTCDA with submolecular resolution, it also contains sharp features showing up in between the molecules. Identifying the stoichiometry is not as trivial as it may appear. If each of the sharp features within the unit cell were assigned to a potassium atom,  $K_5$ PTCDA complexes would have to be concluded. This suggested structure has been checked by means of DFT calculations where hypothetical  $K_x$ PTCDA complexes on Ag(111) with  $x=3, 4$  and  $5$  were structurally optimized using the here found unit cell parameters as a starting point. [72] The calculations reveal that for  $K_3$ PTCDA and  $K_5$ PTCDA either some of the potassium moves underneath the molecules giving rise to tilted molecules on the surface or the symmetry clearly disagrees with the observations made by STHM. Only  $K_4$ PTCDA complexes, whose structure model is superimposed to the STHM image in Fig. 5.5 (c), closely resemble the experimentally found situation: Four of the sharp features within the unit cell nicely agree with adsorption sites of the potassium atoms. However, the fifth feature in the center of the unit cell is where actually no potassium is situated according to the DFT calculations. This feature is even more pronounced in the corresponding STM image (cf. Fig. 5.5 (c)). In order to address this issue, STM images were simulated on the basis of the *Tersoff-Hamann* approach [186] in Ref. [72]. Since the simulated STM image of  $K_4$ PTCDA complexes yields perfect agreement with the experimentally obtained STM image, a deeper insight into the origin of the bright feature in between the PTCDA molecules can be gained. This feature was identified to stem from the LUMO of  $K_4^{4+}$  clusters (cf. white dashed circle in the STHM image Fig. 5.5 (c)), which are formed by four potassium atoms accompanied by a charge transfer of one electron per potassium atom to PTCDA and Ag(111). Strikingly, the LUMO of such a cluster has its highest density of states right in middle of the four potassium atoms and is energetically

broadened due to interface hybridization with Ag(111) making this feature visible over a wide bias range in STM. The existence of this feature in STHM can be ascribed to the imaging parameters used: the contrast achieved in this STHM image is, in fact, not purely topographic, but has also electronic character to a certain extent. This brings us to the conclusion that this feature in the STHM image stems from the  $K_4^{4+}$  LUMO. Since this feature is significantly weaker and much less broadened compared to its appearance in the STM image, it can easily be misinterpreted as a fifth potassium atom. The correct stoichiometry, namely  $K_4$ PTCDA, can thus be only revealed by means of a combined analysis on the basis of LEED, ST[H]M, and DFT calculations.

### Higher Doping Stages: $K_{x>4}$ PTCDA

Upon further potassium deposition, the formation of another highly ordered structure is indicated by LEED. However, this degrades on the time scale of minutes to hours by recovering the  $K_4$ PTCDA phase which, therefore, yields the highest doping ratio achievable in a long-term stable, highly ordered structure. Further investigations of higher doping stages are therefore not feasible.

### 5.4.2 Adsorption Heights

The structural investigation in the last section reveals that potassium atoms are laterally incorporated into the PTCDA films. They are situated in between the flat-lying PTCDA molecules and prefer the direct environment of the carboxylic oxygen atoms. It is thus likely that they play an important role for binding mechanisms, at least where the functional groups of PTCDA are involved. For instance, the pristine PTCDA/Ag(111) is commonly known for strong molecule-substrate interactions, even strong enough to pull the entire molecule towards the substrate to an adsorption height below the sum of van-der-Waals radii, i.e., clearly in the covalent bonding regime. [29, 51, 154, 164–169] The carboxylic oxygen atoms are even more affected than the perylene core, giving rise to a significant bending of the molecules. [78, 169] Two bonding channels can thus be distinguished [80, 187]: first, between the delocalized  $\pi$ -orbital system and Ag(111) and, second, between the carboxylic oxygen atoms and Ag(111). Both bonding channels are characterized by significant charge transfer in addition to *van der Waals* interaction. If bonding

channels are modified due to the presence of potassium atoms, it would be clearly visible by adsorption height realignments of the different chemical components. [80, 187] Adsorption heights were measured by means of the NIXSW technique (cf. Subsec. 3.3.3) in the beamtime in January 2015.

### Sample Preparation

The starting point was a 0.6 ML PTCDA/Ag(111) film, whose coverage was estimated from a comparison of the integrated PE yields of the C 1s emission lines with those of an annealed PTCDA ML on Ag(111). Since DRS was not available at the beamline end station, the doping process had to be monitored by means of LEED. For this purpose, potassium was deposited in steps, each followed by a separate LEED measurement, until sharp LEED spots of the K<sub>2</sub>PTCDA phase occurred and the spots of the PTCDA herringbone phase disappeared (cf. Fig. 5.6 (a)). The signature of the pristine PTCDA is, in fact, also absent in the VB spectrum shown in Fig. 5.6 (b), i.e., no feature is cut by the *Fermi* level. The two main features at 0.86 and 2.14 eV can be indeed assigned to the F-LUMO and the HOMO of K-doped PTCDA, respectively, however, the peak positions cannot be clearly identified with one of the reference spectra of pure K<sub>2</sub>PTCDA and K<sub>4</sub>PTCDA phases (cf. first and second doping stage in Fig. 5.3). The F-LUMO and HOMO peak positions are determined in between those of the K<sub>2</sub>PTCDA and the K<sub>4</sub>PTCDA phases. This can be most likely explained by the coexistence of both phases on the sample. This is surprising since the LEED image is indicative of only K<sub>2</sub>PTCDA. The absence of the K<sub>4</sub>PTCDA LEED pattern, however, does not provide evidence that no K<sub>4</sub>PTCDA complexes are on the sample; this only means that they are not highly ordered in this case. A possible coexistence of K<sub>2</sub>PTCDA and K<sub>4</sub>PTCDA must be born in mind when developing the fitting model for NIXSW data. A sample showing the LEED pattern of K<sub>4</sub>PTCDA could not be successfully prepared at the beamline.

### Development of the Fitting Model

High-statistics (HS) C 1s, K 2p and O 1s core level PE spectra (cf. Fig. 5.7) were recorded for the K-doped PTCDA film at room temperature. The same setup and settings were used as later for the XSW-PE spectra, but under off-*Bragg* conditions (photon energy  $h\nu = E_{\text{Bragg}} - 2.6 \text{ eV}$ ). This means that different adsorption heights

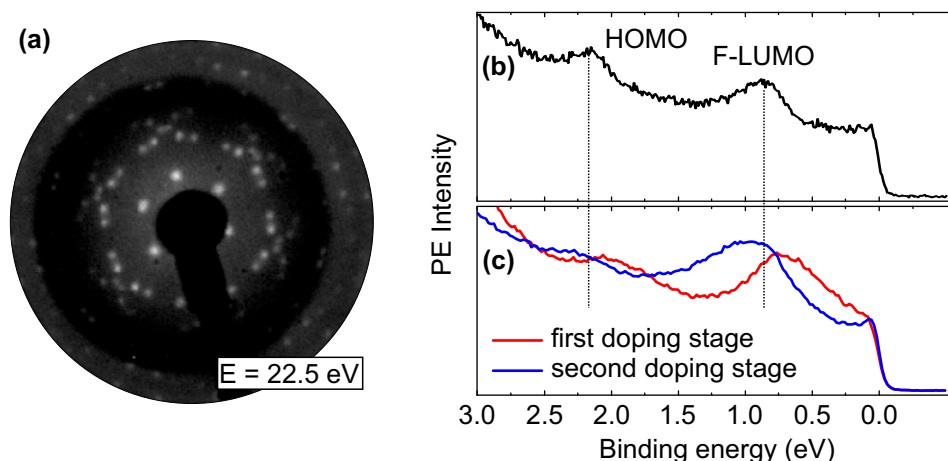


**Figure 5.6:** (a) LEED image, (b) VB spectrum of the sample used for NIXSW investigations, and (c) reference spectra of pure  $K_2$ PTCDA and  $K_4$ PTCDA phases (cf. first and second doping stage in Fig. 5.3). The LEED image in (a) clearly shows the pattern of  $K_2$ PTCDA (cf. Fig. 5.5). The VB spectrum in (b) is shown angle-integrated in the range of  $\pm 22^\circ$  and was measured using He-I $\beta$  ( $h\nu = 23.09$  eV) excitation.

of the PE emitters have no influence on the core level spectra since no standing field builds up.

The fitting model, which was developed for the PE spectra of the  $K_2$ PTCDA phase (first doping stage in Fig. 5.4 (c) and (d)), was transferred to the HE-PE spectra, fixing relative peak positions with respect to C3<sup>m</sup>, maintaining area ratios, and optimizing the *FWHM* of the peaks. However, the HE-PE spectra cannot be reproduced with sufficient accuracy since significant deviations remain in the spectral regions of C1<sup>m</sup>, O1<sup>m</sup>, O2<sup>m</sup>, and their satellite structures. A much better fit, in fact, can be achieved by considering the coexistence of  $K_2$ PTCDA and  $K_4$ PTCDA complexes by a linear combination of the reference PE spectra (cf. first and second doping stages in Fig. 5.4 (c)-(f)) suggesting a stoichiometric ratio between  $K_2$ PTCDA and  $K_4$ PTCDA of roughly 3:2. A precise estimation of this value is impossible since the PE spectra were acquired with different experimental setups under different conditions. The number of potassium atoms per PTCDA molecule has been estimated in the same way as in Sec. 5.3.2. Accordingly, potassium bound to PTCDA and excess potassium amount to 2.3 and 0.7 atoms per molecule, respectively. These values indicate that, in fact, the amount of potassium needed for  $K_2$ PTCDA formation has been exceeded, yet it was also insufficient to form a pure  $K_4$ PTCDA phase on the sample, which further justifies the consideration of



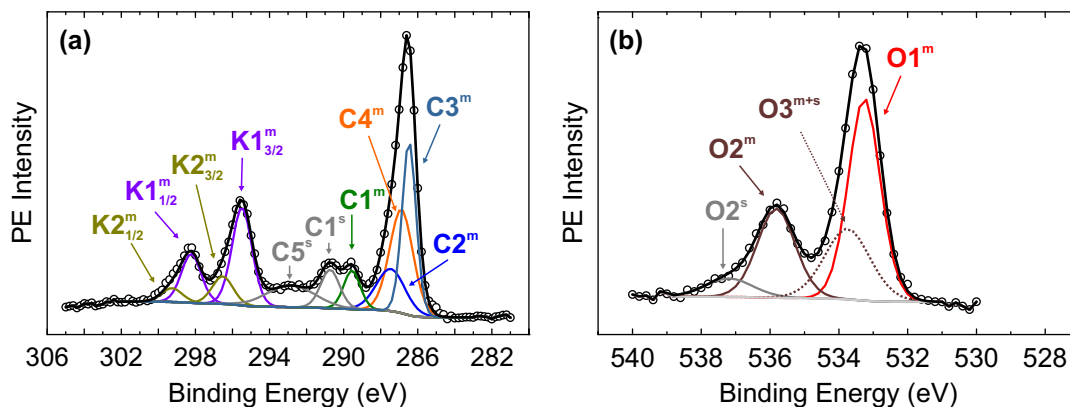


**Figure 5.7:** (a)  $C\ 1s$ ,  $K\ 2p$  and (b)  $O\ 1s$  high-statistics (HS) spectra of the  $K$ -doped PTCDA film, which were used for NIXSW investigations. All spectra were acquired at an emission angle close to  $90^\circ$  with respect to surface normal using an excitation energy of  $2632\text{ eV}$  (off-Bragg) and a pass energy of  $100\text{ eV}$ . The spectra were not calibrated for binding energy. Measured data points are given as circles. The PE backgrounds of  $C\ 1s$  and  $K\ 2p$  have been described by the Shirley function, whereas a linear background has been used for  $O\ 1s$ . Peaks are shown as solid lines. The thick black lines represent the best fits to the data.

the coexistence of both phases. The stoichiometric ratio between  $K_2\text{PTCDA}$  and  $K_4\text{PTCDA}$  cannot be independently inferred from these values, since no significant chemical shift occurs between the  $K\ 2p$  signatures of the two different charge transfer complexes.

The coexistence of  $K_2\text{PTCDA}$  and  $K_4\text{PTCDA}$  complexes must be taken into account for the determination of the adsorption heights. The fitting model of the first doping stage has thus been modified: The contribution of  $C1^m$  of  $K_4\text{PTCDA}$  is accounted for by the peak labeled as  $C1^s$  in Fig. 5.7, which consequently has more intensity than the  $C1^s$  peak of a pure  $K_2\text{PTCDA}$  phase. A new peak  $O3^{m+s}$  is introduced for fitting the  $O\ 1s$  spectrum in order to describe the contributions from  $O2^m$  of  $K_4\text{PTCDA}$  together with contributions from  $O1^s$  of  $K_2\text{PTCDA}$ . We refrain from using a more comprehensive peak decomposition and more constraints since the stoichiometric ratio between  $K_2\text{PTCDA}$  and  $K_4\text{PTCDA}$  remains somewhat uncertain. The derived fitting model for the HS-PE spectra was transferred to the XSW-PE spectra, which have a much lower signal-to-noise ratio. Relating area ratios and fixing relative peak positions to the values determined from the peak-fit of the HS-PE data are necessary to make the fitting procedure more reliable, however,

**Table 5.4:** Peak parameters and constraints of the core level fitting model of the C1s, K2p and O1s signatures of K-doped PTCDA/Ag(111).  $E_B$ : Binding energy; FWHM: peak width; and relative peak areas with respect to the integrated PE yield of each element. Constraints are indicated by mathematical operations on components (A,B,C,...).

	peak	$E_B$ (eV)	FWHM (eV)	area (%)	origin
A	C3 <sup>m</sup>	286.47	0.89	28.7	} C <sub>peryl</sub>
B	C4 <sup>m</sup>	A + 0.42	1.49	A · 1.0	
C	C2 <sup>m</sup>	287.46	1.83	A · 0.5	
D	C1 <sup>m</sup>	289.55	1.05	7.5	} C <sub>funct</sub>
E	C1 <sup>s</sup>	D + 1.18	1.21	8.6	
F	C5 <sup>s</sup>	292.85	3.10	12.2	C Sat
G	K1 <sup>m</sup> <sub>3/2</sub>	A + 9.02	1.26	51.5	} K <sub>PTCDA</sub>
H	K1 <sup>m</sup> <sub>1/2</sub>	G+2.74	G · 1.0	G · 0.5	
I	K2 <sup>m</sup> <sub>3/2</sub>	A + 10.07	1.32	15.1	} K <sub>excess</sub>
J	K2 <sup>m</sup> <sub>1/2</sub>	I+2.74	I · 1.0	I · 0.5	
K	O1 <sup>m</sup>	533.26	1.09	46.4	O <sub>carbox</sub>
L	O3 <sup>m+s</sup>	533.75	1.56	23.1	O <sub>carbox</sub> + O <sub>anhyd</sub>
M	O2 <sup>m</sup>	535.82	1.30	24.2	} O <sub>anhyd</sub>
N	O2 <sup>s</sup>	M + 1.37	1.62	M · 0.26	

components with related peak areas cannot be analyzed independently in terms of their adsorption heights. For instance, the areas of the main carbon peaks of the perylene core (C2<sup>m</sup>, C3<sup>m</sup>, and C4<sup>m</sup>) are related to each other according to Eq. 5.1, a possible bending of the perylene core cannot be revealed directly since the partial yield curves are all the same by the design of the fitting model. This approach, however, is feasible since the perylene core is rather rigid and the coherent fraction is fairly high as shown later. Important parameters and constraints are compiled in Tab. 5.4.

### Vertical Adsorption Geometry

Partial yield curves for all relevant chemical species that are present in the film were extracted from four NIXSW scans recorded at different sample positions. Typical partial yield curves are shown as data points in Fig. 5.8. The solid lines in the graphs

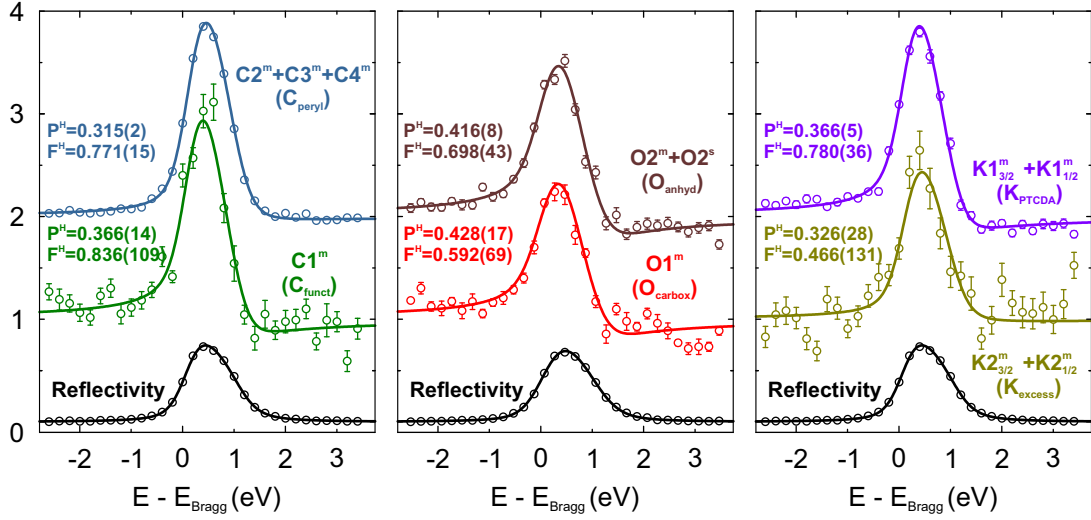


**Figure 5.8:** Partial yield curves obtained for a single NIXSW scan together with the reflectivity curves of the substrate. Measured data points are given as circles. The solid lines represent the best fits to XSW theory yielding coherent fractions  $F^H$  and coherent positions  $P^H$ . The error bars were calculated on the basis of the Monte-Carlo-Simulation implemented in CasaXPS.

represent the best fits to XSW theory from which coherent fractions  $F^H$  and coherent positions  $P^H$  were obtained. All results are compiled in the Argand diagram in Fig. 5.9 (a), where  $F^H$  and  $P^H$  are represented by the polar angle ( $0 \dots 2\pi$ ) and the vector length ( $0 \dots 1$ ), respectively. The values averaged over all NIXSW scans are given by open circle for each chemical species. The adsorption heights were calculated according to Eq. 3.12. The averaged coherent parameters and adsorption heights are listed in Tab. 5.5 along with the respective statistical errors.

Small systematic errors might have been introduced by the design of the fitting model, e.g., by incomplete peak decompositions. Quantifying those errors is in general rather difficult. In order to prevent unnecessary uncertainties, only the main peaks were used for the determination of adsorption heights, satellites were only included if they could be assigned unambiguously (e.g.  $O2^s$ ). The risk that systematic errors are large enough to blur the interpretation of the results is limited, because a variety of peak parameters and constraints were tested. Whether or not a fitting model is better than another is readily indicated by the obtained coherent fractions. The higher these values are in total, the better is the fitting model, i.e.,

**Table 5.5:** Coherent parameters and adsorption heights of *K*-doped PTCDA monolayer domains on Ag(111). The values are the averaged results obtained from four individual NIXSW scans for each chemical species.

species	peaks	$P^H$	$F^H$	$z$ (Å)
$C_{\text{peryl}}$	$C2^m + C3^m + C4^m$	0.321(5)	0.710(55)	3.116(12)
$C_{\text{funct}}$	$C1^m$	0.385(29)	0.71(17)	3.267(68)
$K_{\text{PTCDA}}$	$K1_{3/2}^m + K1_{1/2}^m$	0.371(11)	0.750(67)	3.234(25)
$K_{\text{excess}}$	$K2_{3/2}^m + K2_{1/2}^m$	0.35(18)	0.29(22)	3.19(41)
$O_{\text{carbox}}$	$O1^m$	0.423(30)	0.61(11)	3.355(70)
$O_{\text{anhyd}}$	$O2^m + O2^s$	0.425(20)	0.650(88)	3.361(46)

the peaks are decomposed more accurately into single contributions. In turn, if the peak assignment is incorrect, contributions from species having different adsorption heights are mixed which immediately lowers coherent fractions. [105] The highest coherent fractions were achieved for the fitting model described above.

For  $C_{\text{peryl}}$  ( $=C2^m + C3^m + C4^m$ ) the coherent fraction  $F^H = 0.710 \pm 0.055$  is high, which justifies the made assumption that all perylene carbon atoms have the same adsorption height. This means that the perylene core is essentially planar and adsorbed in a non-tilted geometry. The coherent position  $P^H = 0.321 \pm 0.005$  gives an adsorption height of  $(3.116 \pm 0.012)$  Å. The functional carbon atoms are represented by  $C_{\text{funct}}$  ( $=C1^m$ ) for which  $P^H = 0.385 \pm 0.029$  and  $F^H = 0.71 \pm 0.17$  is found. With an adsorption height of  $(3.267 \pm 0.068)$  Å, the functional carbon atoms are above the perylene core. The two potassium species behave differently in terms of their vertical structure:  $K_{\text{PTCDA}}$  ( $=K1_{3/2}^m + K1_{1/2}^m$ ) shows a high coherent fraction of  $F^H = 0.750 \pm 0.067$  and a coherent position of  $P^H = 0.371 \pm 0.011$ , the corresponding adsorption height is  $(3.234 \pm 0.025)$  Å. In contrast,  $K_{\text{excess}}$  ( $=K2_{3/2}^m + K2_{1/2}^m$ ) gives a low coherent fraction of  $F^H = 0.29 \pm 0.22$ , the corresponding adsorption height thus has to be regarded as the average of a broad range of different adsorption heights. The low coherent fraction cannot be explained merely by different adsorption sites (hollow hcp and hollow fcc) on the Ag(111) surface as the resulting adsorption height difference ( $\Delta z_{\text{fcc-hcp}} = 0.14$  Å) is by far too small. [188] Therefore, cluster formation seems rather likely. The fit results for  $O_{\text{carbox}}$  ( $=O1^m$ ) are  $F^H = 0.61 \pm 0.11$  and  $P^H = 0.423 \pm 0.030$ , the carboxylic oxygen atoms are thus above the carbon atoms with an adsorption height of  $(3.355 \pm 0.070)$  Å. Similarly,

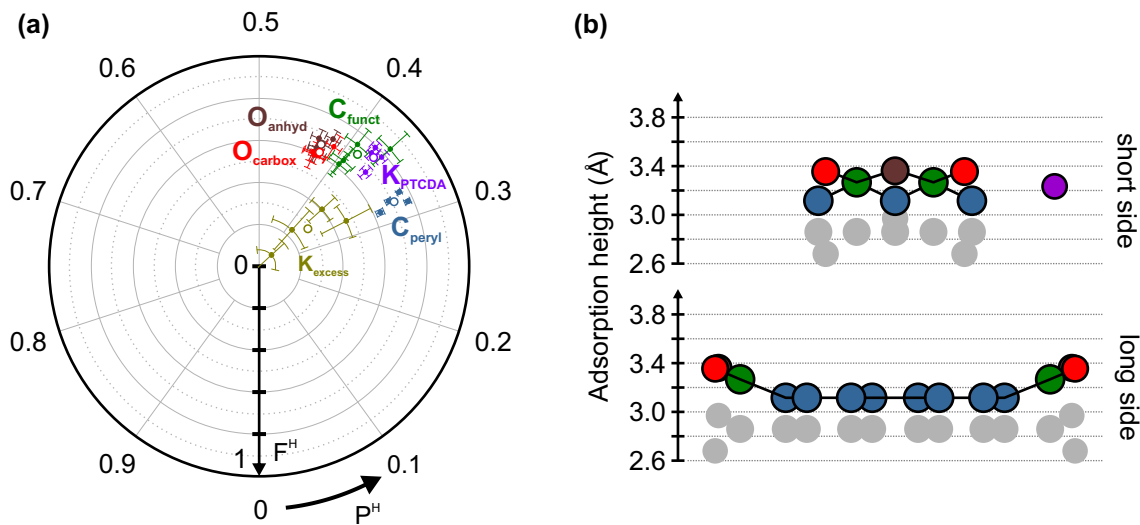


**Figure 5.9:** (a) Argand diagram and (b) suggested vertical adsorption geometry of PTCDA and potassium. The coherent parameters of four single NIXSW data sets are shown as data points in the Argand diagram. The error bars are standard deviations of the fits of the partial yield curves. The values averaged over all single NIXSW data sets are indicated open circles, vectors pointing to the values have been omitted for clarity. The color code is the same as used in Fig. 5.8. Gray spheres represent the undoped monolayer of PTCDA/Ag(111) for comparison. [79]

the anhydride oxygen atoms, represented by  $O_{\text{anhyd}} (=O_2^{\text{m}}+O_2^{\text{s}})$ , give coherent parameters of  $F^H = 0.650 \pm 0.088$  and  $P^H = 0.425 \pm 0.020$ . The corresponding adsorption height is  $(3.361 \pm 0.046)$  Å. The suggested vertical structure is shown in Fig. 5.9 (b) as color-coded ball-and-stick side views together with that of undoped PTCDA/Ag(111) which is represented by gray spheres. The main changes in the vertical structure of PTCDA occurring upon doping are: first, an increase of the adsorption height of the perylene core and, second, the carboxylic oxygen atoms change from downward to upward bending with respect to the perylene core.

The adsorption heights shall be discussed under the aspect of bonding strength with the Ag(111) substrate. The discussion thereby relies on a comparison of the adsorption heights to the sum of the *van der Waals* or covalent radii between the individual chemical species in the film and the substrate atoms. Typical *van der Waals* (vdW) and covalent (cv) radii are given in brackets: Ag ( $r_{\text{vdW}}^{\text{Ag}} = 1.72$  Å,  $r_{\text{cv}}^{\text{Ag}} = 1.45$  Å), perylene ( $r_{\text{vdW}}^{\text{peryl}} = 1.75$  Å,  $r_{\text{cv}}^{\text{peryl}} = 0.77$  Å), carboxylic oxygen ( $r_{\text{vdW}}^{\text{O}} = 1.65$  Å,  $r_{\text{cv}}^{\text{O}} = 0.73$  Å). [78, 189] The adsorption heights of the perylene core in the

K-doped film is  $(3.116 \pm 0.012) \text{ \AA}$ , which is significantly higher than in the pristine PTCDA ML on Ag(111) ( $(2.86 \pm 0.01) \text{ \AA}$  [78, 79]), but somewhat lower than on Au(111) ( $(3.27 \pm 0.02) \text{ \AA}$  [78]). The latter two systems are prime examples for predominantly covalent and *van der Waals* interaction, respectively. The interaction strength of PTCDA with Ag(111) in the K-doped film must thus be in between these two. The bonding channel between the perylene core and Ag(111) determines the adsorption height alignment of the entire molecule, however, the bonding channel via the carboxylic oxygen atoms exerts influence as well. Both bonding channels are not independent from each other, but a moderate coupling has been found in Ref. [185]. There, it is thought that the entire molecule is pulled towards the substrate surface by the carboxylic oxygen atoms if they are on a smaller adsorption height than the perylene core. This is clearly the case for the pristine PTCDA ML on Ag(111), whereas in the K-doped film, it is the opposite, the carboxylic oxygen atoms are above the perylene core. It can thus be assumed that they are also responsible for the increased adsorption height of the perylene core to a certain extent. It is also known that the functional carbon atoms follow the strong distortion of the carboxylic oxygen atoms [187], which, in fact, can also be observed here. The changes in the vertical structure of the anhydride oxygen atoms upon doping are not as pronounced as for the carboxylic oxygen atoms since they remain above the perylene core. The distortion of the molecular geometry with respect to the gas phase geometry is relatively strong. This can be rationalized by the charge transfer leading to a complete filling of the F-LUMO, which was found to weaken the double bond between the functional carbon and carboxylic oxygen atoms thereby making the molecule more flexible. [169, 176]

## 5.5 Summary and Conclusion

Structural, electronic and optical properties of K-doped PTCDA monolayer domains on Ag(111) were comprehensively investigated. Potassium has been deposited onto pristine PTCDA submonolayers resulting in distinct transitions from the commensurate herringbone phase to point-on-line structures even without the need of annealing. This can be attributed to a strong interaction of PTCDA and potassium atoms resulting in charge transfer complex formation. The complex geometries have been determined by means of a combined LEED, ST[H]M and DFT study revealing

the formation of  $K_2$ PTCDA and  $K_4$ PTCDA with potassium adsorption sites nearby the functional anhydride groups. The incorporation of potassium atom in between the molecules strongly alters the electronic properties of the film. While the former LUMO of pristine PTCDA is cut by the *Fermi* level, a complete filling was revealed for both K-PTCDA complex geometries. This enables us to consistently assign their optical absorption features to transitions of PTCDA dianions, albeit they are differently affected by spectral broadening, e.g., the main feature appears blurred for  $K_2$ PTCDA, whereas its vibrational structure is resolved for  $K_4$ PTCDA. It was found in previous studies that spectral broadening can be an indicator for the degree of metal-organic hybridization in certain cases when dealing with metallic substrates. [51] This means that the dianions of the  $K_2$ PTCDA complexes can be regarded as weakly hybridized, those of  $K_4$ PTCDA are even electronically decoupled from the substrate. Remarkably, this trend can be understood as dehybridization of PTCDA by the incorporation of potassium into the film. This interpretation is

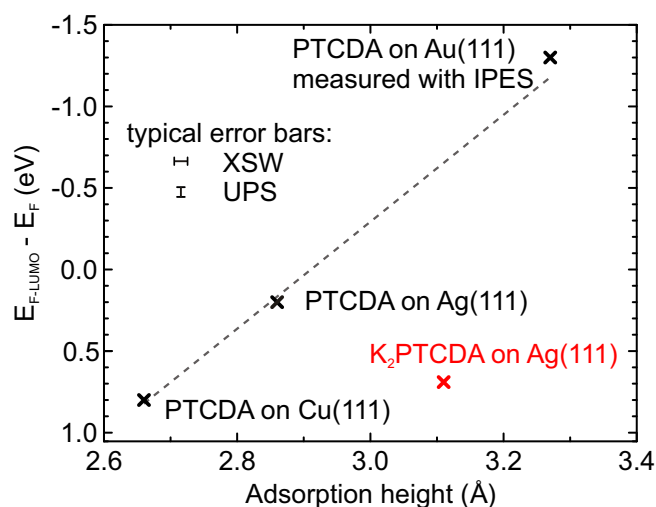


**Figure 5.10:** LUMO or F-LUMO position (binding energy) plotted against the adsorption height of the perylene core for  $K_2$ PTCDA/Ag(111) (red cross). Literature data for PTCDA monolayers on different (111)-oriented metal substrates are shown for comparison (black crosses). F-LUMO and LUMO positions have been measured by means of direct PES [168] and inverse PES (IPES) [190], respectively. Adsorption heights were determined using the NIXSW technique. [77–79] The trend of the LUMO/F-LUMO peak shifting towards higher binding energies with decreasing adsorption heights is indicated by the dashed line (guide to the eye). On the less densely packed Ag(110) surface a similar trend was found for PTCDA based on density functional theory (DFT) calculations only with a different slope. [191]

further corroborated by the adsorption height realignment of PTCDA. The perylene core in the K-doped film clearly moves upwards and the anhydride groups change from a downward- to an upward-bent vertical adsorption geometry compared to the pristine PTCDA on Ag(111). Thus, both bonding channels (one via the anhydride groups and the other via the perylene core) between the molecules and the substrate become significantly weaker compared to pristine PTCDA/Ag(111). This clearly differs from K-doped PTCDA on Ag(110), where only one bonding channel is modified due to local substitution of potassium atoms into the metal substrate underneath the anhydride groups of PTCDA. [80] The adsorption height and the F-LUMO binding energy shift of undoped PTCDA on various (111)-oriented metal surfaces correlate, which is indicated by the dashed line in Fig. 5.10. The K-doped PTCDA films on Ag(111), however, does not fit into this trend, meaning that the F-LUMO shift cannot be simply related to the adsorption height increase within this picture, which has been proposed for pristine PTCDA films on the respective metal surfaces [52]. This illustrates that the substrate plays a minor role in terms of the F-LUMO filling and charge is most likely transferred directly from the potassium atoms into the  $\pi$ -orbital system of PTCDA via its functional groups.



# 6 General Conclusions and Future Perspectives

It was the objective of this work to provide insight into physical effects occurring at organic-based interfaces as well as charge transfer processes in doped layers. To this end, particularly suitable model systems were employed comprising epitaxially grown thin films with well-defined interfaces. These grant access to an unbiased probing of the structure-property relations of the films.

In the first part, it has been demonstrated that a PTCDA monolayer adsorbed on Ag(111) serves as a template for subsequently grown SnPc films thus allowing for high structural ordering up to the multilayer regime. From a comprehensive characterization of the structures formed it was found that the adsorption characteristics directly at the organic-organic interface significantly differ from those at the metal-organic interface that is obtained when the PTCDA layer is omitted. The rich structural information gained were related to the film-thickness-dependent features in the optical absorption of SnPc. The achieved strong improvement of structural ordering manifests in a more narrow, intense optical transition in the near-infrared spectral region, which can be attributed to an efficient coupling of transition dipole moments in a J-type arrangement. It can be expected that template layers will be interesting for future applications that benefit from well-defined organic-organic heterointerfaces and high structural ordering. For the example of organic solar cells (OSC), converting light into electricity can be achieved more efficiently if the physical properties of each layer are purposefully tailored. Template layers provide a route to tune the optical absorption of the employed active materials in order to optimize exciton generation. Likewise, transport layers may benefit from the templating effect since the charge carrier mobility increases with increasing structural ordering, but also the molecular stacking direction is decisive. However, introducing additional layers may compete with other requirements, in particular with the energy-level

alignment of transport levels. A template layer material that is solely selected for structural reasons does not necessarily yield perfect energy-level alignment and may even result in a lower efficiency and/or performance of the device. One strategy to tackle this issue could be using a suitable additional layer that provides beneficial energetic properties and also propagates the templating effect into subsequent layers. Accordingly, it seems worthwhile to structurally investigate multiple stacked heteroepitaxial layers, together with electronic measurements for determining the energy-level alignment. Also a series of highly ordered heterostructures with well-defined alternate heteroepitaxy is conceivable, on which basis organic quantum wells (OQWs) could be structured. These are expected to enable next-generation organic electronics, e.g., lasers, switches, and multiple-valued logic. [11] Template layers may also help preparing such architectures for which rather smooth and well-defined interfaces are essential. [192] Templating also offers the opportunity to manipulate magnetic properties of thin organic films since magnetic coupling sensitively depends on the structures formed. In a prototypical study, films comprising the magnetic molecule cobalt(II)-phthalocyanine (CoPc) have been nanostructured by means of a PTCDA template layer resulting in high-temperature antiferromagnetism, which is much less pronounced if the PTCDA layer is omitted. [193]

In the second part, potassium-doped monolayer domains on Ag(111) have been investigated structurally, electronically, and optically. The experimental results were consistently interpreted with the help of DFT calculations. It has been found that potassium doping induces a structural reordering of the commensurate PTCDA herringbone phase into point-on-line structures comprising charge transfer complexes. Their stoichiometries have been determined as  $K_2$ PTCDA and  $K_4$ PTCDA with potassium adsorption sites nearby the anhydride groups. PTCDA appears doubly negatively charged in both complex geometries while metal-organic hybridization becomes weaker with increasing potassium concentration. Literature data that provide insight into the complex interplay of molecules, alkali metal dopants, and metal surfaces are rather scarce. It would thus be beneficial to systematically investigate the influence of the substrate and dopant reactivity as well as the role played by the functional groups of the molecules. For instance, it has been already shown in Ref. [80] that the more reactive Ag(110) surface allows only the anhydride groups of PTCDA to unbind from the substrate surface upon K-doping whereas the perylene core remains strongly interacting. Thus, it may be worthwhile to check whether this

is a real trend by employing a much less reactive metal substrate such as Au(111). In this case, the undoped PTCDA already weakly interacts with this surface, potentially enabling for the formation of even less strongly coupled charge transfer complexes than observed in this work on the Ag(111) surface. Pursuing this matter might be useful for all applications that employ thin films of alkali doped organic material, where unintended diffusion of the dopants is one of the most challenging issues. Alkali metals can even diffuse into adjacent layers thereby creating recombination centers, which make an opto-electronic device less efficient. [194] This work indicates that a reactive metal surface provides a kind of stabilization effect enabling the formation of well-defined charge transfer complexes. It can be expected that this also holds for other alkali metals such as the commonly used sodium and cesium, though these slightly differ in the atomic radii and ionization energies.

This work particularly emphasizes the importance of thorough structural clarification when aiming at a deep microscopic understanding of organic-organic interfaces as well as charge transfer processes. The results might be helpful to harness the advantages of organic molecular films in future applications.



# Appendix

**DRS drift correction by means of a reference beam.** The issue of drift effects in DRS data has been already mentioned in Subsec. 3.2.1. It became evident that lamp intensity fluctuations play a major role in terms of drift for the setup used in this work. Since DRS measures light intensities relative to a certain reference, usually the pristine substrate, any lamp fluctuations during the experiment can in principle cause (spectral) features which might be misinterpreted in terms of light absorption of deposited films. It is thus important to correct these fluctuations, for example, by an independent measurement of the lamp intensity using a photodiode.

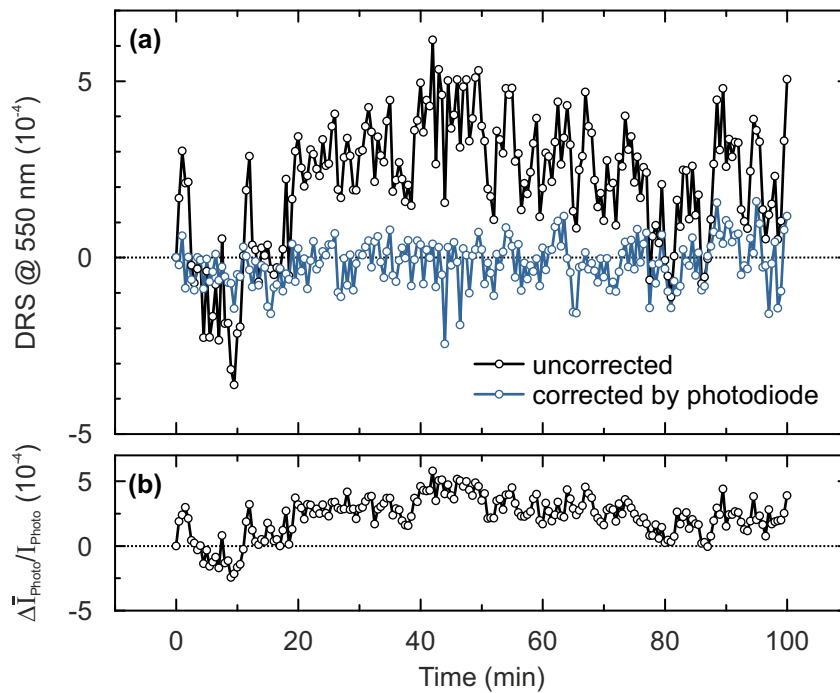


**Figure A.1:** (a) DRS data and (b) corresponding differential photodiode current. For each data point, an accumulation time of 30 s was used.

The achievable improvement shall be demonstrated here. A DRS measurement has been performed where the substrate surface remained unaltered, meaning that no molecules were deposited during the whole experiment. Consequently, each DR spectrum should be a zero line in the ideal case of a drift-free measurement, apart from technically unavoidable noise. In Fig. A.1 (a), the DRS values at 550 nm (where the photodiode has maximum sensitivity) are plotted over time. It can be seen that significant drift accumulates over time up to the mid  $10^{-4}$  range. Since the photodiode current shown in Fig. A.1 (b) nicely correlates with the raw DRS signal, even on time scales of the accumulation time per spectrum, drift effects can be significantly reduced by the approach introduced in Subsec. 3.2.1.

**SnPc structure distorted at silver substrate steps.** Additional structural information about the first monolayer of SnPc on 1 ML PTCDA/Ag(111) is provided in Fig. A.2, where the role of substrate steps is elucidated.

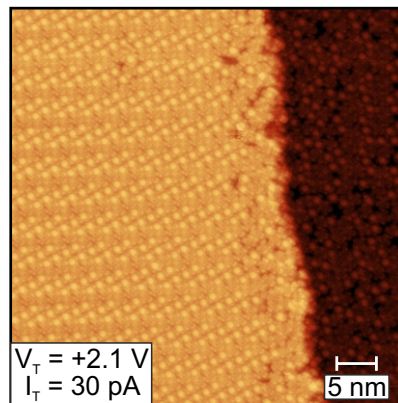


*Figure A.2:* STM image of 1 ML SnPc on 1 ML PTCDA/Ag(111). The highly ordered SnPc monolayer phase P3 on the left-hand side is distorted at a silver step resulting in an unordered phase extending to the right-hand side.

**DRS data of SnPc films on 1 ML PTCDA and 1 ML SnPc on Ag(111).** The imaginary parts  $\epsilon''$  of the dielectric functions of SnPc films depending on the film thickness are shown in Chp. 4. For the sake of completeness, the DRS data used for the extraction of the dielectric functions are given in Fig. A.3.

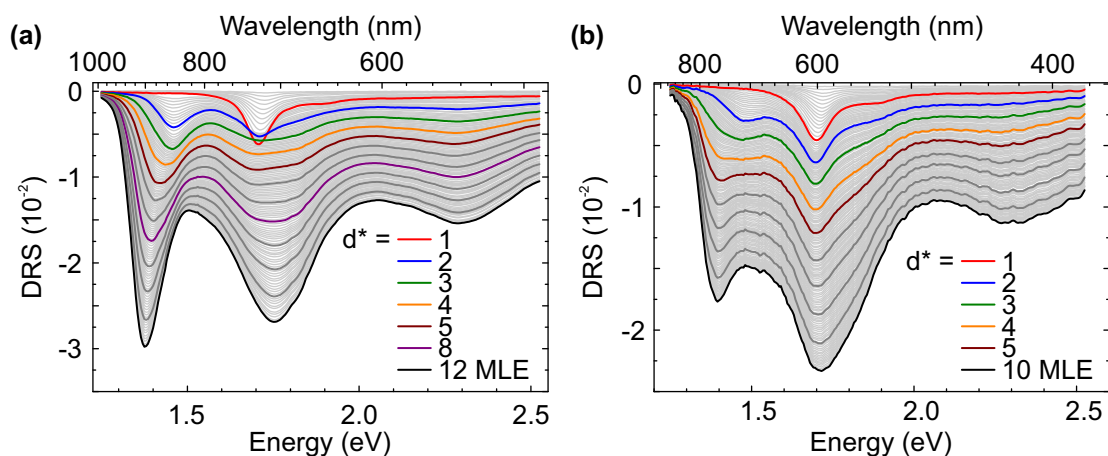


**Figure A.3:** DRS data of SnPc on (a) 1 ML PTCDA/Ag(111) and (b) 1 ML SnPc/Ag(111) depending on the film thickness  $d^*$  of the SnPc adlayer. The data are plotted such that the PTCDA ML/Ag(111) corresponds to the zero baseline. All spectra were numerically corrected for offset drift and slightly smoothed by using a Savitzky–Golay filter.

**LEED data of SnPc multilayers on 1 ML PTCDA/Ag(111).** In Chp. 4, the effect of structural ordering on the optical absorption behavior of SnPc multilayer films on 1 ML SnPc/Ag(111) and 1 ML PTCDA/Ag(111) substrates is discussed. While no LEED spots were obtained in the first case, for the latter, however, long-range ordering could be verified for rather large SnPc layer thicknesses by the LEED pattern shown in Fig. A.4.

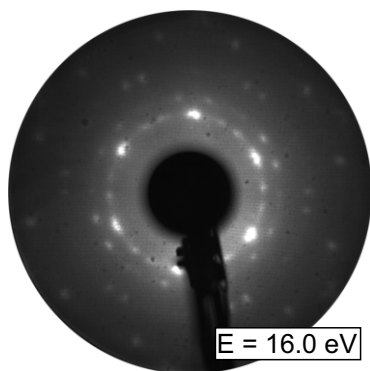


**Figure A.4:** LEED image of 13.6 MLE SnPc on 1 ML PTCDA/Ag(111) acquired at RT. No distortion correction was performed for this image.

**DRS data of potassium-doped PTCDA films on Ag(111).** The imaginary parts  $\epsilon''$  of the dielectric functions of K-doped PTCDA films are shown in Sec. 5.2 as a function of the amount of potassium deposited. For the sake of completeness, the DRS data used for the extraction of the dielectric functions are given in Fig. A.5.

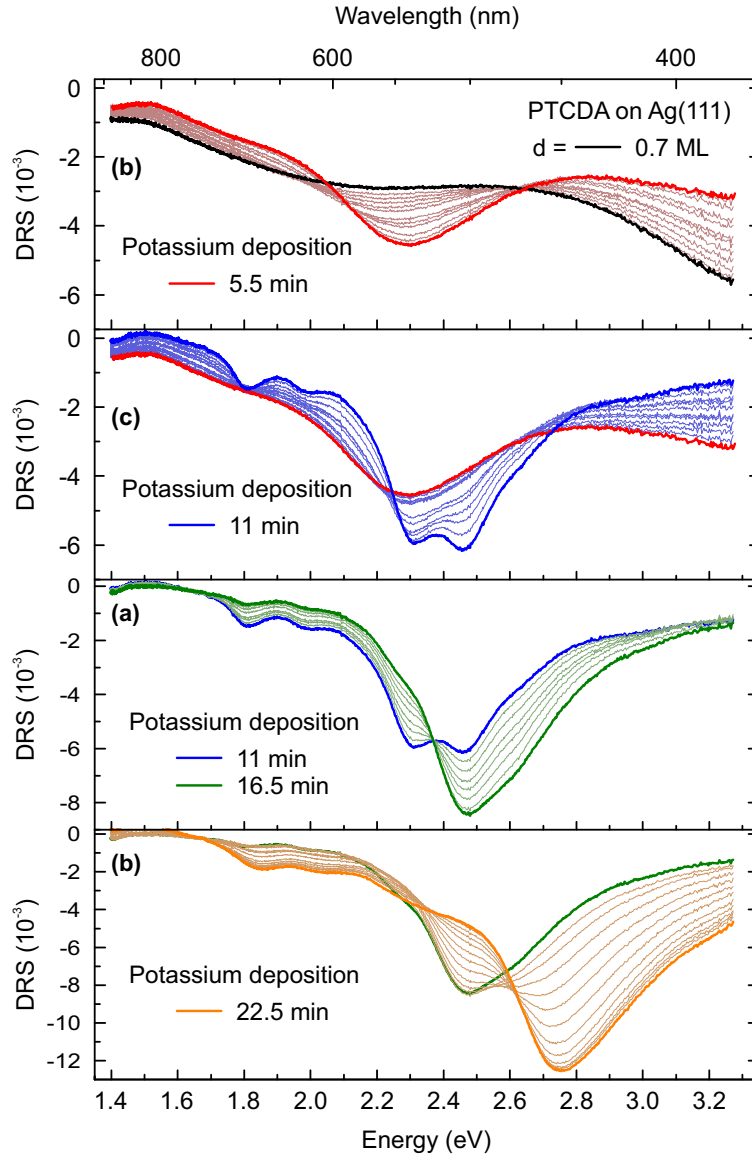


**Figure A.5:** DRS data (unfiltered) of potassium-doped 0.7 ML PTCDA/Ag(111) as a function of the amount of potassium deposited. Distinct doping stages are observed, where each has a characteristic fingerprint in the optical absorption. The spectra were corrected for offset drift by a reference beam measurement (cf. Subsec. 3.2.1).



**Large-scale STM images of potassium-doped PTCDA/Ag(111).** The structures of potassium-doped PTCDA/Ag(111) are investigated in Sec. 5.4.1. It has been found that different structures are formed in the first and second doping stages comprising  $K_2$ PTCDA and  $K_4$ PTCDA charge-transfer complexes, respectively. In order to give an impression about the film quality and long-range ordering, the STM images in Fig. A.6 are additionally provided.

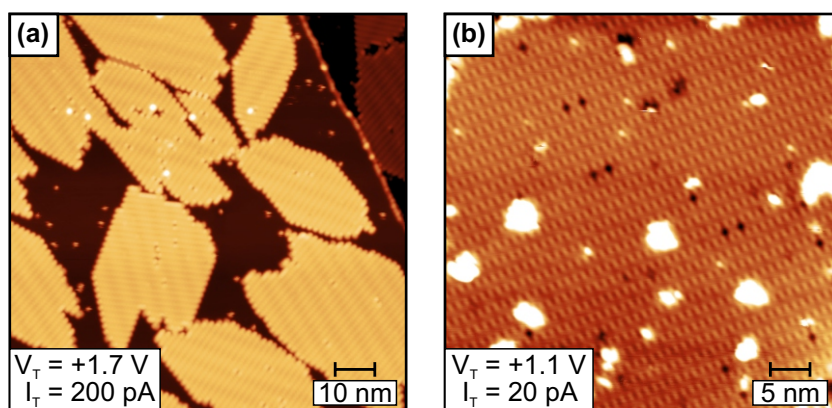


**Figure A.6:** Large-scale STM images of (a) the first and (b) the second doping stages, where  $K_2$ PTCDA and  $K_4$ PTCDA complexes are formed, respectively. The one-dimensional Moiré pattern in (a) is indicative of a point-on-line structure.

**Core level fingerprint of potassium adsorbed on bare Ag(111).** In Chp. 5, K  $2p$  spectra of potassium-doped PTCDA on Ag(111) have been decomposed into two chemically inequivalent species, namely potassium bound to PTCDA and excess potassium. For comparison, the K  $2p$  spectrum of a submonolayer equivalent of potassium on bare Ag(111) is shown in Fig. A.7. The peak parameters of the spin-orbit split features are almost identical to those ascribed to excess potassium in Fig. 5.4 (c) and (e) and Fig. 5.7 (a). The peak parameters fitted to the data are listed in Tab. A.1.

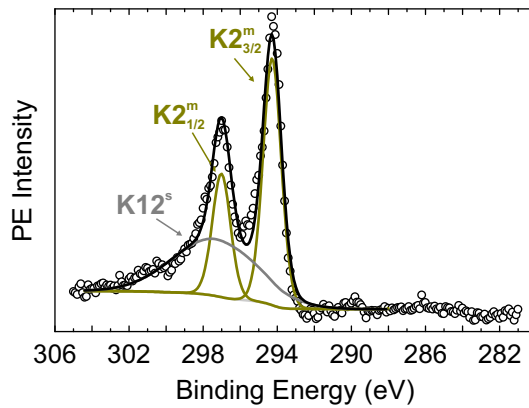


**Figure A.7:** K  $2p$  spectrum of potassium on Ag(111) acquired for  $70^\circ$  emission using an excitation energy of 1486.6 eV (Al  $K_\alpha$ ) and a pass energy of 20 eV. Measured data points are given as circles. The PE background is described by the Shirley function. The peaks of each individual component distinguished by the fitting model are shown as solid lines. The thick black line represents the best fits of the data.

**Table A.1:** Peak parameters of the fitted components in Fig. A.7.  $E_B$ : Binding energy;  $FWHM$ : peak width; and relative peak areas with respect to the integrated PE yield.

Peak	$E_B$ (eV)	Area (%)	$FWHM$ (eV)
$K2_{3/2}^m$	294.15	39.02	1.16
$K2_{1/2}^m$	296.89	19.51	1.16
$K12^s$	297.18	41.47	5.43

Core level PE spectra for the first and second doping stage acquired for normal emission. C 1s, corelevelK2p, and O 1s core level PE spectra of pristine PTCDA/Ag(111) as well as of the first and second doping stages are discussed in Sec. 5.3.2. These spectra were measured for an emission angle of  $70^\circ$  in order to ensure comparability to the NIXSW data. For the sake of completeness, the measurements of the K-doped layers for normal emission are provided in Fig. A.8.

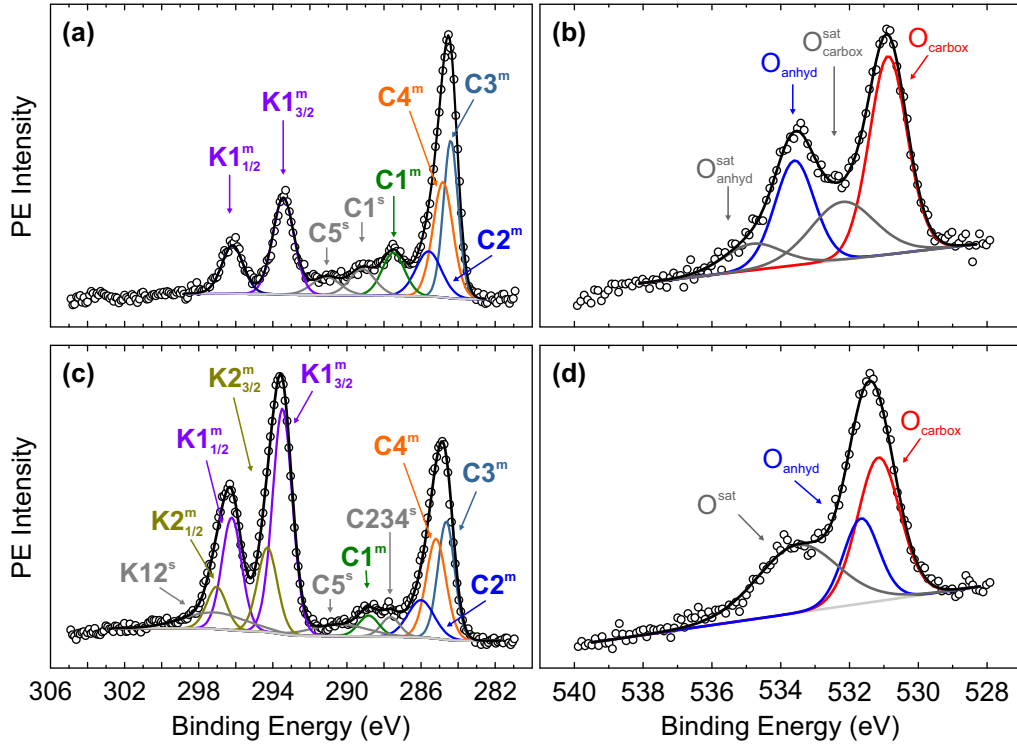


**Figure A.8:** Core level spectra of the first [(a) C 1s and K 2p; (b) O 1s] and second doping stage [(c) C 1s and K 2p; (d) O 1s] acquired in normal emission. An excitation energy of 1486.6 eV (Al  $K_{\alpha}$ ) has been used. C 1s and K 2p were measured with a pass energy of 20 eV, O 1s with 100 eV. Measured data points are given as circles. The peaks of each individual chemical species distinguished by the fitting model are shown as solid lines. The black line represents the best fit to the data.



# References

- [1] A. Mishra and P. Bäuerle, *Small Molecule Organic Semiconductors on the Move: Promises for Future Solar Energy Technology*, Angew. Chem. Int. Ed. **51**, 2020–2067 (2012).
- [2] N. Koch, *Organic Electronic Devices and Their Functional Interfaces*, ChemPhysChem **8**, 1438–1455 (2007).
- [3] S. Liu, W. M. Wang, A. L. Briseno, S. C. B. Mannsfeld, and Z. Bao, *Controlled Deposition of Crystalline Organic Semiconductors for Field-Effect-Transistor Applications*, Adv. Mater. **21**, 1217–1232 (2009).
- [4] S. Reineke, M. Thomschke, B. Lüssem, and K. Leo, *White organic light-emitting diodes: Status and perspective*, Rev. Mod. Phys. **85**, 1245–1293 (2013).
- [5] K. Walzer, B. Maennig, M. Pfeiffer, and K. Leo, *Highly Efficient Organic Devices Based on Electrically Doped Transport Layers*, Chem. Rev. **107**, 1233–1271 (2007).
- [6] F. Zhu, M. Grobosch, U. Treske, L. Huang, W. Chen, J. Yang, D. Yan, and M. Knuifer, *Hole Transparent and Hole Blocking Transport in Single-Crystal-Like Organic Heterojunction: When Rods Hold up Disks*, ACS Appl. Mater. Interfaces **3**, 2195–2199 (2011).
- [7] N. Karl, *Charge carrier transport in organic semiconductors*, Synth. Met. **133-134**, 649–657 (2003).
- [8] S. Tao, H. Matsuzaki, H. Uemura, H. Yada, T. Uemura, J. Takeya, T. Hasegawa, and H. Okamoto, *Optical pump-probe spectroscopy of photocarriers in rubrene single crystals*, Phys. Rev. B **83**, 075204 (2011).

- [9] S. Olthof, S. Mehraeen, S. K. Mohapatra, S. Barlow, V. Coropceanu, J.-L. Brédas, S. R. Marder, and A. Kahn, *Ultralow Doping in Organic Semiconductors: Evidence of Trap Filling*, Phys. Rev. Lett. **109**, 176601 (2012).
- [10] F. Quochi, G. Schwabegger, C. Simbrunner, F. Floris, M. Saba, A. Mura, H. Sitter, and G. Bongiovanni, *Extending the Lasing Wavelength Coverage of Organic Semiconductor Nanofibers by Periodic Organic-Organic Heteroepitaxy*, Adv. Optical Mater. **1**, 117–122 (2013).
- [11] Z. Wang, T. Wang, H. Wang, and D. Yan, *An Organic Quantum Well Based on High-Quality Crystalline Heteroepitaxy Films*, Adv. Mater. **26**, 4582–4587 (2014).
- [12] X. Zhou, J. Blochwitz, M. Pfeiffer, A. Nollau, T. Fritz, and K. Leo, *Enhanced Hole Injection into Amorphous Hole-Transport Layers of Organic Light-Emitting Diodes Using Controlled p-Type Doping*, Adv. Funct. Mater. **11**, 310–314 (2001).
- [13] M. Pfeiffer, K. Leo, X. Zhou, J. S. Huang, M. Hofmann, A. Werner, and J. Blochwitz-Nimoth, *Doped organic semiconductors: Physics and application in light emitting diodes*, Org. Electron. **4**, 89–103 (2003).
- [14] M. F. Craciun, S. Rogge, M.-J. L. den Boer, S. Margadonna, K. Prassides, Y. Iwasa, and A. F. Morpurgo, *Electronic Transport through Electron-Doped Metal Phthalocyanine Materials*, Adv. Mater. **18**, 320–324 (2006).
- [15] A. L. Pitman, J. A. Mcleod, E. K. Sarbisheh, E. Kurmaev, J. Müller, and M. A., *X-ray Spectroscopic Study of the Conduction Band of  $K_3$ :Anthracene and  $K_3$ :Phenanthrene*, J. Phys. Chem. C **117**, 19616–19621 (2013).
- [16] H. Peisert, M. Knupfer, F. Zhang, A. Petr, L. Dunsch, and F. J., *Charge transfer and doping at organic-organic interfaces*, Appl. Phys. Lett. **83**, 3930–3932 (2003).
- [17] A. Koma, *Molecular beam epitaxial growth of organic thin films*, Prog. Cryst. Growth Charact. Mater. **30**, 129–152 (1995).
- [18] A. C. Hillier and M. D. Ward, *Epitaxial interactions between molecular overlayers and ordered substrates*, Phys. Rev. B **54**, 14037–14051 (1996).

- [19] P. Fenter, P. Eisenberger, P. Burrows, S. R. Forrest, and K. S. Liang, *Epitaxy at the organic-inorganic interface*, Physica B **221**, 145–151 (1996).
- [20] S. R. Forrest, *Ultrathin Organic Films Grown by Organic Molecular Beam Deposition and Related Techniques*, Chem. Rev. **97**, 1793–1896 (1997).
- [21] D. E. Hooks, T. Fritz, and M. D. Ward, *Epitaxy and Molecular Organization on Solid Substrates*, Adv. Mater. **13**, 227–241 (2001).
- [22] M. Eremtchenko, J. A. Schaefer, and F. S. Tautz, *Understanding and tuning the epitaxy of large aromatic adsorbates by molecular design*, Nature **425**, 602–605 (2003).
- [23] S. C. B. Mannsfeld, K. Leo, and T. Fritz, *Line-on-Line Coincidence: A New Type of Epitaxy Found in Organic-Organic Heterolayers*, Phys. Rev. Lett. **94**, 056104 (2005).
- [24] S. C. B. Mannsfeld and T. Fritz, *Understanding organic–inorganic heteroepitaxial growth of molecules on crystalline substrates: Experiment and theory*, Phys. Rev. B **71**, 235405 (2005).
- [25] S. C. B. Mannsfeld and T. Fritz, *Advanced Modelling of Epitaxial Ordering of Organic Layers on Crystalline Surfaces*, Mod. Phys. Lett. B **20**, 585–605 (2006).
- [26] N. R. Armstrong, D. M. Alloway, D. Schlettwein, A. Back, K. W. Nebesny, and P. Lee, “Organic Molecular Beam Epitaxy: Creation of Ordered Organic Thin Films and Organic-Organic Heterojunctions”, in *Encyclopedia of Surface and Colloid Science*, Vol. 6, edited by P. Somasundran and A. T. Hubbard, 2nd (Taylor & Francis Group, LLC, 2006), pp. 4349–4363.
- [27] M. Gruenewald, “Organische Heteroepitaxie von PTCDA und SnPc auf einkristallinem Silber”, Diplomarbeit (Friedrich-Schiller-Universität Jena, 2011).
- [28] W. Brütting, *Physics of organic semiconductors* (Weinheim: Wiley-VCH-Verl., 2005).
- [29] L. Kilian, E. Umbach, and M. Sokolowski, *Molecular beam epitaxy of organic films investigated by high resolution low energy electron diffraction*

- (SPA-LEED): 3,4,9,10-perylenetetracarboxylicacid-dianhydride (PTCDA) on Ag(111), Surf. Sci. **573**, 359–378 (2004).
- [30] L. Kilian, E. Umbach, and M. Sokolowski, *A refined structural analysis of the PTCDA monolayer on the reconstructed Au(111) surface – “Rigid or distorted carpet?”*, Surf. Sci. **600**, 2633–2643 (2006).
- [31] C. Stadler, S. Hansen, I. Kröger, C. Kumpf, and E. Umbach, *Tuning intermolecular interaction in long-range-ordered submonolayer organic films*, Nat. Phys. **5**, 153–158 (2009).
- [32] M. Häming, M. Greif, M. Wießner, A. Schöll, and F. Reinert, *Characterization of ultra-thin organic hetero-interfaces – SnPc/PTCDA/Ag(111)*, Surf. Sci. **604**, 1619–1622 (2010).
- [33] M. Häming, L. Weinhardt, A. Schöll, and F. Reinert, *Vibronic structure in resonant Auger Raman spectroscopy of large  $\pi$ -conjugated molecules*, Chem. Phys. Lett. **510**, 82–86 (2011).
- [34] M. Häming, M. Greif, C. Sauer, A. Schöll, and F. Reinert, *Electronic structure of ultrathin heteromolecular organic-metal interfaces: SnPc/PTCDA/Ag(111) and SnPc/Ag(111)*, Phys. Rev. B **82**, 235432 (2010).
- [35] B. Stadtmüller, T. Sueyoshi, G. Kichin, I. Kröger, S. Soubatch, R. Temirov, F. S. Tautz, and C. Kumpf, *Commensurate Registry and Chemisorption at a Hetero-organic Interface*, Phys. Rev. Lett. **108**, 106103 (2012).
- [36] B. Stadtmüller, C. Henneke, S. Soubatch, F. S. Tautz, and C. Kumpf, *Tailoring metal-organic hybrid interfaces: heteromolecular structures with varying stoichiometry on Ag(111)*, New J. Phys. **17**, 023046 (2015).
- [37] C. Wagner, R. Forker, and T. Fritz, *On the Origin of the Energy Gain in Epitaxial Growth of Molecular Films*, J. Phys. Chem. Lett. **3**, 419–424 (2012).
- [38] M. Meissner, F. Sojka, L. Matthes, F. Bechstedt, X. Feng, K. Müllen, S. C. B. Mannsfeld, R. Forker, and T. Fritz, *Flexible 2D Crystals of Polycyclic Aromatics Stabilized by Static Distortion Waves*, ACS Nano **10**, 6474–6483 (2016).



- [39] R. G. Musket, W. McLean, C. A. Colmenares, D. M. Makowiecki, and W. J. Siekhaus, *Preparation of atomically clean surfaces of selected elements: A review*, Appl. Surf. Sci. **10**, 143–207 (1982).
- [40] D. M. Kolb and J. D. E. McIntyre, *Spectrophotometric determination of the optical properties of an adsorbed oxygen layer on gold*, Surf. Sci. **28**, 321–334 (1971).
- [41] J. D. E. McIntyre and D. E. Aspnes, *Differential reflection spectroscopy of very thin surface films*, Surf. Sci. **24**, 417–434 (1971).
- [42] C. Shwe, M. Gal, and M. Gross, *Direct optical observation of hydrogenation induced damage in GaAs*, J. Vac. Sci. Technol. A **9**, 2683–2685 (1991).
- [43] Y. Borensztein, *Surface optical reflectance spectroscopies: Application to semiconductor and metal surfaces*, Physica A **207**, 293–301 (1994).
- [44] D. R. Hagmann and R. E. Hummel, *Characterization of multilayer thin film structures by differential reflection spectroscopy*, Mater. Res. Bull. **31**, 1449–1461 (1996).
- [45] A. Wong and X. D. Zhu, *An optical differential reflectance study of adsorption and desorption of xenon and deuterium on Ni(111)*, Appl. Phys. A **63**, 1–8 (1996).
- [46] R. Forker and T. Fritz, *Optical differential reflectance spectroscopy of ultrathin epitaxial organic films*, Phys. Chem. Chem. Phys. **11**, 2142–2155 (2009).
- [47] R. Forker, M. Gruenewald, and T. Fritz, *Optical differential reflectance spectroscopy on thin molecular films*, Annu. Rep. Prog. Chem., Sect. C: Phys. Chem. **108**, 34–68 (2012).
- [48] M. Knupfer, *Exciton binding energies in organic semiconductors*, Appl. Phys. A **77**, 623–626 (2003).
- [49] M. Kozlik, S. Paulke, M. Gruenewald, R. Forker, and T. Fritz, *Determination of the optical constants of  $\alpha$ - and  $\beta$ -zinc(II)-phthalocyanine films*, Org. Electron. **13**, 3291–3295 (2012).

- [50] M. Gruenewald, L. K. Schirra, P. Winget, M. Kozlik, P. F. Ndione, A. K. Sigdel, J. J. Berry, R. Forker, J.-L. Brédas, T. Fritz, and O. L. A. Monti, *Integer Charge Transfer and Hybridization at an Organic Semiconductor/Conductive Oxide Interface*, J. Phys. Chem. C **119**, 4865–4873 (2015).
- [51] M. Gruenewald, K. Wachter, M. Meissner, M. Kozlik, R. Forker, and T. Fritz, *Optical and electronic interaction at metal-organic and organic-organic interfaces of ultra-thin layers of PTCDAs and SnPc on noble metal surfaces*, Org. Electron. **14**, 2177–2183 (2013).
- [52] M. Gruenewald, C. Sauer, J. Peucker, M. Meissner, F. Sojka, A. Schöll, F. Reinert, R. Forker, and T. Fritz, *Commensurism at electronically weakly interacting phthalocyanine/PTCDA heterointerfaces*, Phys. Rev. B **91**, 155432 (2015).
- [53] E. D. Palik, ed., *Handbook of Optical Constants of Solids I* (Academic Press, New York, 1985).
- [54] R. J. Cole, B. G. Frederick, and P. Weightman, *Substrate dependence of ad-layer optical response in reflectance anisotropy spectroscopy*, J. Vac. Sci. Technol. A **16**, 3088–3095 (1998).
- [55] R. Nitsche and T. Fritz, *Determination of model-free Kramers-Kronig consistent optical constants of thin absorbing films from just one spectral measurement: Application to organic semiconductors*, Phys. Rev. B **70**, 195432 (2004).
- [56] D. W. Marquardt, *An Algorithm for Least-Squares Estimation of Nonlinear Parameters*, J. Soc. Indust. Appl. Math. **11**, 431–441 (1963).
- [57] E. Centurioni, *Generalized matrix method for calculation of internal light energy flux in mixed coherent and incoherent multilayers*, Appl. Opt. **44**, 7532–7539 (2005).
- [58] A. B. Djurišić, T. Fritz, and K. Leo, *Modeling the optical constants of organic thin films: application to 3,4,9,10-perylenetetracarboxylic dianhydride (PTCDA)*, Opt. Commun. **183**, 123–132 (2000).

- [59] K. Ohta and H. Ishida, *Comparison Among Several Numerical-Integration Methods for Kramers-Kronig Transformation*, Appl. Spectrosc. **42**, 952–957 (1988).
- [60] H. Zaglmayr, C. G. Hu, L. D. Sun, and P. Zeppenfeld, *Optical referencing in differential reflectance spectroscopy*, Meas. Sci. Technol. **25**, 115603 (2014).
- [61] A. Einstein, *Über einen die Erzeugung und Verwandlung des Lichtes betreffenden heuristischen Gesichtspunkt*, Ann. Phys. **322**, 132–148 (1905).
- [62] T. Koopmans, *Über die Zuordnung von Wellenfunktionen und Eigenwerten zu den Einzelnen Elektronen Eines Atoms*, Physica **1**, 104–113 (1934).
- [63] S. Hüfner, *Photoelectron Spectroscopy* (Springer, Berlin, 1995).
- [64] M. A. Van Hove, *Surface Crystallography with Low-Energy Electron Diffraction*, Proceedings: Mathematical and Physical Sciences **442**, 61–72 (1993).
- [65] M. Horn-von Hoegen, *Growth of semiconductor layers studied by spot profile analysing low energy electron diffraction - Part I*, Z. Kristallogr. **214**, 591–629 (1999).
- [66] F. Sojka, M. Meissner, C. Zwick, R. Forker, and T. Fritz, *Determination and correction of distortions and systematic errors in low-energy electron diffraction*, Rev. Sci. Instrum. **84**, 015111 (2013).
- [67] F. Sojka, M. Meissner, C. Zwick, R. Forker, M. Vyshnepolsky, C. Klein, M. Horn-von Hoegen, and T. Fritz, *To tilt or not to tilt: Correction of the distortion caused by inclined sample surfaces in low-energy electron diffraction*, Ultramicroscopy **133**, 35–40 (2013).
- [68] The software 'LEEDLab' version 1.64 is commercially available from Scienta Omicron at <http://www.scientaomicron.com/en/products/350/1155>.
- [69] R. Temirov, S. Soubatch, O. Neucheva, A. C. Lassise, and F. S. Tautz, *A novel method achieving ultra-high geometrical resolution in scanning tunnelling microscopy*, New J. Phys. **10**, 053012 (2008).

- [70] C. Weiss, C. Wagner, C. Kleimann, M. Rohlfing, F. S. Tautz, and R. Temirov, *Imaging Pauli Repulsion in Scanning Tunneling Microscopy*, Phys. Rev. Lett. **105**, 086103 (2010).
- [71] L. Gross, *Recent advances in submolecular resolution with scanning probe microscopy*, Nat. Chem. **3**, 273–278 (2011).
- [72] C. Zwick, A. Baby, M. Gruenewald, E. Verwüster, O. T. Hofmann, R. Forker, G. Fratesi, G. P. Brivio, E. Zojer, and T. Fritz, *Complex Stoichiometry-Dependent Reordering of 3,4,9,10-Perylenetetracarboxylic Dianhydride on Ag(111) upon K Intercalation*, ACS Nano **10**, 2365–2374 (2016).
- [73] S. Torbrügge, O. Schaff, and J. Rychen, *Application of the KolibriSensor to combined atomic-resolution scanning tunneling microscopy and noncontact atomic-force microscopy imaging*, J. Vac. Sci. Technol. B **28**, C4E12–C4E20 (2010).
- [74] C. Weiss, “STM beyond vacuum tunnelling: A route to ultra high resolution”, PhD thesis (2011).
- [75] C. Stadler, S. Hansen, F. Pollinger, C. Kumpf, E. Umbach, T.-L. Lee, and J. Zegenhagen, *Structural investigation of the adsorption of SnPc on Ag(111) using normal-incidence x-ray standing waves*, Phys. Rev. B **74**, 035404 (2006).
- [76] R. A. J. Woolley, C. P. Martin, G. Miller, V. R. Dhanak, and P. J. Moriarty, *Adsorbed molecular shuttlecocks: An NIXSW study of Sn phthalocyanine on Ag(111) using Auger electron detection*, Surf. Sci. **601**, 1231–1238 (2007).
- [77] A. Gerlach, S. Sellner, F. Schreiber, N. Koch, and J. Zegenhagen, *Substrate-dependent bonding distances of PTCDA: A comparative x-ray standing-wave study on Cu(111) and Ag(111)*, Phys. Rev. B **75**, 045401 (2007).
- [78] S. K. M. Henze, O. Bauer, T.-L. Lee, M. Sokolowski, and F. S. Tautz, *Vertical bonding distances of PTCDA on Au(111) and Ag(111): Relation to the bonding type*, Surf. Sci. **601**, 1566–1573 (2007).
- [79] A. Hauschild, R. Temirov, S. Soubatch, O. Bauer, A. Schöll, B. C. C. Cowie, T.-L. Lee, F. S. Tautz, and M. Sokolowski, *Normal-incidence x-ray standing-wave determination of the adsorption geometry of PTCDA on Ag(111):*

- Comparison of the ordered room-temperature and disordered low-temperature phases*, Phys. Rev. B **81**, 125432 (2010).
- [80] G. Mercurio, O. Bauer, M. Willenbockel, N. Fairley, W. Reckien, C. H. Schmitz, B. Fiedler, S. Soubatch, T. Bredow, M. Sokolowski, and F. S. Tautz, *Adsorption height determination of nonequivalent C and O species of PTCDA on Ag(110) using x-ray standing waves*, Phys. Rev. B **87**, 045421 (2013).
- [81] C. Kleimann, B. Stadtmüller, S. Schröder, and C. Kumpf, *Electrostatic Interaction and Commensurate Registry at the Heteromolecular  $F_{16}CuPc-CuPc$  Interface*, J. Phys. Chem. C **118**, 1652–1660 (2014).
- [82] B. Stadtmüller, S. Schröder, and C. Kumpf, *Heteromolecular metal-organic interfaces: Electronic and structural fingerprints of chemical bonding*, J. Electron Spectrosc. Relat. Phenom. **204**, 80–91 (2015).
- [83] J. Zegenhagen, *Surface structure determination with X-ray standing waves*, Surf. Sci. Rep. **18**, 202–271 (1993).
- [84] D. P. Woodruff, *Surface structure determination using x-ray standing waves*, Rep. Prog. Phys. **68**, 743–798 (2005).
- [85] F. Schreiber, K. Ritley, I. Vartanyants, H. Dosch, J. Zegenhagen, and B. Cowie, *Non-dipolar contributions in XPS detection of X-ray standing waves*, Surface Science **486**, L519–L523 (2001).
- [86] G. Mercurio, “Study of molecule metal interfaces by means of the normal incidence x-ray standing wave technique”, PhD thesis (Aachen, 2012).
- [87] M. Gruenewald, J. Peuker, M. Meissner, F. Sojka, R. Forker, and T. Fritz, *Impact of a molecular wetting layer on the structural and optical properties of tin(II)-phthalocyanine multilayers on Ag(111)*, Phys. Rev. B **93**, 115418 (2016).
- [88] T. Breuer and G. Witte, *Controlling Nanostructures by Templated Templates: Inheriting Molecular Orientation in Binary Heterostructures*, ACS Appl. Mater. Interfaces **7**, 20485–20492 (2015).

- [89] J. Yang, D. Yan, and T. S. Jones, *Molecular Template Growth and Its Applications in Organic Electronics and Optoelectronics*, Chem. Rev. **115**, 5570–5603 (2015).
- [90] C. Simbrunner and H. Sitter, “Organic van der Waals Epitaxy versus Templated Growth by Organic–Organic Heteroepitaxy”, in , Vol. 3, edited by T. Nishinga and T. F. Kuech, 2nd ed., *Handbook of Crystal Growth: Thin Films and Epitaxy* (Elsevier, Amsterdam, 2015) Chap. 11, pp. 483–508.
- [91] F. Bischoff, K. Seufert, W. Auwärter, S. Joshi, S. Vijayaraghavan, D. Écija, K. Diller, A. C. Papageorgiou, S. Fischer, F. Allegretti, D. A. Duncan, F. Klappenberger, F. Blobner, R. Han, and J. V. Barth, *How Surface Bonding and Repulsive Interactions Cause Phase Transformations: Ordering of a Prototype Macrocyclic Compound on Ag(111)*, ACS Nano **7**, 3139–3149 (2013).
- [92] M. Lackinger, “Untersuchung organischer Adsorbate auf kristallinen Substraten mit dem Raster-Tunnel-Mikroskop”, Dissertation (Technische Universität Chemnitz, 2003).
- [93] I. Kröger, B. Stadtmüller, C. Stadler, J. Ziroff, M. Kochler, A. Stahl, F. Pollinger, T.-L. Lee, J. Zegenhagen, F. Reinert, and C. Kumpf, *Submonolayer growth of copper-phthalocyanine on Ag(111)*, New J. Phys. **12**, 083038 (2010).
- [94] Z. H. Cheng, S. X. Du, N. Jiang, Y. Y. Zhang, W. Guo, W. A. Hofer, and H.-J. Gao, *High resolution scanning-tunneling-microscopy imaging of individual molecular orbitals by eliminating the effect of surface charge*, Surf. Sci. **605**, 415–418 (2011).
- [95] C. Seidel, R. Ellerbrake, L. Gross, and H. Fuchs, *Structural transitions of perylene and coronene on silver and gold surfaces: A molecular-beam epitaxy LEED study*, Phys. Rev. B **64**, 195418 (2001).
- [96] S. Berner, M. Brunner, L. Ramoino, H. Suzuki, H.-J. Güntherodt, and T. A. Jung, *Time evolution analysis of a 2D solid–gas equilibrium: a model system for molecular adsorption and diffusion*, Chem. Phys. Lett. **348**, 175–181 (2001).

- [97] S. Berner, M. de Wild, L. Ramoino, S. Ivan, A. Baratoff, H.-J. Güntherodt, H. Suzuki, D. Schlettwein, and T. A. Jung, *Adsorption and two-dimensional phases of a large polar molecule: Sub-phthalocyanine on Ag(111)*, Phys. Rev. B **68**, 115410– (2003).
- [98] A. Langner, A. Hauschild, S. Fahrenholz, and M. Sokolowski, *Structural properties of tetracene films on Ag(111) investigated by SPA-LEED and TPD*, Surface Science **574**, 153–165 (2005).
- [99] L. D. Sun, J. Gall, G. Weidlinger, C. Y. Liu, M. Denk, and P. Zeppenfeld, *Azimuthal Reorientation of Pentacene upon 2D Condensation*, Phys. Rev. Lett. **110**, 106101 (2013).
- [100] R. Forker, J. Peuker, M. Meissner, F. Sojka, T. Ueba, T. Yamada, H. S. Kato, T. Munakata, and T. Fritz, *The Complex Polymorphism and Thermodynamic Behavior of a Seemingly Simple System: Naphthalene on Cu(111)*, Langmuir **30**, 14163–14170 (2014).
- [101] T. Yokoyama, T. Takahashi, K. Shinozaki, and M. Okamoto, *Quantitative Analysis of Long-Range Interactions between Adsorbed Dipolar Molecules on Cu(111)*, Phys. Rev. Lett. **98**, 206102 (2007).
- [102] I. Fernandez-Torrente, S. Monturet, K. J. Franke, J. Fraxedas, N. Lorente, and J. I. Pascual, *Long-Range Repulsive Interaction between Molecules on a Metal Surface Induced by Charge Transfer*, Phys. Rev. Lett. **99**, 176103 (2007).
- [103] G. Gonella, H.-L. Dai, and T. J. Rokey, *Tetracene Monolayer and Multilayer Thin Films on Ag(111): A Substrate-Adsorbate Charge-Transfer Bonding and Inter-Adsorbate Interaction*, J. Phys. Chem. C **112**, 4696–4703 (2008).
- [104] B. Stadtmüller, I. Kröger, F. Reinert, and C. Kumpf, *Submonolayer growth of CuPc on noble metal surfaces*, Phys. Rev. B **83**, 085416 (2011).
- [105] B. Stadtmüller, M. Willenbockel, S. Schröder, C. Kleimann, E. M. Reinisch, T. Ules, S. Soubatch, M. G. Ramsey, F. S. Tautz, and C. Kumpf, *Modification of the PTCDA-Ag bond by forming a heteromolecular bilayer film*, Phys. Rev. B **91**, 155433 (2015).

- [106] C. Wagner, D. Kasemann, C. Golnik, R. Forker, M. Esslinger, K. Müllen, and T. Fritz, *Repulsion between molecules on a metal: Monolayers and submonolayers of hexa-peri-hexabenzocoronene on Au(111)*, Phys. Rev. B **81**, 035423 (2010).
- [107] E. A. Wood, *Vocabulary of Surface Crystallography*, J. Appl. Phys. **35**, 1306–1312 (1964).
- [108] Y. Wang, J. Kröger, R. Berndt, and W. Hofer, *Structural and Electronic Properties of Ultrathin Tin-Phthalocyanine Films on Ag(111) at the Single-Molecule Level*, Angew. Chem. Int. Ed. **48**, 1261–1265 (2009).
- [109] Y. Wang, J. Kröger, R. Berndt, and W. A. Hofer, *Pushing and Pulling a Sn Ion through an Adsorbed Phthalocyanine Molecule*, J. Am. Chem. Soc. **131**, 3639–3643 (2009).
- [110] M. Lackinger and M. Hietschold, *Determining adsorption geometry of individual tin-phthalocyanine molecules on Ag(111)—a STM study at submonolayer coverage*, Surf. Sci. **520**, L619–L624 (2002).
- [111] N. Papageorgiou, E. Salomon, T. Angot, J.-M. Layet, L. Giovanelli, and G. Le Lay, *Physics of ultra-thin phthalocyanine films on semiconductors*, Prog. Surf. Sci. **77**, 139–170 (2004).
- [112] K. Walzer and M. Hietschold, *STM and STS investigation of ultrathin tin phthalocyanine layers adsorbed on HOPG(0001) and Au(111)*, Surf. Sci. **471**, 1–10 (2001).
- [113] R. Strohmaier, C. Ludwig, J. Petersen, B. Gompf, and W. Eisenmenger, *Scanning tunneling microscope investigations of lead-phthalocyanine on MoS<sub>2</sub>*, J. Vac. Sci. Technol. B **14**, 1079–1082 (1996).
- [114] R. Kubiak and J. Janczak, *X-ray analysis of phthalocyanines formed in the reaction of Au–Cu and Au–Sn alloys with 1,2-dicyanobenzene*, J. Alloys Compd. **189**, 107–111 (1992).
- [115] L. A. Rochford, A. J. Ramadan, D. P. Woodruff, S. Heutz, and T. S. Jones, *Ordered growth of vanadyl phthalocyanine (VOPc) on an iron phthalocyanine (FePc) monolayer*, Phys. Chem. Chem. Phys. **17**, 29747–29752 (2015).



- [116] T. Schmitz-Hübsch, F. Sellam, R. Staub, M. Törker, T. Fritz, C. Kübel, K. Müllen, and K. Leo, *Direct observation of organic–organic heteroepitaxy: perylene-tetracarboxylic-dianhydride on hexa-peri-benzocoronene on highly ordered pyrolytic graphite*, Surf. Sci. **445**, 358–367 (2000).
- [117] F. Sellam, T. Schmitz-Hübsch, M. Toerker, S. Mannsfeld, H. Proehl, T. Fritz, K. Leo, C. Simpson, and K. Müllen, *LEED and STM investigations of organic–organic heterostructures grown by molecular beam epitaxy*, Surf. Sci. **478**, 113–121 (2001).
- [118] M. Campione, L. Raimondo, M. Moret, P. Campiglio, E. Fumagalli, and A. Sassella, *Organic–Organic Heteroepitaxy of Semiconductor Crystals:  $\alpha$ -Quaterthiophene on Rubrene*, Chem. Mater. **21**, 4859–4867 (2009).
- [119] D. Kasemann, C. Wagner, R. Forker, T. Dienel, K. Müllen, and T. Fritz, *Line-on-Line Organic–Organic Heteroepitaxy of Quaterrylene on Hexa-peri-hexabenzocoronene on Au(111)*, Langmuir **25**, 12569–12573 (2009).
- [120] H. Yanagi, K. Ikuta, H. Mukai, and T. Shibutani, *STM-Induced Flip-Flop Switching of Adsorbed Subphthalocyanine Molecular Arrays*, Nano Lett. **2**, 951–955 (2002).
- [121] M. Toader and M. Hietschold, *Tuning the Energy Level Alignment at the SnPc/Ag(111) Interface Using an STM Tip*, J. Phys. Chem. C **115**, 3099–3105 (2011).
- [122] J. D. Baran and J. A. Larsson, *Inversion of the shuttlecock shaped metal phthalocyanines MPc ( $M = Ge, Sn, Pb$ ) - a density functional study*, Phys. Chem. Chem. Phys. **12**, 6179–6186 (2010).
- [123] C. Nacci, K. Kanisawa, and S. Fölsch, *Reversible switching of single tin phthalocyanine molecules on the InAs(111)A surface*, J. Phys.: Condens. Matter **24**, 394004 (2012).
- [124] Y. Li Huang, Y. Lu, T. C. Niu, H. Huang, S. Kera, N. Ueno, A. T. S. Wee, and W. Chen, *Reversible Single-Molecule Switching in an Ordered Monolayer Molecular Dipole Array*, Small **8**, 1423–1428 (2012).

- [125] M. Häming, C. Scheuermann, A. Schöll, F. Reinert, and E. Umbach, *Coverage dependent organic-metal interaction studied by high-resolution core level spectroscopy: SnPc (sub)monolayers on Ag(111)*, J. Electron Spectrosc. Relat. Phenom. **174**, 59–64 (2009).
- [126] F. Würthner, T. E. Kaiser, and C. R. Saha-Möller, *J-Aggregates: From Serendipitous Discovery to Supramolecular Engineering of Functional Dye Materials*, Angew. Chem. Int. Ed. **50**, 3376–3410 (2011).
- [127] K. Palewska, J. Sworakowski, and J. Lipiński, *Molecular aggregation in soluble phthalocyanines - Chemical interactions vs.  $\pi$ -stacking*, Optical Materials **34**, 1717–1724 (2012).
- [128] M. Meissner, “Non-Commensurate Epitaxy of Organic Layers”, PhD thesis (Friedrich-Schiller-Universität Jena, 2016).
- [129] L.-K. Chau, C. D. England, S. Chen, and N. R. Armstrong, *Visible Absorption and Photocurrent Spectra of Epitaxially Deposited Phthalocyanine Thin Films: Interpretation of Exciton Coupling Effects*, J. Phys. Chem. **97**, 2699–2706 (1993).
- [130] S. Kera, H. Fukagawa, T. Kataoka, S. Hosoumi, H. Yamane, and N. Ueno, *Spectroscopic evidence of strong  $\pi$  interorbital interaction in a lead-phthalocyanine bilayer film attributed to the dimer nanostructure*, Phys. Rev. B **75**, 121305 (2007).
- [131] M. Möbus, N. Karl, and T. Kobayashi, *Structure of perylene-tetracarboxylic dianhydride thin films on alkali halide crystal substrates*, J. Cryst. Growth **116**, 495–504 (1992).
- [132] A. A. Levin, T. Leisegang, R. Forker, M. Koch, D. C. Meyer, and T. Fritz, *Preparation and crystallographic characterization of crystalline modifications of 3,4:9,10-perylenetetracarboxylic dianhydride at room temperature*, Cryst. Res. Technol. **45**, 439–448 (2010).
- [133] M. K. Friedel, B. F. Hoskins, R. L. Martin, and S. A. Mason, *A New Metal(II) Phthalocyanine Structure: X-Ray and Mössbauer Studies of the Triclinic Tin(II) Phthalocyanine*, J. Chem. Soc. D, 400–401 (1970).

- [134] M. Kasha, H. R. Rawls, and M. A. El-Bayoumi, *The exciton model in molecular spectroscopy*, Pure Appl. Chem. **11**, 371–392 (1965).
- [135] M. Hoffmann, “Mixing of Frenkel and Charge-Transfer Excitons and Their Quantum Confinement in Thin Films”, in *Electronic Excitations in Organic Multilayers and Organic Based Heterostructures*, Vol. 31, edited by V. M. Agranovich and G. F. Bassani, Thin Films and Nanostructures (Elsevier, Amsterdam, 2003) Chap. 5, pp. 221–292.
- [136] H. Proehl, T. Dienel, R. Nitsche, and T. Fritz, *Formation of Solid-State Excitons in Ultrathin Crystalline Films of PTCDA: From Single Molecules to Molecular Stacks*, Phys. Rev. Lett. **93**, 097403 (2004).
- [137] F. Yang, R. R. Lunt, and S. R. Forrest, *Simultaneous heterojunction organic solar cells with broad spectral sensitivity*, Appl. Phys. Lett. **92**, 053310 (2008).
- [138] Y. Sakakibara, K. Saito, and T. Tani, *Simulation of Phthalocyanine Dimer Spectra by Extended Dipole Model*, Jpn. J. Appl. Phys. **37**, 695–699 (1998).
- [139] J. L. Brédas, J. P. Calbert, D. A. da Silva Filho, and J. Cornil, *Organic semiconductors: A theoretical characterization of the basic parameters governing charge transport*, Proc. Natl. Acad. Sci. U. S. A. **99**, 5804–5809 (2002).
- [140] S. Sharifzadeh, C. Y. Wong, H. Wu, B. L. Cotts, L. Kronik, N. S. Ginsberg, and J. B. Neaton, *Relating the Physical Structure and Optoelectronic Function of Crystalline TIPS-Pentacene*, Adv. Funct. Mater. **25**, 2038–2046 (2015).
- [141] V. Agranovich, K. Schmidt, and K. Leo, *Surface states in molecular chains with strong mixing of Frenkel and charge-transfer excitons*, Chem. Phys. Lett. **325**, 308–316 (2000).
- [142] M. Hoffmann, K. Schmidt, T. Fritz, T. Hasche, V. M. Agranovich, and K. Leo, *The lowest energy Frenkel and charge-transfer excitons in quasi-one-dimensional structures: application to MePTCDI and PTCDA crystals*, Chem. Phys. **258**, 73–96 (2000).
- [143] M. Hoffmann, K. Schmidt, T. Fritz, T. Hasche, V. M. Agranovich, and K. Leo, “The Mixing of Frenkel- and Charge-Transfer Excitons in 1D-Structures: Application to PTCDA and MePTCDI”, in Multiphoton and light driven mul-

- tielectron processes in organics: new phenomena, materials and applications, Vol. 79, edited by F. Kajzar and M. V. Agranovich, NATO Science Series: 3. High Technology (2000), pp. 123–134.
- [144] M. Hoffmann, T. Hasche, K. Schmidt, T. W. Canzler, V. M. Agranovich, and K. Leo, *Excitons in quasi-one-dimensional crystalline perylene derivatives: band structure and relaxation dynamics*, Intern. J. Mod. Phys. B **15**, 3597–3600 (2001).
- [145] M. Hoffmann, Z. G. Soos, and K. Leo, *Absorption spectra and band structure of mixed Frenkel-charge-transfer vibronic states in one-dimensional molecular crystals*, Nonlinear Opt. **29**, 227–237 (2002).
- [146] M. Sumimoto, T. Honda, Y. Kawashima, K. Hori, and H. Fujimoto, *Significance of dimer models describing physical properties in a triclinic solid of tin(ii) phthalocyanine*, RSC Adv. **2**, 12798–12803 (2012).
- [147] M. Hiramoto, K. Kitada, K. Iketaki, and T. Kaji, *Near infrared light driven organic p-i-n solar cells incorporating phthalocyanine J-aggregate*, Appl. Phys. Lett. **98**, 023302 (2011).
- [148] M. Sumimoto, T. Honda, Y. Kawashima, K. Hori, and H. Fujimoto, *Theoretical and experimental investigation on the electronic properties of the shuttlecock shaped and the double-decker structured metal phthalocyanines, MPc and M(Pc)<sub>2</sub> (M = Sn and Pb)*, Dalton Trans. **41**, 7141–7150 (2012).
- [149] A. Yamashita, S. Matsumoto, S. Sakata, T. Hayashi, and H. Kanbara, *Formation and Third-Order Nonlinear Optical Properties of Triclinic Metallophthalocyanine Films*, J. Phys. Chem. B **102**, 5165–5167 (1998).
- [150] K. Walzer, T. Toccoli, A. Pallaoro, S. Iannotta, C. Wagner, T. Fritz, and K. Leo, *Comparison of organic thin films deposited by supersonic molecular-beam epitaxy and organic molecular-beam epitaxy: The case of titanyle phthalocyanine*, Surf. Sci. **600**, 2064–2069 (2006).
- [151] N. Sato, H. Yoshida, and K. Tsutsumi, *Unoccupied electronic structure in organic thin films studied by inverse photoemission spectroscopy*, J. Mater. Chem. **10**, 85–89 (2000).

- [152] K. Iwasaki, K. Umishita, M. Sakata, and S. Hino, *Electrical conductivity and electronic structure of potassium doped PTCDA*, Synth. Met. **121**, 1395–1396 (2001).
- [153] V. Shklover, S. Schmitt, E. Umbach, F. S. Tautz, M. Eremtchenko, Y. Shostak, J. A. Schaefer, and M. Sokolowski, *Strong K-induced changes in perylene-tetracarboxylic-dianhydride films on Ag(110) studied by HREELS and LEED*, Surf. Sci. **482-485**, 1241–1248 (2001).
- [154] F. S. Tautz, M. Eremtchenko, J. A. Schaefer, M. Sokolowski, V. Shklover, and E. Umbach, *Strong electron-phonon coupling at a metal/organic interface: PTCDA/Ag(111)*, Phys. Rev. B **65**, 125405 (2002).
- [155] G. G. Fuentes and M. Knupfer, *Preparation and characterization of single-phase potassium-doped PTCDA thin films*, Phys. Rev. B **70**, 233202 (2004).
- [156] G. G. Fuentes and M. Knupfer, *Electronic structure and work function of potassium-doped PTCDA thin films*, Appl. Phys. A **84**, 329–333 (2006).
- [157] J. Wüsten, S. Berger, K. Heimer, S. Lach, and C. Ziegler, *Interaction of alkali metals with perylene-3,4,9,10-tetracarboxylic-dianhydride thin films*, J. Appl. Phys. **98**, 013705 (2005).
- [158] J. Wüsten, C. Ziegler, and T. Ertl, *Electron transport in pristine and alkali metal doped perylene-3,4,9,10-tetracarboxylicdianhydride (PTCDA) thin films*, Phys. Rev. B **74**, 125205 (2006).
- [159] J. Wüsten, K. Heimer, S. Lach, and C. Ziegler, *Alkali metals in perylene-3,4,9,10-tetracarboxylicdianhydride thin films*, J. Appl. Phys. **102**, 023708 (2007).
- [160] C. Zazza, S. Meloni, A. Palma, M. Knupfer, G. G. Fuentes, and R. Car, *Quasi-One-Dimensional K-O Chain in PTCDA Thin Films: Evidence from First-Principles Calculations*, Phys. Rev. Lett. **98**, 046401 (2007).
- [161] J. Wüsten, S. Berger, M. Salomo, A. Mönnich, M. Bauer, S. Lach, M. Aeschlimann, and C. Ziegler, *Hot-electron dynamics in thin films of sodium-doped perylene-3,4,9,10-tetracarboxylic dianhydride*, Phys. Rev. B **78**, 195326 (2008).

- [162] T. Dienel, A. Krause, R. Alle, R. Forker, K. Meerholz, and T. Fritz, *Alkali Metal Doped Organic Molecules on Insulators: Charge Impact on the Optical Properties*, *Adv. Mater.* **22**, 4064–4070 (2010).
- [163] K. Heimer, J. Wuesten, S. Lach, and C. Ziegler, *Interaction of alkali metals with perylene-3,4,9,10-tetracarboxylic-dianhydride thin films studied by IR spectroscopy*, *J. Chem. Phys.* **126**, 164709 (2007).
- [164] Y. Zou, L. Kilian, A. Schöll, T. Schmidt, R. Fink, and E. Umbach, *Chemical bonding of PTCDA on Ag surfaces and the formation of interface states*, *Surf. Sci.* **600**, 1240–1251 (2006).
- [165] J. Ziroff, F. Forster, A. Schöll, P. Puschnig, and F. Reinert, *Hybridization of Organic Molecular Orbitals with Substrate States at Interfaces: PTCDA on Silver*, *Phys. Rev. Lett.* **104**, 233004 (2010).
- [166] E. Umbach, M. Sokolowski, and R. Fink, *Substrate-interaction, long-range order, and epitaxy of large organic adsorbates*, *Appl. Phys. A* **63**, 565–576 (1996).
- [167] K. Glöckler, C. Seidel, A. Soukopp, M. Sokolowski, E. Umbach, M. Böhringer, R. Berndt, and W.-D. Schneider, *Highly ordered structures and submolecular scanning tunnelling microscopy contrast of PTCDA and DM-PBDCI monolayers on Ag(111) and Ag(110)*, *Surf. Sci.* **405**, 1–20 (1998).
- [168] S. Duhm, A. Gerlach, I. Salzmänn, B. Bröker, R. L. Johnson, F. Schreiber, and N. Koch, *PTCDA on Au(111), Ag(111) and Cu(111): Correlation of interface charge transfer to bonding distance*, *Org. Electron.* **9**, 111–118 (2008).
- [169] L. Romaner, D. Nabok, P. Puschnig, E. Zojer, and C. Ambrosch-Draxl, *Theoretical study of PTCDA adsorbed on the coinage metal surfaces, Ag(111), Au(111) and Cu(111)*, *New J. Phys.* **11**, 053010 (2009).
- [170] D. M. Newns, *Self-Consistent Model of Hydrogen Chemisorption*, *Phys. Rev.* **178**, 1123–1135 (1969).
- [171] P. W. Anderson, *Localized Magnetic States in Metals*, *Phys. Rev.* **124**, 41–53 (1961).

- [172] H. Proehl, R. Nitsche, T. Dienel, K. Leo, and T. Fritz, *In situ differential reflectance spectroscopy of thin crystalline films of PTCDA on different substrates*, Phys. Rev. B **71**, 165207 (2005).
- [173] R. Forker, C. Golnik, G. Pizzi, T. Dienel, and T. Fritz, *Optical absorption spectra of ultrathin PTCDA films on gold single crystals: Charge transfer beyond the first monolayer*, Org. Electron. **10**, 1448–1453 (2009).
- [174] R. Forker, T. Dienel, A. Krause, M. Gruenewald, M. Meissner, T. Kirchhübel, O. Gröning, and T. Fritz, *Optical transition energies of isolated molecular monomers and weakly interacting two-dimensional aggregates*, Phys. Rev. B **93**, 165426 (2016).
- [175] R. Temirov, S. Soubatch, A. Luican, and F. S. Tautz, *Free-electron-like dispersion in an organic monolayer film on a metal substrate*, Nature **444**, 350–353 (2006).
- [176] M. Rohlfing, R. Temirov, and F. S. Tautz, *Adsorption structure and scanning tunneling data of a prototype organic-inorganic interface: PTCDA on Ag(111)*, Phys. Rev. B **76**, 115421 (2007).
- [177] A. Schöll, Y. Zou, M. Jung, T. Schmidt, R. Fink, and E. Umbach, *Line shapes and satellites in high-resolution x-ray photoelectron spectra of large  $\pi$ -conjugated organic molecules*, J. Chem. Phys. **121**, 10260–10267 (2004).
- [178] L. Xu, Y. Meng, Y. Shi, and Y. Liu, *Pitting corrosion of 13Cr steel in oxygen-free completion fluids of organic salt*, Acta Metall. Sin. (Engl. Lett.) **26**, 271–276 (2013).
- [179] A. Caballero, J. Espinós, A. Fernández, L. Soriano, and A. González-Elipe, *Adsorption and oxidation of K deposited on graphite*, Surface Science **364**, 253–265 (1996).
- [180] M. Cardona and L. Ley, eds., *Photoemission in Solids I* (Springer-Verlag Berlin Heidelberg, 1978).
- [181] D. Verner, D. Yakovlev, I. Band, and M. Trzhaskovskaya, *Subshell Photoionization Cross Sections and Ionization Energies of Atoms and Ions from He to Zn*, At. Data Nucl. Data Tables **55**, 233–280 (1993).

- [182] H.-H. Yang, Y.-H. Chu, C.-I. Lu, T.-H. Yang, K.-J. Yang, C.-C. Kaun, G. Hoffmann, and M.-T. Lin, *Digitized Charge Transfer Magnitude Determined by Metal-Organic Coordination Number*, ACS Nano **7**, 2814–2819 (2013).
- [183] Y. Hasegawa, Y. Yamada, and M. Sasaki, *Reordering and Disordering of the Copper Hexadecafluorophthalocyanine ( $F_{16}CuPc$ ) Monolayer by K Doping*, J. Phys. Chem. C **118**, 24490–24496 (2014).
- [184] B. Stadtmüller, M. Gruenewald, J. Peuker, R. Forker, T. Fritz, and C. Kumpf, *Molecular Exchange in a Heteromolecular PTCDA/CuPc Bilayer Film on Ag(111)*, J. Phys. Chem. C **118**, 28592–28602 (2014).
- [185] G. Mercurio, O. Bauer, M. Willenbockel, B. Fiedler, T. Sueyoshi, C. Weiss, R. Temirov, S. Soubatch, M. Sokolowski, and F. S. Tautz, *Tuning and probing interfacial bonding channels for a functionalized organic molecule by surface modification*, Phys. Rev. B **87**, 121409(R) (2013).
- [186] J. Tersoff and D. R. Hamann, *Theory of the scanning tunneling microscope*, Phys. Rev. B **31**, 805–813 (1985).
- [187] O. Bauer, G. Mercurio, M. Willenbockel, W. Reckien, C. H. Schmitz, B. Fiedler, S. Soubatch, T. Bredow, F. S. Tautz, and M. Sokolowski, *Role of functional groups in surface bonding of planar  $\pi$ -conjugated molecules*, Phys. Rev. B **86**, 235431 (2012).
- [188] G. S. Leatherman, R. D. Diehl, P. Kaukasoina, and M. Lindroos, *Unexpected adsorption sites for potassium and rubidium adsorption on Ag(111)*, Phys. Rev. B **53**, 10254–10260 (1996).
- [189] A. Bondi, *van der Waals Volumes and Radii*, J. Phys. Chem. **68**, 441–451 (1964).
- [190] E. V. Tsiper, Z. G. Soos, W. Gao, and A. Kahn, *Electronic polarization at surfaces and thin films of organic molecular crystals: PTCDA*, Chem. Phys. Lett. **360**, 47–52 (2002).
- [191] M. Wießner, J. Ziroff, F. Forster, M. Arita, K. Shimada, P. Puschnig, A. Schöll, and F. Reinert, *Substrate-mediated band-dispersion of adsorbate molecular states*, Nat. Commun. **4**, 1514 (2013).



- [192] H. Sakaki, T. Noda, K. Hirakawa, M. Tanaka, and T. Matsusue, *Interface roughness scattering in GaAs/AlAs quantum wells*, Applied Physics Letters **51**, 1934–1936 (1987).
- [193] M. Serri, W. Wu, L. R. Fleet, N. M. Harrison, C. F. Hirjibehedin, C. W. Kay, A. J. Fisher, G. Aeppli, and S. Heutz, *High-temperature antiferromagnetism in molecular semiconductor thin films and nanostructures*, Nature Communications **5**, 3079– (2014).
- [194] J. Kido and T. Matsumoto, *Bright organic electroluminescent devices having a metal-doped electron-injecting layer*, Applied Physics Letters **73**, 2866–2868 (1998).

# List of Figures

2.1	Molecular orbitals of ethene and energy diagram . . . . .	7
3.1	Scheme of the DRS setup . . . . .	13
3.2	Calculated DRS for a hypothetical film on different substrates . . . . .	15
3.3	Spectral coefficients $A(E)$ and $B(E)$ and $ B / A $ for Ag . . . . .	16
3.4	Principle of photoemission measurements . . . . .	21
3.5	Principle of the x-ray standing wave technique . . . . .	27
4.1	Phase diagram of SnPc on top of 1 ML PTCDA/Ag(111) . . . . .	31
4.2	LEED and STM images of disordered phase of SnPc . . . . .	32
4.3	LEED and STM images of commensurate SnPc phases . . . . .	34
4.4	Plot of the real space lattices . . . . .	37
4.5	STM-tip-induced switching of SnPc molecules . . . . .	39
4.6	STM and LEED images of 1.5 ML SnPc on 1 ML PTCDA/Ag(111) . . . . .	42
4.7	STM image of the SnPc bilayer, 2D FFT, and real-space plot . . . . .	43
4.8	STM and LEED images of 4 MLE SnPc . . . . .	46
4.9	Optical spectra of SnPc on 1 ML PTCDA/Ag(111) . . . . .	48
5.1	$\epsilon''$ spectra of K-doped PTCDA, low K concentrations . . . . .	58
5.2	$\epsilon''$ spectra of K-doped PTCDA, high K concentrations . . . . .	60
5.3	VB spectra of K-doped PTCDA . . . . .	62
5.4	Core level spectra of pristine PTCDA, the first and second doping stage for $70^\circ$ emission . . . . .	64
5.5	LEED and STM data of pristine and K-doped PTCDA/Ag(111) . . . . .	70
5.6	LEED image and VB spectrum of the sample used for NIXSW . . . . .	76
5.7	High-statistics spectra of K-doped PTCDA films used for NIXSW . . . . .	77
5.8	Partial yield curves obtained for a single NIXSW scan . . . . .	79
5.9	textslArgand diagram and suggested vertical adsorption geometry. . . . .	81

5.10	F-LUMO position versus adsorption height of the perylene core . . .	83
A.1	DRS drift correction by means of a reference beam . . . . .	89
A.2	STM image of 1 ML SnPc on 1 ML PTCDA/Ag(111) . . . . .	90
A.3	DRS of SnPc on 1 ML PTCDA/Ag(111) and on 1 ML SnPc/Ag(111)	91
A.4	LEED image of 13.6 MLE SnPc on 1 ML PTCDA/Ag(111) . . . . .	91
A.5	DRS data of potassium-doped 0.7 ML PTCDA/Ag(111) . . . . .	92
A.6	Large-scale STM images of the first and the second doping stages . .	93
A.7	K2p spectrum of potassium on Ag(111) . . . . .	94
A.8	Core level spectra of the first and second doping stage . . . . .	95

# List of Tables

2.1	Molecular substances used in this work . . . . .	8
4.1	Structural parameters of the three commensurate phases of SnPc . . .	36
4.2	Structural parameters of SnPc on 1 ML PTCDA/Ag(111) . . . . .	45
5.1	Peak parameters of the fitted components . . . . .	65
5.2	Calculated ratio of the photoionization cross sections of C1s and K2p	68
5.3	Structural parameters of $K_x$ PTCDA on Ag(111) with $x=0,2$ , and 4 . .	72
5.4	Peak parameters and constraints of the core level fitting model . . . .	78
5.5	Coherent parameters and adsorption heights of K-doped PTCDA/Ag(111) . . . . .	80
A.1	K2p peak parameters of potassium/Ag(111) . . . . .	94

## List of Abbreviations

BL	bilayer
DFT	density functional theory
DRS	differential reflectance spectroscopy
FFT	fast <i>Fourier</i> transformations
HOMO	highest occupied molecular orbital
HS	high-statistics
LEED	low-energy electron diffraction
LUMO	lowest unoccupied molecular orbital
ML	monolayer
MLE	monolayer equivalent
SnPc	metal-phthalocyanine
NIXSW	normal incidence x-ray standing wave
OMBE	organic molecular beam epitaxy
PE	photoelectron
PES	photoelectron spectroscopy
POL	point-on-line
PTCDA	3,4,9,10-perylene-tetracarboxylic-dianhydride
RT	room temperature
SnPc	tin(II)-phthalocyanine
STHM	scanning tunneling hydrogen microscopy
STM	scanning tunneling microscopy
UHV	ultrahigh vacuum
vdW	<i>van der Waals</i>
XSW	x-ray standing wave



# Publications

## Articles

- A1 R. Forker, M. Gruenewald, and T. Fritz, *Optical differential reflectance spectroscopy on thin molecular films*, Annu. Rep. Prog. Chem., Sect. C: Phys. Chem. **108**, 34–68 (2012).
- A2 M. Kozlik, S. Paulke, M. Gruenewald, R. Forker, and T. Fritz, *Determination of the optical constants of  $\alpha$ - and  $\beta$ -zinc(II)-phthalocyanine films*, Org. Electron. **13**, 3291–3295 (2012).
- A3 M. Meissner, M. Gruenewald, F. Sojka, C. Udhardt, R. Forker, and T. Fritz, *Highly ordered growth of PTCDA on epitaxial bilayer graphene*, Surf. Sci. **606**, 1709–1715 (2012).
- A4 M. Gruenewald, K. Wachter, M. Meissner, M. Kozlik, R. Forker, and T. Fritz, *Optical and electronic interaction at metal-organic and organic-organic interfaces of ultra-thin layers of PTCDA and SnPc on noble metal surfaces*, Org. Electron. **14**, 2177–2183 (2013).
- A5 M. Kozlik, S. Paulke, M. Gruenewald, R. Forker, and T. Fritz, *Optical Constants of  $\alpha$ - and  $\beta$ -Zinc(II)-Phthalocyanine Films*, Dataset Papers in Physics **2013**, 926470 (2013).
- A6 B. Stadtmüller, M. Gruenewald, J. Peuker, R. Forker, T. Fritz, and C. Kumpf, *Molecular Exchange in a Heteromolecular PTCDA/CuPc Bilayer Film on Ag(111)*, J. Phys. Chem. C **118**, 28592–28602 (2014).
- A7 M. Gruenewald, C. Sauer, J. Peuker, M. Meissner, F. Sojka, A. Schöll, F. Reinert, R. Forker, and T. Fritz, *Commensurism at electronically weakly in-*

- teracting phthalocyanine/PTCDA heterointerfaces*, Phys. Rev. B **91**, 155432 (2015).
- A8 M. Gruenewald, L. K. Schirra, P. Winget, M. Kozlik, P. F. Ndione, A. K. Sigdel, J. J. Berry, R. Forker, J.-L. Brédas, T. Fritz, and O. L. A. Monti, *Integer Charge Transfer and Hybridization at an Organic Semiconductor/Conductive Oxide Interface*, J. Phys. Chem. C **119**, 4865–4873 (2015).
- A9 G. Rouillé, T. Kirchhübel, M. Rink, M. Gruenewald, J. Kröger, R. Forker, and T. Fritz, *Identification of vibrational excitations and optical transitions of the organic electron donor tetraphenyldibenzoperiflanthene (DBP)*, Phys. Chem. Chem. Phys. **17**, 30404–30416 (2015).
- A10 R. Forker, T. Dienel, A. Krause, M. Gruenewald, M. Meissner, T. Kirchhübel, O. Gröning, and T. Fritz, *Optical transition energies of isolated molecular monomers and weakly interacting two-dimensional aggregates*, Phys. Rev. B **93**, 165426 (2016).
- A11 M. Gruenewald, J. Peuker, M. Meissner, F. Sojka, R. Forker, and T. Fritz, *Impact of a molecular wetting layer on the structural and optical properties of tin(II)-phthalocyanine multilayers on Ag(111)*, Phys. Rev. B **93**, 115418 (2016).
- A12 T. Kirchhübel, M. Gruenewald, F. Sojka, S. Kera, F. Bussolotti, T. Ueba, N. Ueno, G. Rouillé, R. Forker, and T. Fritz, *Self-Assembly of Tetraphenyldibenzoperiflanthene (DBP) Films on Ag(111) in the Monolayer Regime*, Langmuir **32**, 1981–1987 (2016).
- A13 C. Udhardt, R. Forker, M. Gruenewald, Y. Watanabe, T. Yamada, T. Ueba, T. Munakata, and T. Fritz, *Optical observation of different conformational isomers in rubrene ultra-thin molecular films on epitaxial graphene*, Thin Solid Films **598**, 271–275 (2016).
- A14 C. Zwick, A. Baby, M. Gruenewald, E. Verwüster, O. T. Hofmann, R. Forker, G. Fratesi, G. P. Brivio, E. Zojer, and T. Fritz, *Complex Stoichiometry-Dependent Reordering of 3,4,9,10-Perylenetetracarboxylic Dianhydride on Ag(111) upon K Intercalation*, ACS Nano **10**, 2365–2374 (2016).



## Talks

- T1 R. Forker, M. Gruenewald, M. Meissner, and T. Fritz, *Formation of Organic-on-Organic Heteroepitaxial Layers*, 13th ICFSI, July 3-8 2011 in Praha, Czech Republic.
- T2 M. Gruenewald, K. Wachter, F. Sojka, M. Meissner, R. Forker, and T. Fritz, *Organic heteroepitaxy of PTCDA and SnPc on single crystalline silver*, DPG Frühjahrstagung, 25-30 March 2012 in Berlin, Germany.
- T3 M. Gruenewald, *Organic Heteroepitaxy of PTCDA and SnPc on Single Crystalline Metals*, Invited talk given at the seminar of atom and surface physics, Institute of Experimental Physics of the Johannes Kepler University, 9 November 2012 in Linz, Austria.
- T4 M. Meissner, F. Sojka, M. Gruenewald, R. Forker, and T. Fritz, *Quantification of LEED measurements. II. Application to epitaxial organic film*, DPG Frühjahrstagung, 25-30 March 2012 in Berlin, Germany.
- T5 F. Sojka, M. Meissner, M. Gruenewald, R. Forker, and T. Fritz, *Quantification of LEED measurements. I. Systematic Errors*, DPG Frühjahrstagung, 25-30 March 2012 in Berlin, Germany.
- T6 M. Gruenewald, K. Wachter, R. Forker, and T. Fritz, *Organic heteroepitaxy of PTCDA and SnPc on single crystalline metals*, DPG Frühjahrstagung, 10-15 March 2013 in Regensburg, Germany.
- T7 M. Gruenewald, K. Wachter, M. Meissner, M. Kozlik, F. Sojka, R. Forker, and T. Fritz, *Organic Heteroepitaxy of PTCDA and SnPc on Single Crystalline Metals*, OSI-10, 8-13 September 2013 in Chemnitz, Germany.
- T8 M. Kozlik, S. Paulke, M. Gruenewald, R. Forker, and T. Fritz, *Optoelectronic Properties Of Zinc(II)-Phthalocyanine*, DPG Frühjahrstagung, 10-15 March 2013 in Regensburg, Germany.
- T9 M. Kozlik, M. Gruenewald, S. Paulke, R. Forker, C. Ronning, and T. Fritz, *Hybrid Solar Cells Made of Phthalocyanine and Zinc Oxide Nanowires*, Hybrid-Photovoltaics, 15-17 May 2013 in Berlin, Germany.

- T10 M. Kozlik, S. Paulke, M. Gruenewald, R. Forker, C. Ronning, and T. Fritz, *Optoelectronic Properties of Zinc Phthalocyanine*, IVC19, 9-13 September 2013 in Paris, France.
- T11 R. Forker, M. Gruenewald, C. Zwick, and T. Fritz, *Structural and optical investigation of potassium-doped epitaxial molecular thin films on silver*, ICEL-10, 3 September 2014 in Cologne, Germany.
- T12 T. Fritz, M. Gruenewald, C. Zwick, and R. Forker, *Structure and Physical Properties of Epitaxial Molecular Layers: The Influence of K-Doping*, Invited colloquium talk at Institute of Solid State Physics, Graz University of Technology, 23 April 2014, Austria.
- T13 M. Gruenewald, C. Zwick, R. Forker, and T. Fritz, *Structural and optical investigation of ultra-thin layers of potassium doped PTCDA on Ag(111)*, DPG Frühjahrstagung, 30 March - 4 April 2014 in Dresden, Germany.
- T14 M. Gruenewald, J. Peuker, M. Meissner, F. Sojka, R. Forker, and T. Fritz, *Structural and optical investigation of weakly interacting commensurate organic-organic interfaces in SnPc/PTCDA heterolayers on Ag(111)*, DPG Frühjahrstagung, 15-20 March 2015 in Berlin, Germany.
- T15 T. Kirchhübel, T. Morgenroth, M. Gruenewald, R. Forker, T. Yamada, T. Munakata, F. Bussolotti, S. Kera, N. Ueno, and T. Fritz, *Structural, optical, and electronic properties of mono- and multilayers of tetraphenyldibenzoperiflanthene (DBP)*, DPG Frühjahrstagung, 15-20 March 2015 in Berlin, Germany.
- T16 R. Forker, T. Dienel, A. Krause, M. Gruenewald, M. Meissner, T. Kirchhübel, O. Gröning, and T. Fritz, *Optical transition energies of isolated molecular monomers and weakly interacting 2D aggregates*, DPG Frühjahrstagung, 6-11 March 2016 in Regensburg, Germany.

## Posters

- P1 R. Forker, M. Gruenewald, K. Wachter, F. Sojka, and T. Fritz, *Organic Heteroepitaxy of PTCDA and SnPc on Single Crystalline Metals*, CMD-24, 3 - 7 September 2012 in Edinburgh, UK.
- P2 K. Wachter, M. Gruenewald, M. Meissner, F. Sojka, R. Forker, and T. Fritz, *Optical and structural properties of organic heterostructures: PTCDA and SnPc on Au(111)*, DPG Frühjahrstagung, 25-30 March 2012 in Berlin, Germany.
- P3 T. Huempfer, F. Sojka, M. Gruenewald, R. Forker, and T. Fritz, *Growth of coronene-layers on reactive and inert substrates*, DPG Frühjahrstagung, 30 March - 4 April 2014 in Dresden, Germany.
- P4 T. Kirchhübel, M. Gruenewald, J. Peuker, T. Vajas, R. Forker, and T. Fritz, *Decoupling in organic heterostructures of PTCDA and CuPc on single crystalline silver*, DPG Frühjahrstagung, 30 March - 4 April 2014 in Dresden, Germany.
- P5 J. Peuker, F. Sojka, M. Meissner, M. Gruenewald, R. Forker, and T. Fritz, *Structural and optical investigations of organic-organic heterosystems*, DPG Frühjahrstagung, 30 March - 4 April 2014 in Dresden, Germany.
- P6 C. Zwick, M. Gruenewald, R. Forker, and T. Fritz, *Structural and optical investigation of K doping induced changes of PTCDA on Ag(111)*, DPG Frühjahrstagung, 30 March - 4 April 2014 in Dresden, Germany.
- P7 T. Kirchhübel, M. Gruenewald, F. Sojka, S. Kera, F. Bussolotti, T. Ueba, N. Ueno, G. Rouillé, R. Forker, and T. Fritz, *Thin epitaxial films of tetraphenyl-dibenzoperiflanthene (DBP) on Ag(111)*, DPG Frühjahrstagung, 15-20 March 2015 in Berlin, Germany.



# Danksagung

Ich bedanke mich bei all jenen Personen, die zum Gelingen dieser Arbeit beigetragen haben, im Besonderen Prof. Dr. Torsten Fritz für die unmittelbare Betreuung meiner Arbeit und für das entgegengebrachte Vertrauen, am Aufbau seiner neuen Arbeitsgruppe teilhaben zu dürfen. Bei Prof. Dr. Moritz Sokolowski, Prof. Dr. Peter Zeppenfeld und Prof. Dr. Stefan Mannsfeld bedanke ich mich dafür, dass sie sich jeweils zur Übernahme eines Gutachtens dieser Arbeit bereit erklärt haben.

Dr. Roman Forker danke ich für seinen stets hilfreichen Rat in allen fachlichen und nichtfachlichen Angelegenheiten. Als ersten Ansprechpartner und Begleiter von Beginn an schätze ich seine Unterstützung sehr.

Dr. Bernd Schröter danke ich dafür, dass er mich während meiner Studienarbeitszeit für die Nanowelt begeistern konnte und somit dafür gesorgt hat, dass ich in dieser Arbeitsgruppe gelandet bin.

Meinen Kollegen, die stets in freundschaftlicher Atmosphäre, sei es im Labor, im Büro, beim Essen oder in der Freizeit, mich beim erstellen dieser Arbeit tatkräftig unterstützten, danke ich hiermit. Ein besonderer Dank geht an Julia Peuker, Christian Zwick, Tino Kirchhübel, Susanne Fuchs und Kristin Wachter, deren Abschlussarbeiten ich betreuen durfte. Meinen ehemaligen Büronachbarn Matthias Meissner, dessen Verständnis von Elektronenbeugung mir eine große Hilfe war, möchte ich hiermit danken, sowie Felix Otto für die Durchführung der PES Experimente.

Den technischen Mitarbeitern Holger Mühlig, Stefan Prass, Uwe Eberhardt, Helga Rudolph und Silke Frunzke danke ich dafür, dass sie zu jeder Tageszeit ein Ohr für meine technischen Wünsche hatten und an deren Umsetzung unermüdlich gearbeitet haben.

Meiner Freundin Franziska verdanke ich tatkräftige Unterstützung während der gesamten Promotionszeit. Mein Sohn Gero sorgte stets für eine willkommene Abwechslung vom Arbeitsalltag.

Abschließend möchte ich mich bei meiner Familie und bei meinen Freunden bedanken, die eine Promotion überhaupt erst ermöglicht haben und mich dabei stets liebevoll unterstützen.

# Erklärung

Ich erkläre hiermit ehrenwörtlich, dass ich die vorliegende Arbeit selbständig, ohne unzulässige Hilfe Dritter und ohne Benutzung anderer als der angegebenen Hilfsmittel und Literatur angefertigt habe. Die aus anderen Quellen direkt oder indirekt übernommenen Daten und Konzepte sind unter Angabe der Quelle gekennzeichnet.

Bei der Auswahl und Auswertung folgenden Materials haben mir die nachstehend aufgeführten Personen in der jeweils beschriebenen Weise unentgeltlich geholfen:

- LEED- und STM-Messungen an SnPc auf 1 ML PTCDA/Ag(111) sowie deren Auswertung habe ich in Zusammenarbeit mit Julia Peuker durchgeführt.
- Die STM-Daten zum Schaltverhalten von SnPc wurden von Julia Peuker und Susanne Fuchs gemeinsam aufgenommen. Die entstandenen Daten wurden von Susanne Fuchs analysiert. Die Ergebnisse wurden gemeinsam interpretiert.
- Bei der Analyse der 2D-FFT in Fig. 4.7 habe ich Hilfe von Matthias Meißner erhalten
- LEED-Messungen an K-dotiertem PTCDA/Ag(111) und deren Auswertung wurden in Zusammenarbeit mit Christian Zwick durchgeführt
- STM- und STHM-Messungen an K-dotiertem PTCDA/Ag(111) habe ich zusammen mit Christian Zwick durchgeführt
- Die PE-Spektren von K-dotiertem PTCDA/Ag(111) in Fig. 5.3, Fig. 5.4 und Fig. A.8 sowie die PE-Spektren von K/Ag(111) in Fig. A.7 wurden von Felix Otto aufgenommen
- NIXSW-Messungen habe ich in Zusammenarbeit mit Prof. Dr. Christian Kumpf (Forschungszentrum Jülich) und Prof. Dr. Benjamin Stadtmüller

(Technische Universität Kaiserslautern) angefertigt. Die Datenauswertung wurde gemeinsam diskutiert. Bei der Aufnahme der NIXSW-Daten wurden wir von Dr. Sergey Subach, Markus Franke, Gerben Van Straaten (alle vom Forschungszentrum Jülich), Ina Krieger (Universität Bonn) und Norman Haag (Technische Universität Kaiserslautern) unterstützt

- DFT-Rechnungen für K-dotiertes PTCDA/Ag(111) und STM-Simulationen wurden von Dr. Anu Baby, Elisabeth Verwüster, Dr. Oliver T. Hofmann (alle von der Technischen Universität Graz) durchgeführt. Unterstützt wurden sie von Dr. Guido Fratesi (Universität Mailand-Bicocca und Universität Mailand), Prof. Dr. Gian Paolo Brivio (Universität Mailand-Bicocca) und Prof. Dr. Egbert Zojer (Technische Universität Graz). Die Ergebnisse der Rechnungen wurden gemeinsam diskutiert.
- Prof. Dr. Torsten Fritz und Dr. Roman Forker waren an der Interpretation der Daten beteiligt

Weitere Personen waren an der inhaltlich-materiellen Erstellung der vorliegenden Arbeit nicht beteiligt. Insbesondere habe ich hierfür nicht die entgeltliche Hilfe von Vermittlungs- bzw. Beratungsdiensten (Promotionsberater oder andere Personen) in Anspruch genommen. Niemand hat von mir unmittelbar oder mittelbar geldwerte Leistungen für Arbeiten erhalten, die im Zusammenhang mit dem Inhalt der vorgelegten Dissertation stehen.

Die Arbeit wurde bisher weder im In- noch im Ausland in gleicher oder ähnlicher Form einer anderen Prüfungsbehörde vorgelegt.

Die geltende Promotionsordnung der Physikalisch-Astronomischen Fakultät ist mir bekannt.

Ich versichere ehrenwörtlich, dass ich nach bestem Wissen die reine Wahrheit gesagt und nichts verschwiegen habe.

Jena, den 30. November 2016

.....